Chapter 1

Introduction

## 1.1 Introduction of Solar Cell Development

1.1.1 Introduction

After the industrial revolution in the 18th century, the energy consumption increased rapidly. The petroleum has played as a major source of energy since the mid-20th century. From the first oil crisis in 1973, the oil supply wasn't stable due to the war, and the rapid changes of economic. Thus, the demands of second source increase and become more and more important. Besides, the energy saving and renewable energy were also valued gradually [1~3]. On the other hand, the world wide trend of environmental protection has been consciousness and rose. As shown in Fig. 1, the emissions of greenhouse gas, such as carbon dioxide and methane, which may come from the use of petroleum, will be seriously restricted. After the Financial Tsunami in 2008, many countries developed the green technology to revive the economic recession. It is also the most important policy of countries to solve the global warming and the petroleum price jumps. In Taiwan, the government focuses on seven items of green technology: solar cell, LED, wind power generation, bio-fuel, hydrogen energy, and fuel cell, most investment and resource are focused on solar cell in recent years[4].

In general, the green technology is the energy saving and carbon reduction

technique using renewable energy, such as sunlight, wind, rain, tides, and geothermal heat, as shown in Fig. 2 (a) . Nowadays, the solar cells industry grow rapidly among these renewable energy, which may be due to its better conversion efficiency, lower cost with technology progress, and easy to setup the solar cell power station. The solar cells applications are shown in Fig. 2 (b) [5].

Currently, the amount of solar cell energy is only 0.037% of the total energy consumption on earth and the cost is around 0.36€ per watt. But based on EPIA's estimation (as shown in Fig. 3), the cost will be continuously reduced and the price may approach around 0.24€ in 2015, which may cause a strong demands at that moment. The solar cell will play a major role in energy's usage, its amount may further achieve as high as 50% for world wide energy source before 2100[6].
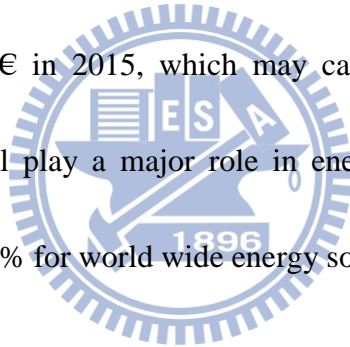
1.1.2 Solar Cell Origins

The solar cell (also called "photovoltaic" or "photoelectric" cell) is a solid state electrical device that converts the energy of light directly into electricity by the photovoltaic effect. The term "photovoltaic" comes from the Greek meaning "light", and "voltaic". The photovoltaic effect was first recognized in 1839 by French physicist A. E. Becquerel [7]. However, the first photovoltaic cell was built, by Charles Fritts, who coated the semiconductor selenium with an extremely thin

layer of gold to form the junctions until 1883. The device was only around 1%

efficient at that time. In 1888, a Russian physicist, Aleksandr Stoletov built the first

photoelectric cell based on the outer photoelectric effect and discovered by Heinrich

Hertz in earlier 1887. Albert Einstein explained the photoelectric effect in 1905 for

which he received the Nobel Prize in Physics in 1921[8]. Russell Ohl patented the

modern junction semiconductor solar cell in 1946 [9], which was discovered while

working on the series of advances that would lead to the transistor. The modern

photovoltaic cell was developed in 1954 at Bell Laboratories [10]. The highly

efficient solar cell was first developed by Daryl Chapin, Calvin Souther

Fuller and Gerald Pearson in 1954 using a diffused silicon p-n junction [11].

1.1.3 Mass Applications and Commercial Operation of Solar Industry

Most of the solar cell are used for power plant and combined with buildings,

which called Building-Integrated PhotoVoltaics (BIPVs). The solar cell power plant

goes on the road toward "Feed-in Tariff" and grown drastically in the past several

years. The BIPV are the use of photovoltaic materials to replace the conventional

building materials in parts of the building envelope, such as the roof, skylights, or the

facades [12]. They are being incorporated into the construction of new buildings as a

principal or ancillary source of electrical power as well. The merit of integrated

photovoltaics on buildings is that the initial cost can be offset by reducing the amount

spent on building materials and labor that would normally be used to construct the

part of the building that the BIPV modules replace. These advantages make BIPV one

of the fastest growing segments of the photovoltaic industry [13].

The Europe's first commercial concentrating solar power tower is PS10 Solar

Power Plant (*Spanish: Planta Solar 10*), which is near Seville, in Andalucia, Spain.

The 11 megawatt (MW) solar power tower produces electricity with 624 large

movable mirrors called heliostats. It took four years to build and so far cost €35

million [14].

In Taiwan, besides the raw material of solar grade Si, we have constructed a

complete supply chain for solar industry. Most of the factory concentrated on the cell

manufactory, where we have several types of cell, such as crystal, polycrystalline, and

thin-film type solar cell. The cell materials are diverse and contain with Si, SiGe, and

CIS-like materials. The system-integration, the inverters, and the power plant

installation are also highly concentrated in Taiwan. The module and the Si ingot

suppliers are the minority in Taiwan's solar industry [15].

1.1.4 Solar Cell Fundamentals

A basic structure of solar cell is a combination of semiconductor p-n junction.

When a p-type semiconductor contacts with a n-type semiconductor, electron and hole

will be recombined with each other near the p-n contact region. The depletion region

is then formed. When sunshine irradiates the p-n junction, electron and hole pairs are

generated in the depletion region. Due to the existence of the built-in electric field,

electrons are swept into the n-region and the holes are swept to the p-region. If the

electrodes are connected, the movement of carriers will induce the photocurrent.

That is the simplest solar cell, as shown in Fig. 4 [16].

From the view of process, the silicon (Si) solar cells are formed by a thin and

heavily doped n-type layer, which contacted with a thick and lightly doped p-type

substrate, as shown in Fig. 5. An anti reflection (A.R.) coating layer will also be

capped on top, which is the side of light incident and this layer will serve to guide

light into the PV Cell. Without this A.R. layer, most of the light would bounce off the

surface of the cell. On the top of A.R. layer, a transparent and protective adhesive

layer is also needed. The layer used for solar cell encapsulation, may be made of glass

or other clear material such clear plastic, seals the cell from the external environment.

Back contact, made out of a metal, covers the entire back surface and acts as a

conductor, as shown in Fig. 6[17].

Different solar cell materials display different efficiencies and have different costs.

Materials for efficient solar cells must have characteristics matched to the spectrum of

available light. Some cells are designed to efficiently convert wavelengths of solar light that reach the earth surface. However, some solar cells are optimized for light absorption beyond earth's atmosphere as well. Light absorbing materials can often be used in multiple physical configurations to take advantage of different light absorption and charge separation mechanisms. Materials presently used for photovoltaic solar cells include monocrystalline silicon, polycrystalline silicon, amorphous silicon, cadmium telluride, and copper indium selenide/sulfide , as shown in Fig. 7 [18].

Many currently available solar cells are made from bulk materials that are cut into wafers between 180 to 240 micrometers thick that are then processed like other semiconductors. Other materials are made as thin-films layers, organic dyes, and organic polymers that are deposited on supporting substrates. A third group are made from nanocrystals and used as quantum dots (electron-confined nanoparticles). Silicon remains the only material that is well-researched in both bulk and thin-film forms [19].

As summarized in Fig. 8, the high efficiency single crystal (S.C.) solar cell startup from 1980s. The S.C. solar cells are developed by dopant diffusion in high temperature driven-in process. (Complicated diffusion, oxidation passivation, photomasking, up to 1000℃) The S.C. solar cell showed a break-through efficiency

about 20% by Stanford University in 1987, and further boosted by University New

South Wealth toward efficiency around 22%~24% from 1990 to 1995. In addition,

from Table Y, the muti-crystalline Si solar cell startup from 1984s. The M. C. solar

cell are developed by ….process. The M. C. solar cell showed efficiency about 15%

by Solarex in 1985, and further boosted by University New South Wealth toward

efficiency around 19% in 1998s. Also, from Table Y, the amorphous Si solar cell

startup from 1976s. The a-Si solar cells are developed by CVD process. (Complicated

diffusion, oxidation passivation, photomasking) The a-Si. solar cell showed an

efficiency about 7% by Solarex in 1986, and further boosted by United Solar toward

efficiency around 9%~11.5% from 1992 to 1999. Now, we discuss about HIT solar

cell. From the literature [20], the HIT solar cells are developed by CVD. (Formation

of pn junction, BSF are all completed by PECVD, less than 200℃) The main

company to research and develop HIT solar cell is Sanyo which started R&D in 1990.

It has been reached high-efficiency around 23% in 2009[21].

1.2 Comparisons of Solar Cells

Now, we compared all kinds of Si based solar cells, as shown in Table 1, and Fig.

9. The c-Si solar cells, poly Si solar cells, and HIT solar cells used Si wafer as

substrate, except a-Si (thin film) solar cells which used glass. Generally, we used

chemical vapor deposition (CVD) as process tool. According to the Table, low

pressure chemical vapor deposition (LPCVD) was usually used to deposit c-Si and

poly-Si solar cells, and plasma enhanced chemical vapor deposition (PECVD) was

used to deposit a-Si (thin film) and HIT solar cells. Then, the maximum process

temperatures are different depend on types of solar cells. The maximum process

temperature of c-Si and poly-Si was the same as 650℃, and a-Si (thin film) solar cell

is 200℃. In addition, the maximum process temperature of HIT solar cell was the

range from 150~200℃. Further, the report efficiency and absorption wavelength were

shown. The report efficiencies of c-Si, poly-Si, a-Si (thin film), and HIT solar cells

were >16%, >14%, >8%, and >18%, respectively. The absorption wavelengths of c-Si,

poly-Si, and HIT solar cells were from 300 nm to 1100 nm, expect a-Si (thin film)

solar cell was from 300 nm to 900 nm. According the Table, we can observe there are

lowest maximum process temperature and highest report efficiency in HIT solar cell

fabrication. Therefore, the HIT solar cell processes consumed lower energy and reach

higher efficiency [22].

1.3 HIT Solar Cell fundamental technologies and toward high efficiency

Efficiency increase and cost down are the key to develop solar cell. According to

the literature, the maximum efficiency of heterojunction with intrinsic thin-layer solar

cells (HIT solar cell) which deposited on special demand of Si wafer can reach around 23%, and it is potentially and become the main stream of Si-based solar cell in the future. Therefore, according to the literature, we tried to deposit single-side and double-side (with back side contact) HIT solar cells, then, do the post-anneal H_2 treatment in order to increase the efficiency. In addition, in this case, we used 40.68MHz very high frequency plasma enhanced chemical vapor deposition (VHF-PECVD) to deposit Si solar cell in order to save process gas and reduce cost [23].

In the page, the c-Si solar cell and the HIT solar cell are compared, as shown in Fig. 10. In the conventional solar cell, the emitter depth is deep, which limited the incident photon flux to the pn junction and wafer. Hence, the solar cell photo current will be limited. On the other side, the diffusion instruments to precede the diffusion process will cost a lot of money, and it also required a higher process temperature. However, in the HIT structure, it has a shallow emitter, which is made by the CVD deposition in a very low process temperature and with a very thin emitter layer on the surface (about 10nm order) Besides, the back contact of base region may also be passivated to lower the density of surface defect. With the passivation in the back contact, the carrier transport may be enhanced and the extraction of photo current will also be increased. These features can make the bulk absorb more light and extract

more photo-electric current, respectively. Therefore, HIT solar cell is promising in the future [24].

The first part of paper review is the fundamentals of HIT solar cell and its simulation. Before discussing the HIT fundamentals, I show two types of HIT solar cell. First, is the single-side HIT solar cell, as shown in Fig. 11 (a), the a-Si emitter and a-Si intrinsic layer was continuously deposited on wafer and the metal on the backside is directly without depositing any Si film. In addition, if the single-side HIT with a intrinsic and doping a-Si layers on backside, which contacts to the metal, is called double-side HIT solar cell, as shown in Fig. 11 (b). Sometimes, the ITO is deposited between a-Si layer and metal to enhance the optical back reflection. If the metal is suitable, ITO can be neglected and the cell performance is still well [25]. There are two type of HIT solar cell as shown in Fig. 12 (a)、(b). The difference is the use of substrate dopant, one is n-type and the other is p-type. In the view of energy bandgap, we may understand the HIT solar cell more clearly. The principle of HIT is to use a wide bandgap material as doping layer as emitter, which contact to c-Si substrate. The wide bandgap material can increase the light transmission. Therefore, the c-Si substrate absorbs more light and the photo-electric current is increased. Furthermore, with the doping layer, only one type of carriers (electron or hole) can flow into the doping layer in the only one direction. But one drawback needs to be

overcome is a larger barrier in the interface of p-type doping layer and the c-Si substrate[26].

Furthermore, we can understand the fundamentals of HIT solar cell through simulation, as shown in Fig. 13. Before discussing the device properties, we must know the material parameters in simulation. The parameters of c-Si is well-known and easy to be obtained, however, the parameters of a-Si,uc-Si and poly Si should be observed from the experiments. In the page, we take a single-side HIT solar cell as an example. We may observe that by inserting a very thin intrinsic a-Si between doped emitter layer and c-Si wafer can increase the device Voc and efficiency. But if the intrinsic a-Si is too thick, the Voc and FF will decrease and the efficiency will also decrease. Therefore, inserting intrinsic a-Si between doping layer and substrate is needed. But the thickness must be optimized [27].

In Fig. 14, I show the HIT solar cell performance under long-term light illumination. Although the a-Si film is used as emitter or back contact passivation layer in HIT device, however, after a long time exposure, there is no significant photo-induced degradation. Its long-term stability is much better than the a-Si based thin-film solar cell, which usually has a degradation ratio about 20%. In addition, the table 2 was about several kinds of solar cell manufactories and research institutes and the information of the wafer types they used for HIT solar cell. Sanyo company

research HIT solar cell several years and fabricated the highest efficiency HIT solar cell. The CZ and FZ wafer showed a similar HIT solar cell performance, but the price of FZ wafer is higher than the CZ wafer. Besides, the use of wafer types (n-doped and p-doped) will not show any significant difference in HIT solar cell performance [28].

1.4 Issues of HIT Film Growth and Cell Process

1.4.1 Interface issue

As for the role of a-Si layer between emitter and c-Si wafer, we may explain in the page. In the real case, the truncated c-Si wafer surface is defective and with a lot of dangling that may require addition hydrogen to passivate the surface defects.　In the view of material, a-Si is a natural passivation layer. The high hydrogen content in the a-Si film may changed with its crystallinity. As we can see in Fig. 15, when the a-Si film (with low crystallinity) transferred into uc-Si, (with high crystallinity) the hydrogen concentration will significantly reduced. We may adjust the film crystallinity by controlling the hydrogen dilution ratio, is the SiH_4 and H_2 ration, when we deposited the Si thin film. Therefore, we may use the proper Si thin film with optimized hydrogen concentration to passivate the surface defect on the interface between emitter and c-Si wafer.. But, it will also be a critical challenge to deposit a ultra thin film on c-Si surface [29].

1.4.2 Surface texture issue

Here, we discuss the effects of c-Si surface morphology and texture on cell performance. In table 3, the author use planar substrate as baseline to optimize the process to obtain a high-performance HIT solar cell. It is found that with a planar wafer as the substrate, it will more easier to observe some tiny changes in HIT cell between different process. Besides, in the author's experiment, they also indicate that after depositing emitter and back contact, the carrier lifetime is over 700us and the Voc is over 0.68. The high Voc is attributed to proper wafer surface clean and fast transition before depositing. When the author obtained a high performance planr HIT cell, they textured the c-Si substrate to achieve a higher efficiency device. It is difficult to clean a texture wafer surface well and the texture substrate HIT has a lower Voc. As a result, it is necessary to adjust surface clean process well. Take an example from NREL, they used RCA1 and RCA2 as clean process after texturing the substrate. It can enhance Voc up to as high as 0.67-0.66 volt in texture HIT device and increase the Jsc, too. The SEM image, as shown in Fig. 16 (a), showed the pyramidal texture surface from NREL. The size is less than 10um is proper for HIT solar cell. The TEM image, as shown in Fig. 16 (b), can confirm high-quality conformal coating for a-Si and ITO. NREL concluded that with a well cleaned texture surface and a high a-Si film coverage on c-Si wafer are the key of high Voc texture

device [30].

1.4.3 Contact optimization issue

Here, we discuss the effect of doping layer and contact on HIT solar cell performance. In Fig. 17, it is usually to deposit a-Si intrinsic layer at a lower temperature. (less than 150℃). In NREL's research, by increasing n-layer deposition temperature. can increase the Voc in HIT device. It is because that a higher deposition temperature in doping layer can provide a more effective activation for dopant irons and a good quality film in a optimized temperature. But at a higher deposition temperature, it may degrade the film quality and dopant interdiffusion between the emitter and c-Si. In table 4, by using the deposition parameter of emitter a-Si in the single-side HIT solar cell on the backside of double-side HIT solar cell, we may fabricate as a-Si passivation layer in back contact. Therefore, the simple double-side HIT solar cell can be made. As we can observe, the HIT device with a back-contact passivation will have a higher deice Voc [31].

1.4.4 ITO film deposition issues

Fig.18 shows the effect of doping concentration, a-Si layer, and ITO on HIT. ITO can increase the current extracting area and adjust Eg to decrease the contact barrier with electrode.

Therefore, ITO layer is necessary. When the ITO layer is present, large doping concentration and thickness of a-Si doping layer is required to maintain reasonable diode behavior. On the other hand, if the ITO layer is excluded, the device is a classical p-n diode, the a-Si:H doping and thickness have a significantly less pronounced effect on Voc

Now, I explain the effect of ITO electron density and surface recombination on HIT. Fig. 19 (a) shows the dependence of a p-wafer HIT cell open-circuit voltage Voc on the electron density in the doped a-Si:H layer. Because of the strong n-type doping in the ITO, the electron density in the adjacent a-Si:H has a small effect on the device performance.

Fig. 19 (b) shows the dependence of Voc on surface recombination. When the p-HIT back with a-Si, the Voc dropped slowly. Whereas, the front with/without a-Si, the Voc also dropped significantly. In practice, there is a large lattice mismatch between c-Si and ITO, which can create interface defects. By inserting a-Si:H between the c-Si and ITO layers, the a-Si:H layer forms a buffer that is important for surface passivation but otherwise has little influence on device performance.

1.5 Motivations

In this study, we tried to deposit a high efficiency HIT solar cell and find a

treatment method to improve HIT cell efficiency. The method may be with a high

feasibility and easy to integrate into the deposition process[32].

In the initial stage of our experiment, we will deposit the Si film for solar cell

fabrication. The intrinsic, n-type, and p-type Si films will be deposited. We will find

out the optimized process and try to control the crystalline of the Si films under a high

deposition rate. The transition of amorphous and poly crystalline Si films, which are

intrinsic and un-doped, will be studied and controlled in the sequence of our

experiments. As for n-type and p-type Si films, which are used as contact layer in

solar cell, will be deposited under different doping concentration. The film resistance

and its crystalline will also be studied[33].

After we well-controlled the Si films for solar cell deposition, we will try to find

out the key to high efficiency HIT solar cell. We will use computer-assisted designed

(CAD) software, which is AMPS 1D, to simulate the HIT solar cell properties. We

will try the study the correlation of Si film characteristics to HIT solar cell efficiency.

The Si film characteristics, such as defect distribution, film thickness, and doping

properties, will be studied for optimizing the HIT solar cells. We may find out an

optimized structure and film properties for HIT solar cells[34].

From the experiments of Si film deposition and solar cell simulation, we may

understand the key to high efficiency HIT solar cell. We may propose a new

methodology to improve HIT solar cell efficiency. We propose the usage of the

hydrogen (H_2) plasma to treat the HIT solar cell, which treatment is preceded in very

high frequency chemical vapor deposition (VHF-CVD) system. With the usage of

VHF plasma source (41.56MHz), a high efficiency and low ion bombardment

treatment may be achieved [35].

In order to further increase the HIT solar cell efficiency, the post-deposition

process is also studied. A low temperature and rapid thermal anneal may be required

to high efficiency HIT solar cell. The impact of RTA temperature will be studied and

the optimized process will also be found to enhance the HIT solar cell efficiency.

Then, before we deposited HIT solar cell, we used 1D-AMPS to simulate the device

performance. From 1D-AMPS simulation, we can obtain the relationship of i-layer

thickness, doping concentration, defect density and HIT solar cell efficiency. Finally,

we can find the optimized condition to deposit HIT solar cell [36].

According the literature [37], now, we induced a treatment- post H_2 plasma treatment

- to improve solar cell performance.

Paper review two: Influence of hydrogen plasma on HIT surface passivation and

performance. The Fig. 20 shows the dependence of effective surface recombination

velocity on the deposition temperature with different c-Si surface passivation

treatment. When using H_2 plasma treatment, the effective surface recombination

velocity is lowest. The Fig. 21 is the measured dependence of effective lifetime on the

excess carrier density and the simulation results for two samples with deposition temp.

is 300°C And two treatments of the c-Si surface: HF dip ~5% and hydrogen plasma.

Excellent fitting is achieved in this fig. and using H2 plasma treatment can make the

effective lifetime higher than HF dip. Therefore, H2 plasma is the best c-Si surface

passivition method [38].

As mentioned above, we know post H_2 plasma treatment can improve HIT solar cell

performance. Therefore, we assumed another anneal – rapid thermal annealing

(RTA) – also improve HIT solar cell performance can be tried. We will show the

experiment result in the chapter 5.
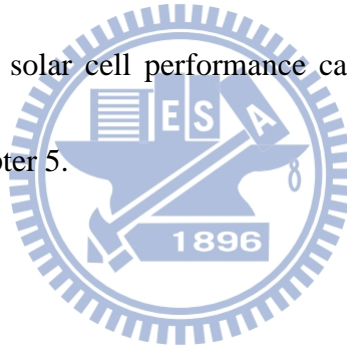
Chapter 2

Optimization of Si Thin-film Deposition for HIT solar cell

2.1 Introduction

In this chapter, we tried to optimization of Si thin film deposition for HIT solar cell. First, we use 40.68MHz PECVD (VHF-PECVD) , as shown in Fig. 22, to deposit intrinsic Si thin films (i-Si) and doped (p-type or n-type) Si thin films by well-control its crystalline (Xc) under high deposition rate. Raman analysis can help to estimate all kinds of crystalline (Xc) of Si thin films, and XRD analysis can also estimate it. In addition, SEM images of plan-view and cross section show us the Si thin films morphology directly. P-10 was used to estimate film thickness of Si thin films, and four-point probe was also used to estimate sheet resistance of these Si thin films.[39]

2.1.1 VHF-PECVD

In order to enhance deposition rate of Si film, we used the very high frequency plasma enhances chemical vapor deposition (40.68MHz VHF-PECVD), which was set in ITRI (Fig.22). The plasma frequency was increased from 13.56 MHz to

40.68MHz so that the deposition rate can be increased ($> 8\text{Å} / \text{sec}$) and the quality of Si films was still well. In addition, the higher deposition rate resulted in lower gas consumption [40].

2.1.2 Raman intro. & Xc definition

The Raman spectrum was relative to molecular vibration energy. When incident photon interacted with molecular, the electrons jumped from basic state to the virtual state. The molecular released the energy by scattering without absorb it. If the released energy was equal to one of incident photon, the scattering light was called Rayleigh scattering, as shown in Fig.23. If the released energy was not equal to one of incident photon, the scattering light was called Raman scattering. And the loss energy of photon scattering was called Stokes scattering, the increase energy was called anti-Stokes scattering. Generally, Raman spectrum detected the difference of scattering photon and incident photon, and it was called Raman shift, which was molecular vibration energy. One of a million incident photon scattered by sample molecular, most of scattering light was Rayleigh scattering, and Raman scattering intensity was only around one of a thousand Rayleigh scattering. Raman spectrum was the vibration spectrum of measuring molecular directly, and it can qualify the matter qualitatively. The tiny change of matter structure reflected in Raman spectrum

sensitively. Therefore, it can be used to research the change of matter structure in physical, chemical, or all aspect.

The Raman spectrum we showed in this report was from Horiba HR800system, which system had two Laser sources: He/Ne Laser (wavelength: 632.8 nm) and Ar Laser (wavelength: 514.5 nm). We used the longer wavelength He/Ne Laser to reduce the possibility of Si films crystalline caused by Laser anneal. In addition, the absorption coefficient of longer wavelength Laser was smaller than shorter one. Therefore, the He/Ne Laser penetrated more deeply than Ar Laser, and got more Si film information. Further, we used 2400 grating to increase resolution, and open filter to reduce Laser intensity, preventing Laser anneal from crystallizing Si film. The Fig. 24 shows the process of angular dispersion [41].

2.1.3 XRD intro. & Xc orientation

Bragg's Law and Diffraction

The atomic planes of a crystal cause an incident beam of X-rays to interfere with one another as they leave the crystal. In some incident angle, the crystal face will diffract the x-ray beams with same phase. When the difference is as the integer of incident x-ray wavelength, a construction diffraction pattern will be appeared, as

shown in Fig. 25. When the condition is achieved, that is the Bragg's Law [42]:

$$2d\sin\theta = n\lambda \qquad \text{Eq. 1}$$

The different crystal structure will result in different composition of {2θ hkl} Hence, we can use the x-ray diffraction pattern, we may determine the materials crystalline and its crystal structure. The different crystals show its characteristic {2θ hkl}. In real application, the single crystal and polycrystalline are used for distinguish the material x-ray diffraction pattern.

XRD analysis

The x-ray diffraction data was measured by Bede D1, which is high resolution x-ray characteristic instrument from NDL. The x-ray instrument is both with high current (50mA) and low current (2mA) beams with acceleration voltage about 40KV. The operation power is from 80W to 2000W. The system is also contained with graphite monochromator, dual channel analyzer crystal, and double crystal channel. The resolution is 5, 12, 25 arc sec on different channel detector.

P-10 intro.

The P-10 Surface Profiler is a high-sensitivity surface profiler that measure micro-roughness, waviness, and step height in a variety of applications. It features the

ability to measure micro-roughness with 1Å resolution over short distances as well as waviness over a full, 60-mm scan.

The P-10 provides the following features: Measurement of vertical features ranging from under 100Å to approximately 0.3 mm, with a vertical resolution of 1 or 25Å. In addition, the profiling performance such as scan length, scan speed, sample rate….etc., as shown in Table X.

4-probes intro.

The four-probes (Type: 280p) is manufactured by Four Dimensions Inc. It is none- gas requirement, and the sample substrate is p-type or n-type Si wafer. The substrate size is larger 5cm$_X$5cm.
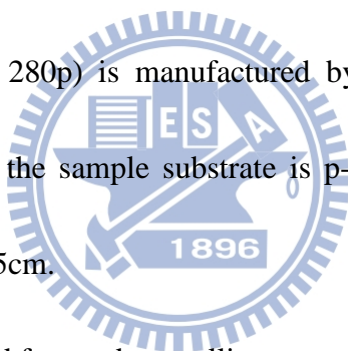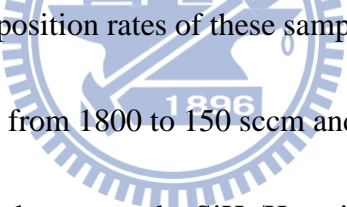
The Si thin film with void free and crystalline around 50-70% is achieved. Finally, high quality Si thin films with low sheet resistance (~order of 10 kΩ/$\square$) and crystalline around 70% are achieved. The p-type Si thin film with low sheet resistance (9.7 kΩ/$\square$) and 66% Xc can be deposited under deposition rate of 8.0Å/s, and the n-type Si thin film with low sheet resistance (13.0 kΩ/$\square$) and 69% Xc can be deposited under deposition rate of 5.6 Å/s.

2.2 Intrinsic Si Film Deposition

First, we tried to deposit intrinsic Si (i-Si) thin films. It is important part of HIT solar cell. For mass production of HIT solar cell, the requirements of i-Si film are high deposition rate, high quality, and well-controlled crystalline (Xc), as shown in the Table 5. The Xc of i-Si films by Raman spectrum, as the Fig. 26 shown. Therefore, depends on the position of Raman peak, we can calculate Xc by Eq. 2. [43]

$$Xc(\%)=(I_{510}+I_{520})/(I_{480}+I_{510}+I_{520}) \qquad Eq\ 2.$$

In our experiment, the deposition rates of these samples are as high as 9.5~11.4 Å/s. We changed the H_2 flow from 1800 to 150 sccm and fixed the SiH_4 flow rate at 30 sccm, the crystalline (Xc) changes as the SiH_4/H_2 ratio, which changes from 85 to 0 %. It indicates that we can control the Xc well by change the of SiH_4/H_2 ratio. In Fig. 27, the plan-view and cross section SEM images Si films were shown, which Si film were void free and the Xc were around 50% to 70%.

2.3 P-type/N-type Si Film Deposition

2.3.1 Optimization of [P] concentration for Si thin-film for HIT solar cell

In these experiments, we based on experiment of deposition i-Si film. We

optimized the n-type Si thin film, and adjusting its doping concentration by changing

PH_3 flow rate. We deposited n-type Si films under a substrate temperature and the

plasma power were set to 200°C, and 300W. The deposition pressure was around

4Torr, and the deposition time was 200 sec. In these serious, the $[SiH_4]$ / $[H_2]$ was

fixed at 15/800 sccm, and the $[PH_3]$ was changed as 1, 3, 5, 8, 10 sccm. The

deposition rates of these n-type Si thin films were around 6 Å/s. As the Table 6

respectively, we found that the Xc changed with the changes of $[PH_3]$. The higher

$[PH_3]$ flow rate will result in a Si film with lower Xc. From Raman spectrum, as

shown in Fig. 28, the $[PH_3]$ flow rate increased from 3 sccm to 5sccm, and 8 sccm

(A02/A03/A04), the Xc were decreased from 72.4% to 71.8%, and 66.6%. The

reduced of Xc may also be found in XRD spectrum, which XRD signals were also

decreased with the increase of $[PH_3]$ flow rate, as shown in Fig. 29. Besides, the

relationship of sheet resistance (Ω/□) and $[PH_3]$ flow rate was also shown in Fig. 30.

The sheet resistance decreases when the $[PH_3]$ flow rate increased. A drastically

reduce of sheet resistance was found, when the $[PH_3]$ flow rate was over 8 sccm. A

lowest reduce sheet resistance may be as low as 13.3 Ω/□, when a $[SiH_4]/[PH_3]$ ration

was around 15/8 sccm.

In addition, we can observe the relationship of deposition rate and [P]

concentration. As shown in the Fig. 31, the deposition rate (D.R.) increased with

increases of [PH$_3$] flow rate. The relationship of Xc and [P] concentration is the same as Fig. 30 shown. However, when the [PH$_3$] flow rate is higher than 8 sccm, as high as 10 sccm. The sheet resistance will not be further reduced, but increased to 35.7 $\Omega/\square$. That implied the higher [PH$_3$] flow rate may induce a doping poisoning in thin film growth. That will impacts film quality and introduce defects in Si film.

Consequently, we choose three deposition conditions (A02/A03/A04) for solar cell n-type contact layer. We measured dark IV curves of these three devices, as shown in Table 7. The dark IV analysis was shown in Fig. 32, and Fig. 33. As shown in these two figures, when the [PH$_3$] flow rate increased, the on-current (I$_{on}$) also increased. We may also found that the device off state current (I$_{off}$) can also be kept the same in higher [PH$_3$] flow rate.

From the summary of Fig. 34, a better on-current (Ion) may be achieved when the [PH$_3$] flow rate increase. In addition, Fig. 35 showed the 1/R, which extra plot from the slope of Ion current vs. voltage, may be increased, when the [PH$_3$] flow rate increases.

2.3.2 Optimization H$_2$ flow for growth Si thin-film of HIT solar cell

In this section, we optimized the n-type Si thin film by adjusting the H$_2$ flow. The [SiH$_4$] / [PH$_3$] flow rate was fixed as 15/8 sccm, and the [H$_2$] flow rates were changed

from 300 to 2000 sccm. The deposition rates of these with a n-type Si thin films are around 4.5~6 Å/s. As shown in the Table 8, the Xc changed as a function of [H$_2$] flow rate. Higher [H$_2$] flow rate, the Si film showed a higher Xc. From Raman spectrum (Fig. 36), when the [H$_2$] flow rates increased from 800/1000/1200 sccm (B03/B04/B05), the Xc were increased from 68.7% to 72.4% and 79.1%. In XRD spectrum (Fig. 37), all Si films show a significant (111) and (220) orientation signals. According to these results, we can observe the relationship of sheet resistance and H$_2$ flow. As shown in Fig. 38, sheet resistance decreases when the H$_2$ flow increased from 300 sccm to 800 sccm, under a fixed [SiH4]/[PH3] ratio around 15/8 sccm. However, when the [H$_2$] flow rate is higher than 800 sccm, the sheet resistance will not increase with high [H$_2$] flow rates, which were as high as 1000 sccm to 2000 sccm. In other words, sheet resistance had a inflection point at [H$_2$] flow rate around 800 sccm. It may reveal that the higher [H$_2$] flow rate was not good for doping incorporate or activation in Si film.

Besides, the deposition rate (D.R.) decreased when the H$_2$ flow increased, and the Xc will monotonically increased with the increase of H$_2$ flow rate, as shown in Fig. 39. In order to improve the doping efficiency in the Si film, a higher [SiH$_4$] flow rate may be also required in higher [H$_2$] flow rate.

2.3.3 Optimization of [B] concentration Si thin-film for HIT solar cell

Finally, we tried to optimize of the p-type Si thin film by adjusting the $[B_2H_6]$ flow rate. The deposit condition were under a substrate temperature and a plasma power about 200℃, 330W. The deposition pressure was setted to 4 Torr, and the deposition time was 200 sec. The $[SiH_4]$ / $[H_2]$ flow rate was fixed as 15/1200 sccm, and $[B_2H_6]$ is changed from 1 sccm to 10 sccm. The deposition rates of these p-type Si thin films were around 7.2~7.8 Å/s. As shown in the Table 9, the Xc changed as a function of $[B_2H_6]$. With a higher $[B_2H_6]$, the Si films show a lower Xc. From Raman spectrum (as shown in Fig. 40), when the $[B_2H_6]$ increased from 3 sccm to 5 sccm and 8 sccm (C02/C03/C04), the Xc decreases (54.6%/ <50%/ amorphous). According to these results, we can observe the relationship of sheet resistance and $[B_2H_6]$ flow rate, as shown in Fig. 41, the sheet resistance (S.R.) increased when the $[B_2H_6]$ flow rate increased in low $[B_2H_6]$ flow rate. Under a fixed $[SiH_4]$ and $[H_2]$ flow rate, when we increased the $[B_2H_6]$ flow rate as high as 5sccm or more, the Xc will significant degraded and even disappeared. The film will lose its crystalline when the $[B_2H_6]$ flow rate is high, as shown in Fig. 41 and Fig. 42. The amorphous type p-type Si film may be observed, as shown in the Raman spectrum and the sheet resistance will drastically jump to the order of 1G $\Omega/\square$. Besides, the Xc will be reduced when the $[B_2H_6]$ flow rate increased.

2.3.4 Optimization H$_2$ flow for Si thin-film growth of HIT solar cell (p-type doped Si film),

In order to optimize the p-type Si thin film, we tried to adjust the [H$_2$] flow rates to improve its crystalline. The deposition conditions were the same as previous section. The [SiH$_4$] / [B$_2$H$_6$] flow rate was fixed as 15/5 sccm, and the [H$_2$] flow rate was changed from 300 sccm to 2000 sccm. The deposition rates of these p-type Si thin films are around 8~9.3 Å/s. As shown in the Table 10, the Xc may be changed the [H$_2$] flow rate. The Si film with higher [H$_2$] flow rate will show a higher Xc. At the same condition, the sheet resistance may be further induced from 200 kΩ/□ to less than 10 kΩ/□. From Raman spectrum (Fig. 43), [H$_2$] flow rate increased from 1200/1600/2000 sccm (D05/D06/D07), the Xc increased (<50% /66.1% /73.2%). From the XRD spectrum (Fig. 44), the XRD signal of Si film will also be enhanced with higher [H$_2$] flow rate. According to these results, we can observe the relationship of sheet resistance and H$_2$ flow, as shown in Fig. 45. The sheet resistance (S.R.) decreased when the H$_2$ flow rate increased, the deposition rate also decreased with the increase of [H2] flow rate, as shown in Fig. 46.

2.3.5 Optimization of growth Si thin-film for HIT solar cell (p-type / n-type Si)

In summary, we can optimize the doped (p-type / n-type) Si thin film with high deposition rate (>5 Å/s) and low sheet resistance (<10 kΩ/□), under well-controlled crystalline (Xc) around 60~70%, as shown in the Table 11. From Raman spectrum (Fig. 47 (a) and Fig. 47 (b)), we can observe the Xc of n-type Si thin film as about 69%, and p-type Si thin film was about 66%. Therefore, doped (p-type / n-type) Si film with low sheet resistance (~order of 10 kΩ/□) and crystalline around 70% is achieved. The SEM images showed that the doped Si thin films were with grains and clear column shape and void free, as shown in Fig. 48 (a)、(b).

Chapter 3

HIT Solar Cell Simulation & Deposition Optimization

3.A HIT Solar Cell Simulation

3.A.1 Introduction

In this context, we used AMPS-1D to simulate HIT solar cell performance for deposition optimization. First, we can know the relationship of i-a-Si film thickness and efficiency of HIT solar cell by AMPS-1D. The optimization of i-a-Si film thickness. The relationship of doping concentration and efficiency of HIT solar cell, and the cap layer doping concentration in HIT solar cell. Finally, the relationship of defect density and efficiency of HIT solar cell can be verified. As the result, we can find optimization parameter to deposit HIT solar cell by AMPA-1D simulation. Then, we introduced the HIT solar cell fabrication in 40.68MHz VHF-PECVD.

3.A.2 HIT Solar Cell Structure Simulation (AMPS-1D)

3.2.A.2.1 i-a-Si Film Thickness vs. Efficiency

In this study, we used AMPS-1D to simulate HIT solar cell performance by adjusting its i-a-Si film thickness, as shown in Fig. 49. When the i-a-Si film thickness was increased from 1 nm to 5 nm, the solar cell efficiency was increased from 13.91 % to 14.05 %. We can see this result in photo I-V curve, as shown in Fig. 50. Further,

when the i-a-Si film thickness was increased from 5 nm to 20 nm, the solar cell

efficiency was degraded from 14.05 % to 12.17 %. We can also see this result in

photo I-V curve, as shown in Table 12. As the result, when the i-a-Si film thickness

was 5 nm, the maximum HIT solar cell efficiency was achieved, as shown in Fig. 51

(a). However, when the i-a-Si film thickness was increased from 5 nm to 20 nm, the

fill factor (F.F.) was decreased from 0.851 to 0.745, and the efficiency also dropped.

The Fig. 51 (b) also showed this trend. The short circuit current density (Jsc) and open

circuit voltage (Voc) didn't change significantly when the i-a-Si film thickness was

increased[44].
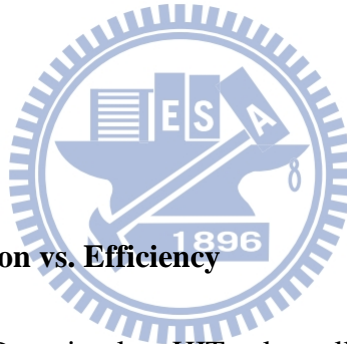
3.2.A.2 Doping concentration vs. Efficiency

Now, we used AMPS-1D to simulate HIT solar cell performance by adjusting the

doping layer's concentration, as shown in Fig. 52. When the doping concentration

was increased from 10^{15} cm^{-3} to 10^{21} cm^{-3}, the solar cell efficiency was increased from

10.86 % to 13.14 %. We can see this result in photo I-V curve, as shown in Fig. 53. In

addition, when i-a-Si film thickness was increased, the fill factor (F.F.) and the open

circuit voltage (Voc) were also increased. The F.F. was increased from 0.787 to 0.846,

and the open circuit voltage (Voc) was increased from 0.638 V to 0.728 V, as shown

in Table 13. The Fig. 54 also showed this trend. Especially, when the doping

concentration was over 10^{19} cm^{-3}, the HIT solar cell efficiency, F.F. and Voc were

increased significantly, as Fig. 54 (b)、(c). shown.

3.2.A.3 Defect density vs. Efficiency

Now, we used AMPS-1D to simulate HIT solar cell performance by adjusting its

defect density (localized bonded states), as shown in Fig. 55. When the defect density

was increased from 10^{15} cm^{-3} to 4×10^{19} cm^{-3}, the solar cell efficiency was decreased

from 11.587 % to 3.426 %. We can see this result in photo I-V curve, as shown in Fig.

56. In addition, when defect density was increased, the fill factor (F.F.) and the open

circuit voltage (Voc) were both decreased. The F.F. was decreased from 0.807 to

0.458, and the open circuit voltage (Voc) was decreased from 0.664 V to 0.374 V, as

shown in Table 14. The Fig. 57 also showed this trend. Especially, when the defect

density was less then 10^{16} cm^{-3}, the HIT solar cell efficiency, F.F. and Voc were better,

as Fig. 57. shown.

3.B HIT Solar Cell Layer Growth

The structure of p-type wafer HIT solar cell and the corresponding energy

bandgap are shown in Fig. 58. According to the literature [X], intrinsic amorphous Si

(i-a-Si) film was firstly deposited on both sides of p-type c-Si substrate. Then, the

n-type a-Si films were deposited on i-a-Si. In other words, n-type amorphous Si (n-a-Si) film was deposited on the front side, and p-type amorphous Si (p-a-Si) film was deposited on the back side. It is symmetric structure with different contact layer. Finally, the ITO was on the top of HIT solar cell.

Now, we tried to deposit HIT solar cell by using VHF-PECVD (40.68MHz) in ITRI. The VHF-PECVD, as shown in Fig. 59, was mentioned in chapter 2. First, we deposited single side HIT solar cell, then, the double side HIT solar cell was made, as shown in Fig. 60.

For HIT solar cell deposition, we used a p-type c-Si wafer with double-side polished. The wafer is also <100> oriented, 250 ± 25 nm thick, and 0.5-5 Ω cm. Before deposition, we used standard RCA clean to remove the particles and the native oxide on c-Si wafer surface. Before deposition, a dilute hydrofluoric acid (DHF) (1% in DI water, 1min) was used to remove the surface oxide. We in-situ deposited an intrinsic a-Si layer, and a n-type doped a-Si layer. Then, a ITO layer was fully deposited on c-Si substrate. The electrodes (Ti/Ag) were also evaporated on both sides: n-a-Si layer and c-Si substrate. In front of the wafer, we used a mask to pattern the top electrodes.

In this experiment, we deposited two types of HIT structure for electrical measurement. First, it is the single side device, which was used for deposition a-Si films and optimized its structure. The single side HIT solar cell fabrication was shown

in Fig. 61. The other is a double side HIT solar cell, which was with a highly doped

p-type a-Si film for back side contact. The double side HIT solar cell is a full structure

of HIT solar cell, we may also measure the device under light illumination. The

double side HIT solar cell fabrication was shown in Fig. 62 [45,46]
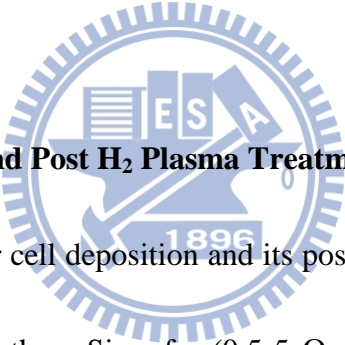
Chapter 4

Part A: Post H$_2$ Plasma Treatment Process on HIT solar cell

4.1 Introduction

In this chapter, we proposed a process to improve HIT solar cell performance. We used a post H$_2$ plasma treatment on HIT solar cell[47]. The device performance, both dark IV curves and photo IV curves were verified in this chapter. Finally, we also used the external quantum efficiency (E.Q.E.) measurement on HIT solar cell to observe the changes of HIT solar cell after treatment.

4.2 Solar Cell Deposition and Post H$_2$ Plasma Treatment Process

The single side HIT solar cell deposition and its post H$_2$ plasma treatment process was shown in Fig. 63, first, the c-Si wafer (0.5-5 Ω cm, 250±25 nm thick, <100> oriented) was treated by standard RCA clean. In our standard process, before the a-Si deposition, the wafers were etched in diluted hydrofluoric acid (DHF) (1% in DI water, 1min). The doped and un-doped intrinsic amorphous (a-Si) thin films were deposited on c-Si wafers by VHF-PECVD system under a temperature about 200℃. The plasma power during the thin film deposition was set to around 90~300W, and the deposition pressure was 0.7~6 Torr. In addition, the SiH$_4$ flux was varied from 0 to 50 sccm and the H$_2$ flux is also varied from 0 to 2000 sccm for the un-doped Si thin

film. For the doped Si films, the B_2H_6 or PH_3 flux is adjusted around 2~10 sccm during the film deposition. After the thin film deposition, post hydrogen (H_2) plasma treatment was used. The anneal temperature was around 200℃, and the adjustable H_2 flux was around 50~2000 sccm. In addition, usable the post-anneal plasma power and pressure were around 0.7~6 torr and 90~400W, respectively. Then, the ITO layer was deposited at the same temperature as Si thin film deposition. The solar cell is finished by evaporating metal electrode Ti/Ag. The front and backside contacts are formed by E-gun deposition system[48].

The double side HIT solar cell deposition and its post H_2 plasma treatment process was shown in Fig. 64. The process was mentioned in chapter 3, and the process parameters were the same as single side HIT solar cell. The difference of single side HIT solar cell and double side HIT solar cell was from i-a-Si film on the backside[49].

For the analysis of the layer, the thin-film thickness and sheet resistance in this device are measured by surface profile (Dektak IIA) and four-point probe (NAPSON RT-7), respectively. The dark I-V of HIT solar cell is measured by HP4156. The photo I-V of HIT solar cell is measured by full spectrum solar simulator (Oriel class A, 91160A, Newport Corporation). And, the external quantum efficiency (E.Q.E.) curves are measured by IPCE (Incident photon conversion efficiency, ENLI, EQE-D-3011,

ENLI Technology Co, Ltd).

4.3 Dark IV Curves on HIT Solar Cell

4.3.1 Post H_2 plasma treatment under different ambient condition (Optimization of H_2 flux)

In order to optimize the post-anneal H_2 plasma treatment, several parameters were fine-tuned in this article, such as H_2 flux, plasma power, ambient pressure, and H_2 treatment time. First, we adjusted the H_2 flux of post-anneal H_2 treatment under different H_2 flux (600sccm, 1200sccm). The dependence of device characteristics and performance (dark I-V curves) under different H_2 flux were shown in Table 15 and Fig. 65 (a)、(b). In Table 15, the V_{on} can be improved when using the H_2 treatment, simultaneously the I_{on} and I_{off} did not be changed. The V_{on} is 0.440V when H_2 flux is 600sccm. Besides, when the H_2 flux is increased to a double value (1200 sccm), the V_{on} is decreased to 0.309V. According to the literature, hydrogen atom can passivate the Si surface and repair Si-Si dangling bonds [50,51]. But a large amount of hydrogen will damage (or etch) the surface. Therefore, using moderate H_2 flux of post-anneal H_2 treatment can change the device performance.

4.3.2 Post H_2 plasma treatment under different plasma condition (Optimization of Plasma Power)

Then, the H_2 plasma treatment under different plasma power and ambient pressure were proceeded on HIT devices. First, we showed the dependence of HIT characteristics (dark I-V curves) under various plasma power and post H_2 plasma treatment. The dark I-V curves were shown in Fig. 66 (a)、(b). As summarized in Table 16 and Fig. 67, the V_{on} and I_{off} can be well controlled, when the power was controlled in the range from 100W to 200W under 4 torr. The V_{on} was increased from 0.477V to 0.514V and the I_{off} was decreased from 3.27×10^{-9} A to 7.49×10^{-10}A when the power was lowered from 200W to 150W and 100W (sample D~F). In comparison with the baseline sample A, without post-anneal H_2 plasma treatment, sample F has better performance (lower I_{off} and higher V_{on}) in this power-depdendent H_2 plasma treatment. According to sample F, we further controlled pressure of post-anneal H_2 treatment (under 100W).

4.3.3 Post H_2 plasma treatment under different pressure condition (Optimization of Process Pressure)

In Table 17, the dark I-V performance (I_{on}, I_{off}, and V_{on}) can be also well controlled when the pressure in the range from 2.25 torr to 0.75 torr. The V_{on} was increased from 0.492V to 0.547V, the I_{off} was decreased from 6.88×10^{-10} A to 5.59 $\times 10^{-10}$A, and the I_{on} was increased from 2.44×10^{-6} V to 8.48×10^{-6}V when the pressure

of H_2 treatment was decreased from 2.25 torr to 0.75 torr. Sample I has better performance (higher I_{on}、V_{on} and lower I_{off}), which was treated with low plasma power and low ambient pressure. We also know from the dark I-V curve in Fig.68 (a)、(b). In addition, according to Fig. 68, when the plasma power of H_2 treatment was decreased to 100W, the V_{on} was as high as ~0.515 V(0.514 V) and I_{off} were low to ~10^{-9} A (7.49×10^{-10}). Fig. 69 shows the V_{on} and I_{off} were dependent on various pressures. When the pressure was decreased to 0.75 torr, the V_{on} and I_{on} were as high as ~0.55 V (0.547 V) and ~8.5×10^{-6} A (8.48×10^{-6}), respectively. Therefore, we can know low-power and low-pressure of post-anneal H_2 treatment on HIT solar cell can obtain better dark I-V performance.
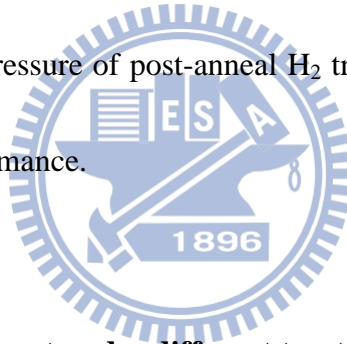
4.3.4 Post H_2 plasma treatment under different treatment time (Optimization of Treat Time)

Additionally, the H_2 treatment time was also be to controlled for obtaining a better post-anneal result. First, we showed the dependent of dark I-V curves of HIT device as a function of H_2 treatment time. As summarized in Table 18 and Fig. 70, when the H_2 plasma treatment time is more than 20sec, the V_{on} can be increased, at the same time, the I_{on} and I_{off} will not be changed significantly. As H_2 treatment time increased from 40 to 60 second, the V_{on} can be increased as high as 0.6V, and I_{off} was still as

low as 6×10^{-9} A. Furthermore, we prolonged the H_2 treatment time to 100 sec, the V_{on} will be dropped, the I_{on} and I_{off} were decreased. So, the moderate H_2 plasma treatment time is around 40 to 60sec. In this time, the post-anneal H_2 treatment effect reaches saturation. In addition, according to Fig. 71, a longer H_2 plasma treatment time (100sec) degrading the HIT solar cell performance (V_{on}) had been proven again. Therefore, moderate time, low-power, and moderate H_2 flux of post-anneal H_2 plasma treatment can improve device performance.

4.4 Photo IV Curves on HIT Solar Cell

In this part, we used the solar simulator to measure the HIT solar cell efficiency. The solar simulator was in NTHU (Center for Nanotechnology, Materials Science, and Microsystems), as shown in Fig. 72. The system provided full spectrum solar simulator with beam size around 2 x 2 in. (51 x 51 mm). The solar simulator was used 300 W Xenon (Short Arc) as light source, and the collimation was less then ±10°.

4.4.1 Post H_2 plasma treatment on HIT solar cell (Photo-IV Curve: Single Side)

From the photo IV curve (Fig. 74), we summarized the HIT solar cell performance, in Table 19. When we used the post H_2 plasma treatment on single side HIT solar cell,as shown in Fig. 73,   the efficiency and F.F. were increased. The efficiency was

increased from 2.42 % to 3.67 %, and the F. F. was increased from 25.3 to 39.5.

Therefore, post H_2 plasma treatment improved single side HIT solar cell efficiency

1~2%, and F. F. was increased significantly.

4.4.2 Post H_2 plasma treatment on HIT solar cell (Photo-IV Curve: Double Side)

Further, we compared the post H_2 plasma treatment on double side HIT solar cell,

as shown in the Fig. 75. From the photo IV curve (Fig. 76), we summarized the HIT

solar cell performance, in Table 20. When we used post H_2 plasma treatment on

double side HIT solar cell, the solar cell performance (Voc, Jsc, F.F. and η) was

increased. The efficiency (η) was increased from 5.17 % to 8.05 %, Voc was

increased from 0.75 V to 0.90 V, Jsc was increased from 13.92 mA/cm^2 to 14.68

mA/cm^2, and F. F. was increased from 49.5 to 61.0.

4.5 HIT Solar Cell n-a-Si / i-a-Si Layer Thickness Optimization & Post H$_2$ Plasma Treatment and Their External Quantum Efficiency (E.Q.E.) measurements

4.5.1 Post H$_2$ plasma treatment on reduced i-a-Si layer HIT solar cell (Photo-IV Curve: Double Side)

Further, we measured double side HIT solar cell with different i-layer (i-a-Si film) thickness, as shown in Fig. 77. From the photo IV curve (Fig. 78), we obtained the HIT solar cell performance, as the Table 21. shown. When we reduced i-layer (i-a-Si film) thickness of double side HIT solar cell, the solar cell performance (Voc, Jsc, F.F. and η) was increased. The efficiency (η) was increased from 5.74 % to 8.05 %, Voc was increased from 0.74 V to 0.90 V, Jsc was increased from 13.62 mA/cm^2 to 14.68 mA/cm^2, and F. F. was increased from 57.0 to 61.0.

4.5.2 Post H$_2$ plasma treatment on reduced n-a-Si layer HIT solar cell (Photo-IV Curve: Double Side)

We verified double side HIT solar cell performance with different n-layer (n-a-Si film) thickness, as the Fig. 79 shown. From the photo IV curve (Fig. 80), we obtained the HIT solar cell performance, as shown in Table 22. When we reduced i-layer (i-a-Si film) thickness of double side HIT solar cell, the solar cell performance (Voc, Jsc, F.F.

and η) was increased. The efficiency (η) was increased from 8.99 % to 9.56 %, Voc was increased from 0.90 V to 0.91 V, Jsc was increased from 14.11 mA/cm^2 to 14.32 mA/cm^2, and F. F. was increased from 70.8 to 73.3.

From previous study, we may found the post H_2 plasma treatment can improve HIT solar cell significantly. By combining i-layer and n-layer thin-down in HIT solar cell, we may obtain a higher HIT solar cell efficiency around 9.6 % with post H_2 plasma treatment. The optimized HIT solar cell were also used for following experiments and discussing.

In this part, we introduced the external quantum efficiency (E.Q.E.) spectrum to measure the HIT solar cell efficiency. The external quantum efficiency was also in NTHU (Center for Nanotechnology, Materials Science, and Microsystems), as shown in Fig. 81. The operation wavelength range was from 350 nm to 1100 nm with adjustable wavelength interval from 1 nm to 50 nm (Default 5 nm). For current measurement, an amplifier with chopping frequency from 4 kHz to 5 kHz (MCU controlled) was used. The S/N ratio was larger then 500, and its precision (error bar) was less then 2% with repeatability > 95%. In addition, the auto Jsc calculation with reference solar spectrum or consumer input.

4.5.3 External Quantum Efficiency (E.Q.E.) measurements

Further, we measured the E.Q.E. (%) on double side HIT solar cell, which were

with and without post H_2 plasma treatment, as shown in Fig. 82. From the photo IV

curve (Fig. 83), we obtained the HIT solar cell performance, as shown in Table 23.

When we introduce the post H_2 plasma treatment on double side HIT solar cell, the

solar cell performance (Voc, Jsc, F.F. and η) was increased. The efficiency (η) was

increased from 8.78 % to 9.56 %, Voc was increased from 0.90 V to 0.91 V, Jsc was

increased from 13.82 mA/cm^2 to 14.32 mA/cm^2, and F. F. was increased from 71.0 to

73.3.

The measured external quantum efficiency (EQE) curves can also explain the

characteristic of the photo current after H_2 plasma treatment. As shown in Fig. 84, the

HIT solar cell with post H_2 plasma treatment showed a higher E.Q.E., especially in

the wavelength in 600nm to 900nm. It can be seen in Table 24A and 24B. However, in

the short wavelength region, the H_2 plasma treated HIT solar cells showed a lower

E.Q.E. It has been reported the short wavelength E.Q.E. present the front contact

characteristics, and the longer wavelength E.Q.E. present the solar cell bulk or

interface characteristics[52]. The result implied the photo current enhancement was

mainly come from the intrinsic layer and bulk-side photon absorption or photo-current

generation, but not from the top-side layer improvement, which side is close to photon

incident[53].

Chapter 4B

Process Improvement (II): Rapid Thermal Annealing (RTA) on HIT solar cell

4.6 Introduction

In this chapter, we continue to improve the HIT solar cell process by using Rapid Thermal Annealing (RTA) on HIT device. First, we introduce post RTA process. And we compared the effects of RTA on diode structure (single side HIT solar cell) and HIT solar cell(double side HIT solar cell)[54]. Finally, the summary about performance enhancement of solar cell characteristic were be shown.
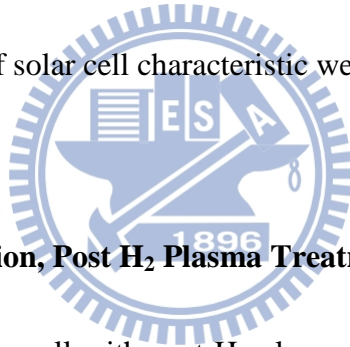
4.7 HIT Solar Cell Deposition, Post H_2 Plasma Treatment Process and RTA

The single side HIT solar cell with post H_2 plasma treatment were used for RTA treatment shown in Fig. 85. The process of deposition and post H_2 plasma treatment was as mentioned in chapter 4. In addition, the double side HIT solar cell were also deposited for RTA treatment, and the process parameters were the same as single side HIT solar cell, as shown in Fig. 86.

Then, we used rapid thermal annealing (RTA) to improve the HIT solar cell performance. The RTA temperature was $200\,^\circ\text{C}$, $250\,^\circ\text{C}$, $300\,^\circ\text{C}$, and $350\,^\circ\text{C}$ under 3 sccm N_2 gas. The RTA time was 30sec.

4.8 RTA on HIT solar cell

4.8.1 Test on Single Side Device

In order to find out the suitable annealing temperature for HIT solar cell, the RTA

temperature was split as 200℃, 250℃, 300℃, and 350℃. The annealing ambient was

under 3 sccm N_2 gas, and the RTA time was 30sec. After annealing, we measured the

dark IV curves of single side HIT solar cells and analyze the performance of the HIT

solar cells under various RTA temperature. From the dark IV curves (Fig. 87), the

HIT solar cell under 250℃ RTA temperature has better dark IV performance. As the

result, the RTA temperature was over 250℃, and the p/n junction abruptness may be

damaged.
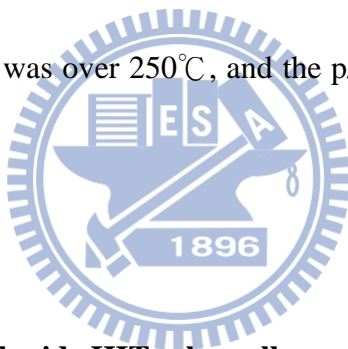
4.8.2 RTA process on double side HIT solar cell

From previous study, the low temperature RTA (<250℃) may be suitable

annealing temperature for HIT solar cell. Thus, the RTA temperature was set to from

150℃ to 250℃ for improving HIT solar cell performance.

After annealing, we compared five HIT solar cells, the as-deposited cell, and annealed

cells under 150℃, 180℃, 200℃, and 250℃. We measured these double side HIT

solar cells. From the photo IV curve (Fig. 88), we obtained the HIT solar cell

performance, as summarized in Table 25 shown. First, we compared the double side

HIT solar cell with or without RTA treatment. When we used the RTA treatment (from 150℃ to 200℃ RTA temperature) on the double side HIT solar cell, the solar cell performance (Jsc and η) was increased. The efficiency (η) was increased from 8.78 % to 9.59 %, and Jsc was increased from 13.82 mA/cm^2 to 15.34 mA/cm^2. Voc was the same as 0.90 V, both the F. F. wasn't changed significantly.

Further, when we increased the RTA temperature from 200℃ to 250℃ on the double side HIT solar cell. The solar cell performance (Voc, Jsc and η) was decreased. The efficiency (η) was decreased from 9.59 % to 8.88 %. Voc was decreased from 0.90 V to 0.88V, and Jsc was also decreased from 15.34 mA/cm^2 to 14.32 mA/cm^2.

It may imply the higher RTA temperature may result in higher thermal budget on HIT solar cell. Thus, the p-n junction abruptness may be damaged and lowered the photo current generation[55]. Hence, a lower photo current was found in HIT solar cell with RTA 250℃ annealing than in 200℃.

Then, we also used rapid thermal annealing (RTA) to improve the HIT solar cell with post H$_2$ plasma treatment. The RTA temperature was 150℃, 180℃, 200℃, and 250℃ under 3 sccm N$_2$ gas. The RTA time was 30sec.

We measured these double side HIT solar cells. From the photo IV curve (Fig. 89), we obtained the HIT solar cell performance, as the Table 26. shown. First, we

compared the double side HIT solar cell with or without RTA treatment. When we

used RTA treatment (from 150°C to 200°C RTA temperature) on the double side

HIT solar cell, the solar cell performance (Jsc and η) was increased. The efficiency

(η) was increased from 10.00 % to 11.07 %, and Jsc was increased from 14.96

mA/cm^2 to 17.36 mA/cm^2. Voc was increased from 0.90 V to 0.91V.

Further, we increased the RTA temperature on the double side HIT solar cell from

200°C to 250°C. The solar cell performance (Jsc and η) was decreased. The

efficiency (η) was decreased from 11.07 % to 10.23 % , and Jsc was also decreased

from 17.36 mA/cm^2 to 15.09 mA/cm^2. The higher thermal budget resulted in lower

HIT solar cell efficiency were also found.
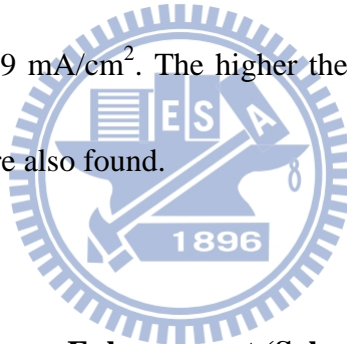
5.3.4 Summary of Performance Enhancement (Solar Cell Characteristic)

Finally, we also summarized these results of double side HIT solar cells with or

without post H$_2$ plasma treatment or RTA treatment, as the Table 27 shown. When we

used post H$_2$ plasma treatment on HIT solar cell, the efficiency was increased from

5.17 % to 8.05 %. Voc was increased from 0.75 V to 0.90 V, and Jsc was increased

from 13.92 mA/cm^2 to 14.68 mA/cm^2. In addition, F. F. was increased from 49.5 to

61.0. Therefore, post H$_2$ plasma treatment can improve HIT solar cell performance

significantly.

Then, we reduced the i-a-Si/n-a-Si (i/n-layer) film thickness of double side HIT solar cells under post H_2 plasma treatment. When we reduced the i-a-Si/n-a-Si (i/n-layer) film thickness, the solar cell performance was increased. The efficiency was increased from 8.05 % to 9.56 %. Voc was increased from 0.90 V to 0.91 V, and F. F. was increased from 61.0 to 73.3. Therefore, reduced the i-a-Si/n-a-Si (i/n-layer) film thickness of HIT solar cells can improve HIT solar cell performance.

Further, we used RTA treatment on HIT solar cell with thinner i-a-Si/n-a-Si (i/n-layer) film thickness under post H_2 plasma treatment. When we used RTA treatment, the solar cell performance was increased. The efficiency was increased from 9.56 % to 11.07 %, and Jsc was increased from 14.32 mA/cm^2 to 17.36 mA/cm^2. Voc was the same as 0.91 V. Thus, we concluded that a high performance HIT solar cell may achieve by using：(1) post H_2 plasma treatment (2) HIT solar cell structure optimization, and (3) post RTA annealing in low temperature.

Chapter 5

Conclusion

In this work, we optimized HIT solar cell structure for epi layer thickness and layer doping concentration. Then we proposed the new process method for post hydrogen (H_2) plasma treatment to improve HIT solar cell performance, and further enhanced HIT solar cell efficiency by RTA treatment. Finally, the solar efficiency can achieve to 11.1%.

First, we deposited the intrinsic Si (i-Si) thin films and doped Si thin films by using 40.68MHz VHF-PECVD. In order to enhance deposition rate of Si film, we used the very high frequency plasma enhances chemical vapor deposition (40.68MHz VHF-PECVD), which located in ITRI Lab. The plasma frequency was increased from 13.56 MHz to 40.68MHz so that the deposition rate can be increased ($> 8\text{Å} / \text{sec}$) and the quality of Si epi layer was still well. In addition, the higher deposition rate resulted in lower gas consumption.

In these series of i-Si thin film experiment, we deposited high quality Si epi layer with void free and well controlled the crystalline around 50-70%. The Raman spectrum we showed in this report was from Horiba HR800 system, which system had two Laser sources: He/Ne Laser (wavelength: 632.8 nm) and Ar Laser (wavelength: 514.5 nm). We used the longer wavelength He/Ne Laser to reduce the possibility of Si

films crystalline caused by Laser anneal. In addition, the absorption coefficient of longer wavelength Laser was smaller than shorter one. Therefore, the He/Ne Laser penetrated more deeply than Ar Laser, and got more Si film information. Further, we used 2400 grating to increase resolution, and open filter to reduce Laser intensity, preventing Laser anneal from crystallizing Si film.

In addition, the doped Si epi layer (n-uc-Si for $[PH_3]$=8 sccm and p-uc-Si for $[B_2H_6]$=5 sccm) with low sheet resistance (~order of 10 kΩ / $\square$) and crystalline around 70% were also achieved. The depositions of Si thin layer for HIT solar cells were also optimized. The SEM images showed that the doped Si thin films were with grains and clear column shape and void free.

Before depositing the HIT solar cell, we used the AMPS-1D to simulate the HIT solar cell performance. We can obtain the HIT solar cell characteristics by adjusting the HIT structure for (a) i-a-Si (i-layer) thickness, the (b) doping concentration in contact layer. Based on simulation result, the optimization thickness for i-a-Si (i-layer) in HIT solar cell was 3~5 nm and the required doping concentration in contact layer for HIT solar cell was must over 10^{19} cm^{-3}.

The simulation results were matched with experiment data, as shown later. Furthermore, an optimized HIT solar cell process and structure was then achieved.

We proposed the new method for process improvement method, according to (a)

"post H_2 plasma treatment", and (b) rapid thermal annealing (RTA). The proposed "post H_2 plasma treatment" was optimized by adjusting treatment condition, such as H_2 flux, plasma power, ambient pressure and post H_2 plasma treatment time during the "post H_2 plasma treatment"[56]. In these series of dark IV measurement, the result indicated that a low plasma power (100W), a low ambient pressure (0.75 torr), and long post H_2 plasma treatment time (50 sec) was a preferable condition to enhance the single side HIT solar cell performance. A suitable condition of post H_2 plasma treatment can increase Von (from 0.20 V to 0.59 V) and decrease I_{off} (from $\sim 10^{-7}$ A to $\sim 10^{-10}$ A) , and I_{on} (from $\sim 10^{-7}$ A to $\sim 10^{-10}$ A). In addition, long post H_2 plasma treatment time (from 10 sec to 50sec) can increase Von (from 0.36 V to 0.59V).

In the photo IV measurement on HIT solar cells, we used post H_2 plasma treatment on double side HIT solar cell. We compared HIT solar cell with or without post H_2 plasma treatment. The solar cell performance (Voc, Jsc, F.F. and η) was increased. The solar cell performance was also improved. The efficiency (η) was increased from 5.17 % to 8.05 %, V_{oc} was increased from 0.75 V to 0.90 V, Jsc was increased from 13.92 mA/cm^2 to 14.68 mA/cm^2, and F. F. was increased from 49.5 to 61.0.

According the literature, there are many Si-Si, Si-H break-bonding in a-Si layer film. In other words, there are many break-bonding defects in this layer and many

mid-states between valence band and conduction band[57] When sun shine a-Si layer, the electron and hole recombine in these defects, then recombination decrease the cell performance. That is photodegradation effect (or called "Steabler-Wronski Effect, SWE"). Therefore, we used post H_2 plasma treatment in order to improve Si solar cell efficiency performance, because the hydrogen atom can repair Si-Si break bond, and fill the vacancy between them[57]. In addition, the hydrogen atom can smooth the a-Si surface or interface, and, furthermore, reduce the photodegradation effect[57].

According the AMPS-1D simulation results, optimization of i-layer thickness in HIT solar cell is 3~5 nm. Therefore, we reduced i-a-Si (i-layer) of double side HIT solar cell, and then applied post H_2 plasma treatment on them. The solar cell performance (Voc, Jsc, F.F. and η) was increased. The efficiency (η) was increased from 5.74 % to 8.05 %, Voc was increased from 0.74 V to 0.90 V, Jsc was increased from 13.62 mA/cm^2 to 14.68 mA/cm^2, and F. F. was increased from 57.0 to 61.0.

Furthermore, according to the literature [56], the thinner cap layer (n-a-Si layer) can enhance the incident photons. Therefore, we reduced n-a-Si (n-layer) and also used post H_2 plasma treatment on them. The solar cell performance (Voc, Jsc, F.F. and η) was increased. The efficiency (η) was increased from 8.99 % to 9.56 %, Voc was increased from 0.90 V to 0.91 V, Jsc was increased from 14.11 mA/cm^2 to 14.32 mA/cm^2, and F. F. was increased from 70.8 to 73.3.

We further tried to enhance HIT solar cell efficiency by using rapid thermal annealing (RTA) treatment after all the processes of layer deposition and post H_2 plasma treatment has been done. First, in order to find out the suitable annealing temperature for HIT solar cell, the RTA temperature was split as 200℃, 250℃, 300℃, and 350℃. The annealing ambient was under 3 sccm N_2 gas, and the RTA time was 30sec. After annealing, we measured the dark IV curves of single side HIT solar cells and analyze the performance of the HIT solar cells under various RTA temperature. From the dark IV curves, the HIT solar cell under 250℃ RTA temperature has better dark IV performance. As the result, the RTA temperature was over 250℃, and the p/n junction abruptness may be damaged because the layer deposition temperature was only 200℃.
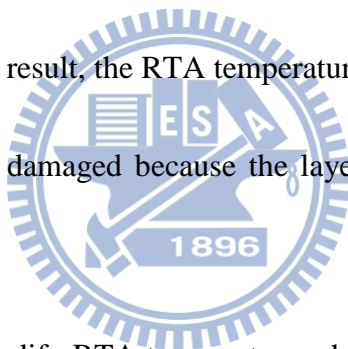
Therefore, we tried to modify RTA temperature which was from 150℃ to 250℃ was used on optimized double side HIT solar cell. When RTA temperature was 200℃, a short circuit current density (Jsc) was improved around 15.4 % (from 14.68 mA/cm^2 to 17.36 mA/cm^2) and an 13 % increased fill-factor (F. F.) were observed. Voc was increased about 1.1 % (from 0.90 V to 0.91 V). Besides, the overall efficiency increased around 27.3 % (from 8.1 % to 11.1%) was obtained. A HIT solar cell with efficiency was over around 11% was achieved with both post H_2 plasma treatment and low temperature RTA anneal.

Table List

Solar Cell Type	c-Si	poly-Si	a-Si (thin-film)	HIT
Substrate	Wafer	Wafer	Glass	Wafer
Process Tool	LPCVD	LPCVD	PECVD	PECVD
Max. Process temperature (℃)	650	650	200	150~200
Report Efficiency (%)	>16%	>14%	>8%	>18%
Absorption Wavelength (nm)	300-1100	300-1100	300-900	300-1100

Table 1 Comparisons of Si solar cells, including Si based and Si thin film solar cells. (Data source: "太陽電池 Solar Cells")
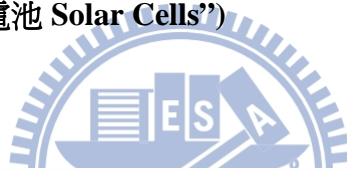
	FZ / CZ	Area	J_{sc} (mA/cm²)	V_{oc} (mV)	FF (%)	Eff (%)
Sanyo	n CZ	**100 cm²**	38,9	725	79	**22,3**
AIST	n CZ	1 cm²	33,2	628	77	16,0
HMI	n FZ	1 cm²	39,3	639	79	19,8
	p FZ	1 cm²	36,8	634	79	18,5
IMT	n FZ	0,3 cm²		682	82	19,1
	p FZ	0,3 cm²		690	74	16,3
IMEC	p FZ	1 cm²	32,2	644	80	16,5
NREL	p FZ	1 cm²	35,4	667	77	18,2

Table 2 Several companies and institutions are listed in HIT solar cell research.

(Sanyo is still far ahead of laboratories.)

	V_{oc} (V)	J_{sc} (mA/cm^2)	FF (%)	η (%)
p-type** (planar)	0.688	31.6	81.3	17.7
n-type (planar)**	0.691	33.6	72.1	16.7
p-type (textured)**	0.678	35.9	78.6	19.1
n-type (textured)*	0.664	35.3	74.5	17.2

** independently confirmed by NREL PV Performance Characterization Team

* measured by using calibrated NREL XT-10 solar simulator.

Table 3 Summary of the best double-side HIT solar cell (1cm^2) by HWCVD, fabricated at NREL.

ID	V_{oc} (V)	Structure
5-5	0.63	diffused n+/planar p-FZ/Al-BSF
16C	0.65	a-Si(n/i)/planar p-FZ/Al-BSF
1540	0.65	a-Si(n/i)/textured p-FZ/Al-BSF
2933	0.66	a-Si(n/i)/textured p-FZ/a-Si(i/p)
2930	0.69	a-Si(p/i)/planar n-FZ/a-Si(i/n)

Table 4. Effects of a-Si:H as emitter and back contact on Voc. (Data source:

Conference Paper **NREL/CP-520-38942 November 2005)**

Sample	A	B	C	D
SiH_4/H_2 ratio	30/1800	30/600	30/200	30/150
Deposition rate (Å/sec)	11.4	11.2	9.5	11.3
Crystallinity (%)	85	72	50	N.A. (a-Si)

Table 5 The deposition parameters and results of sample A, B, C, and D.

Sample ID	$SiH_4/PH_3/H_2$ (sccm)	Deposition Rate (Å/s)	Film Thickness (Å)	Sheet Resistance (Ω/□)	Xc (%)
A01	15/1/800	5.4	1080	89.0k	75.7
A02	15/3/800	5.6	1120	71.8k	72.4
A03	15/5/800	6.1	1220	38.6k	71.8
A04	15/8/800	6.3	1260	13.3k	66.6
A05	15/10/800	6.4	1280	35.7k	64.8
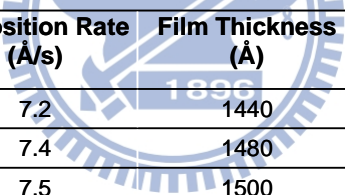
Table 6 The deposition parameters and results of sample A01~A05. (n-type Si film under deposition temperature is 200℃, deposition plasma power is 300W, deposition pressure is 4Torr, and deposition time is 200sec).

Sample ID	$SiH_4/PH_3/H_2$ (sccm)	I_{on} (A)	1/R	n-layer D.R. (Å/s)	n-layer S.R. (kΩ/□)
A02	15/3/800	3.45E-06	4.21E-06	5.56	71.75
A03	15/5/800	3.17E-05	3.89E-05	6.73	38.61
A04	15/8/800	6.05E-05	8.08E-05	6.33	13.30

Table 7 The deposition parameters and results of sample A02~A04. (n-type Si film under deposition temperature is 200℃, deposition plasma power is 300W, deposition pressure is 4Torr, and deposition time is 15 sec).

Sample ID	SiH$_4$/PH$_3$/H$_2$ (sccm)	Deposition Rate (Å/s)	Film Thickness (Å)	Sheet Resistance (Ω/□)	Xc (%)
B01	15/8/300	5.9	1180	40.6k	50.1
B02	15/8/500	5.8	1160	28.3k	52.3
B03	15/8/800	5.6	1120	13.0k	68.7
B04	15/8/1000	5.7	1140	20.6k	72.4
B05	15/8/1200	5.0	1000	25.9k	79.1
B06	15/8/1500	4.8	960	34.5k	80.9
B07	15/8/1800	4.7	940	40.2k	82.5
B08	15/8/2000	4.5	900	45.4k	85.0

Table 8 The deposition parameters and results of sample B01~B08. (n-type Si film under deposition temperature is 200℃, deposition plasma power is 300W, deposition pressure is 4Torr, and deposition time is 200 sec).

Sample ID	SiH$_4$/ B$_2$H$_6$ /H$_2$ (sccm)	Deposition Rate (Å/s)	Film Thickness (Å)	Sheet Resistance (Ω/□)	Xc (%)
C01	15/1/1200	7.2	1440	100.6k	65
C02	15/3/1200	7.4	1480	20.2k	54.6
C03	15/5/1200	7.5	1500	300.2k	<50
C04	15/8/1200	7.7	1540	1.0G	Amorphous
C05	15/10/1200	7.8	1560	1.0G	Amorphous

Table 9 The deposition parameters and results of sample C01~C05. (p-type Si film under deposition temperature is 200℃, deposition plasma power is 330W, deposition pressure is 4Torr, and deposition time is 200 sec).

Sample ID	SiH$_4$/B$_2$H$_6$/H$_2$ (sccm)	Deposition Rate (Å/s)	Film Thickness (Å)	Sheet Resistance (Ω/□)	Xc (%)
D01	15/5/300	9.3	1860	200.5k	Amorphous
D02	15/5/500	9.2	1840	150.2k	Amorphous
D03	15/5/800	9.0	1800	81.2k	<50
D04	15/5/1000	8.9	1780	79.4k	<50
D05	15/5/1200	8.8	1760	73.3k	<50
D06	15/5/1600	8.0	1600	9.7k	66.1
D07	15/5/2000	6.8	1360	11.1k	73.2

Table10 The deposition parameters and results of sample D01~D07. (p-type Si film under deposition temperature is 200℃ , deposition plasma power is 330 W, deposition pressure is 4 Torr, and deposition time is 200 sec).

Sample	SiH$_4$/PH$_3$, B$_2$H$_6$/H$_2$	Deposition rate (Å/s)	Sheet resistance (kΩ/□)	Xc (%)
n-uc-Si	15/8/800	5.6	**13.0**	~69
p-uc-Si	15/5/1600	8.0	**9.7**	~66

Table 11 Optimization of Si thin-film for HIT solar cell (p-type / n-type Si films).

The deposition parameters and results were shown here.

i-layer thickness (nm)	Jsc (mA/ cm^2)	Eff (%)	FF	Voc (V)
1	21.659	13.909	0.851	0.75
3	21.654	14.028	0.851	0.761
5	21.651	14.046	0.849	0.76
9	21.647	13.965	0.843	0.76
20	21.634	12.166	0.745	0.75

Table 12 The AMPS-1D simulation results by adjusting i-a-Si (i-layer) films of

HIT solar cells.

Doping concentration (cm^{-3})	Jsc (mA/ cm^2)	Eff (%)	FF	Voc (V)
1E+15	21.615	10.855	0.787	0.638
5E+16	21.614	10.860	0.787	0.639
1E+17	21.614	10.865	0.787	0.639
1E+18	21.613	10.953	0.791	0.641
1E+19	21.599	11.561	0.814	0.657
1E+20	21.468	12.584	0.838	0.699
1E+21	21.337	13.141	0.846	0.728

Table 13 The AMPS-1D simulation results by adjusting n-a-Si (n-layer) doping

concentrations of HIT solar cells.

DNG (cm^{-3})	Jsc (mA/cm^2)	Eff (%)	FF	Voc (V)
1E+15	21.613	11.587	0.807	0.664
4E+15	21.612	11.556	0.806	0.663
4E+16	21.607	11.276	0.804	0.649
4E+17	21.558	10.296	0.801	0.596
4E+18	21.178	8.469	0.774	0.516
4e+19	20.025	3.426	0.458	0.374

Table 14 The AMPS-1D simulation results by adjusting defect densities of n-a-Si / i-a-Si films in HIT solar cells.

Sample ID	Parameter	Ion (A)	Ioff (A)	1/R	Von (V)
E01	Without H$_2$ treatment	3.27E-05	-8.29E-09	4.20E-05	0.227
E02	H$_2$ Treatment：H$_2$=600 sccm	3.58E-06	-5.20E-09	6.32E-06	0.440
E03	H$_2$ Treatment：H$_2$=1200 sccm	1.73E-05	-8.03E-09	2.46E-05	0.309

Table 15 The HIT solar cell deposition parameters and results of sample E01~E03 under various H$_2$ flow of post H$_2$ plasma treatment. Sample E01 is baseline without post H$_2$ plasma treatment. Sample E02 is treated by H$_2$ flux 600sccm, and Sample E03 is treated by H$_2$ flux 1200sccm. (The Si film deposition temperature is 200℃, deposition plasma power is 300W, and deposition pressure is 4Torr).

Sample ID	Parameter	Ion (A)	Ioff (A)	1/R	Von (V)
F01	Without H_2 treatment	3.31E-05	-1.57E-07	3.78E-05	0.204
F02	H_2 Treatment @ 200 W	4.83E-06	-3.27E-09	9.59E-06	0.477
F03	H_2 Treatment @ 150 W	5.64E-06	-3.09E-10	1.01E-05	0.487
F04	H_2 Treatment @ 100 W	9.12E-07	-7.49E-10	1.75E-06	0.514

Table 16 The HIT solar cell deposition parameters and results of sample F01~F04 under various H_2 plasma power of post H_2 plasma treatment. Sample F01 is baseline without post H_2 plasma treatment. Sample F02, F03, and F04 are under post H_2 plasma power 200W, 150W, and 100W, individually. (The Si film deposition temperature is 200℃, deposition plasma power is 300W, and deposition pressure is 4Torr).
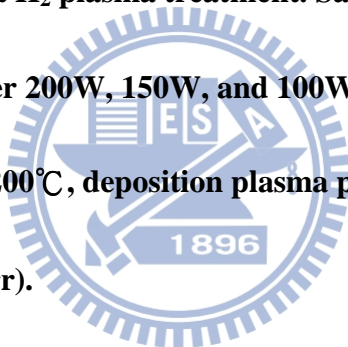
Sample ID	Parameter	Ion (A)	Ioff (A)	1/R	Von (V)
G01	H_2 Treatment @ 2.25 torr	2.44E-06	-6.88E-10	5.34E-06	0.492
G02	H_2 Treatment @ 1.5 torr	4.56E-06	-5.06E-10	8.48E-06	0.430
G03	H_2 Treatment @ 0.75 torr	8.48E-06	-5.59E-10	1.87E-05	0.547

Table 17 The HIT solar cell deposition parameters and results of sample G01~G03 under various H_2 plasma pressure of post H_2 plasma treatment. Sample G01, G02, and G03 are under post H_2 plasma pressure 2.25 Torr, 1.5 Torr, and 0.75 Torr, individually. (The Si film deposition temperature is 200℃, deposition plasma power is 300W, and deposition pressure is 4Torr. The post H_2 plasma treatment power is 100 W.)
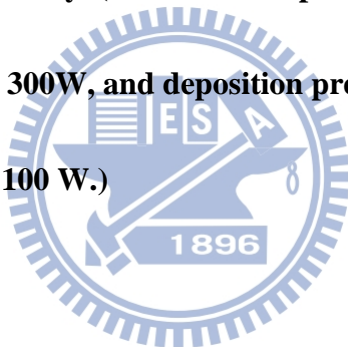
Sample ID	Parameter	Ion (A)	Ioff (A)	1/R	Von (V)
H01	Baseline (without H_2 treatment)	1.83E-05	-5.99E-09	2.93E-05	0.376
H02	H_2 Treatment @ 10 sec	2.34E-05	-1.66E-07	3.56E-05	0.357
H03	H_2 Treatment @ 30 sec	1.28E-05	-5.25E-09	2.58E-05	0.559
H04	H_2 Treatment @ 50 sec	1.86E-05	-6.13E-09	4.65E-05	0.594

Table 18 The HIT solar cell deposition parameters and results of sample H01~H04 under various post H_2 plasma treatment time. Sample H01 is baseline without post H_2 plasma treatment. Sample H02, H03, and H04 are under post H_2 plasma time 10 sec, 30 sec, and 50 sec, individually. (The Si film deposition temperature is 200℃, deposition plasma power is 300W, and deposition pressure is 4Torr.)
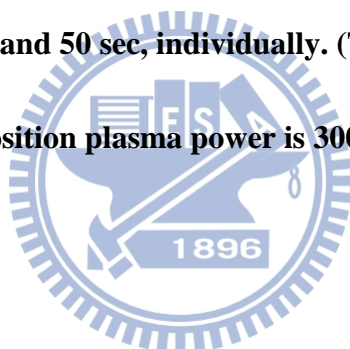
Sample ID	Parameter	Voc (V)	Jsc (mA/ cm^2)	F.F.	Eff (%)
I01	No H_2 Treatment	0.42	22.82	25.3	2.42
I02	H_2 Treatment	0.41	22.67	39.5	3.67

Table 19 The results of HIT solar cells. Sample I01 is deposited by VHF-PECVD without post H_2 plasma treatment, and sample I02 is deposited with post H_2 plasma treatment.

Sample ID	Parameter	Voc (V)	Jsc (mA/ cm^2)	F.F.	Eff (%)
J01	No H2 Treatment	0.75	13.92	49.5	5.17
J02	H2 Treatment	0.90	14.68	61.0	8.05

Table 20 The results of HIT solar cells. Sample J01 is deposited by VHF-PECVD without post H$_2$ plasma treatment, and sample J02 is deposited with post H$_2$ plasma treatment.

Sample No.	Parameter	V_{oc} (V)	J_{sc} (mA/cm^2)	F.F.	E_{ff} (%)
J02	15/30/100/30 sec	0.90	14.68	61.0	8.05
J03	20/30/100/30 sec	0.74	13.62	57.0	5.74

Table 21 The results of HIT solar cells. Sample J02 is deposited by VHF-PECVD with 15sec i-a-Si (i-layer) film deposition time, and sample J03 is deposited with 20 sec i-a-Si (i-layer) film deposition time.

Sample No.	Parameter	V_{oc} (V)	J_{sc} (mA/cm^2)	F.F.	E_{ff} (%)
K01	10/30/100/30 sec	0.90	14.11	70.8	8.99
K02	10/10/100/30 sec	0.91	14.32	73.3	9.56

Table 22 The results of HIT solar cells. Sample K01 is deposited by VHF-PECVD with 30 sec n-a-Si (n-layer) film deposition time, and sample K02 is deposited with 10 sec n-a-Si (n-layer) film deposition time.

Sample No.	Parameter	V_{oc} (V)	J_{sc} (mA)	F.F.	E_{ff} (%)
K02	H_2 Treatment	0.91	14.32	73.3	9.56
K03	No H_2 Treatment	0.90	13.82	71.0	8.78

Table 23 The results of HIT solar cells. Sample K03 is baseline without post H_2 plasma treatment. Sample K02 is deposited by VHF-PECVD with post H_2 plasma treatment.

Sample No.	Parameter	AM 1.5 J_{sc} (mA/cm^2)
K02	H_2 Treatment	22.23
K03	No H_2 Treatment	21.27

Table 24(A) The E.Q.E. measurement results (AM 1.5 Jsc) of HIT solar cells. Sample K03 is baseline without post H_2 plasma treatment. Sample K02 is deposited by VHF-PECVD with post H_2 plasma treatment.

Sample No.	Wavelength (nm)	400~500	500~700	700~900	900~1100
K02	H_2 Treatment	14.6	57.8	74.1	38.7
K03	No H_2 Treatment	28.3	55.1	61.9	40.8

Table 24(B) The E.Q.E. measurement results (wavelength range from 400 nm to 1100 nm) of HIT solar cells. Sample K03 is baseline without post H_2 plasma treatment. Sample K02 is deposited by VHF-PECVD with post H_2 plasma treatment.

Sample No.	RTA temp. (℃)	Voc (V)	Jsc (mA/ cm^2)	F.F.	Eff (%)
L01	No RTA	0.90	13.82	70.6	8.78
L02	150	0.91	13.88	71.5	9.03
L03	180	0.90	14.11	71.9	9.13
L04	200	0.90	15.34	69.4	9.59
L05	250	0.88	14.32	70.5	8.88

Table 25 The results of the double-side HIT solar cells. Sample L01 is baseline without RTA treatment. Sample L02, L03, L04, and L05 were treated under various RTA temperatures.

Sample No.	RTA temp. (℃)	Voc (V)	Jsc (mA/cm2)	F.F.	Eff (%)
M01	No RTA	0.90	14.96	74.3	10.00
M02	150	0.90	15.27	73.8	10.13
M03	200	0.91	17.36	70.1	11.07
M04	250	0.91	15.09	74.5	10.23

Table 26 The results of the double-side HIT solar cells with post H$_2$ plasma treatment. Sample M01 is baseline without RTA treatment. Sample M02, M03, and M04 were treated under various RTA temperatures.

	Voc (V)	Jsc (mA/cm2)	F.F.	Eff (%)
No H_2 treatment	0.75	13.92	49.5	5.17
H_2 treatment	0.90	14.68	61.0	8.05
H_2 treatment, thinner i/n-layer	0.91	14.32	73.3	9.56
H_2 treatment, thinner i/n-layer, RTA	0.91	17.36	70.1	11.07

Table 27 The summary of HIT solar cell with or without post H_2 plasma treatment and RTA treatment.

Figure List
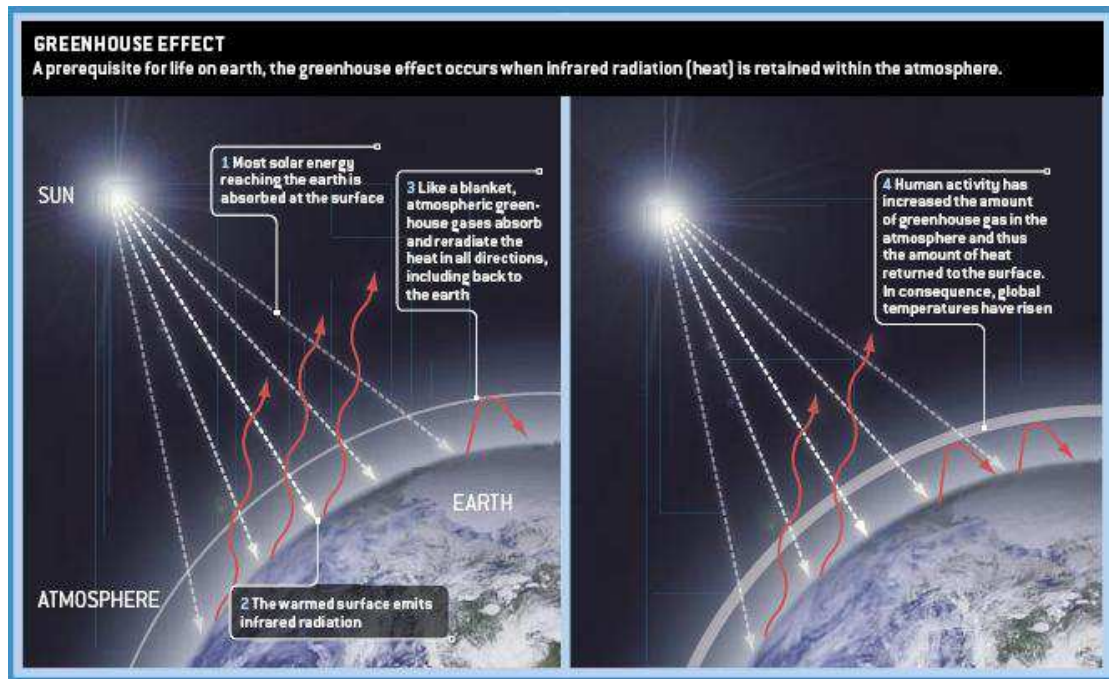
Fig. 1 The figure shows how the greenhouse effect on earth.

（**Data source**：www.acoolerclimate.com/the-greenhouse-effects-impact/）

(a)   (b)

Fig. 2 (a) The figure shows all kinds of renewable energy, including solar, wind,

biomass, hydro, and waste. (b) The solar cell application：The solar planets are

on the roof. (Data source: http://www.solarpowerwindenergy.org)
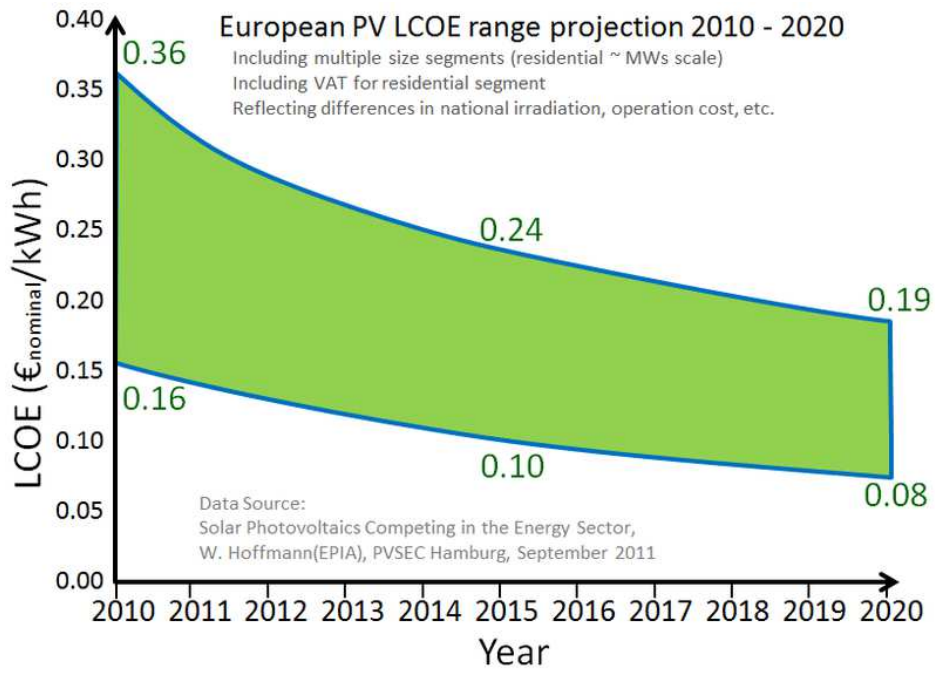
Fig. 3 European PV LCOE range projection 2010~2020

(Data source: Solar Photovoltaics Competing in the Energy Sector, W. Hoffmann

(EPIA), PVSEC Hamburg, September 2011)
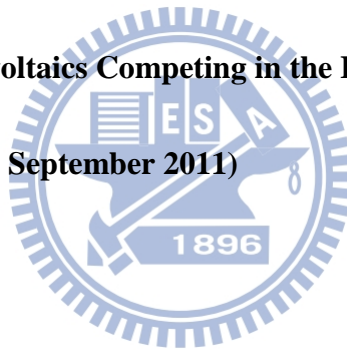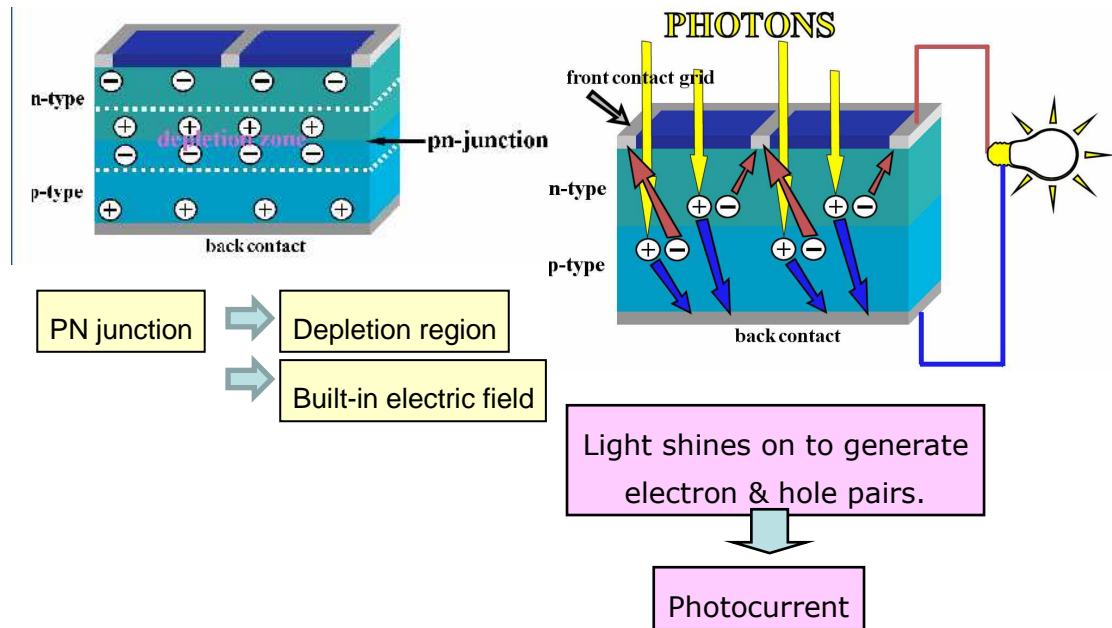
Fig. 4 The figure shows structure of the simplest solar cell (pn junction), and the process of photocurrent generation. (Data source: ELECTRONICS EVERYDAY)
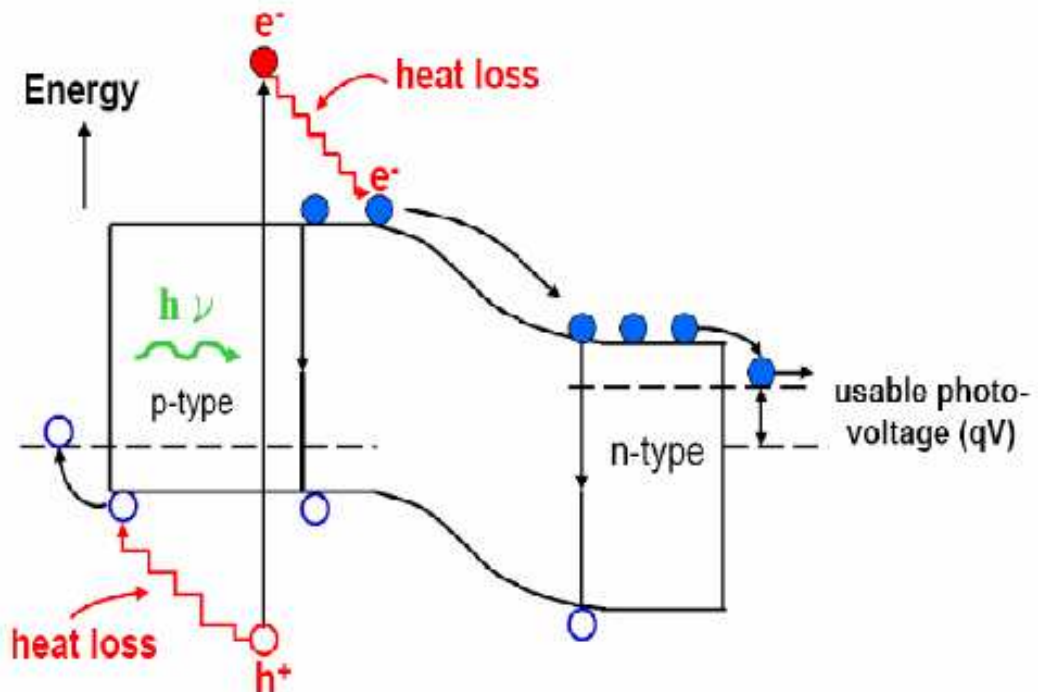
Fig. 5 The energy bandgap and physical mechanism (principles) of pn junction.

(Data source: AUO company website)
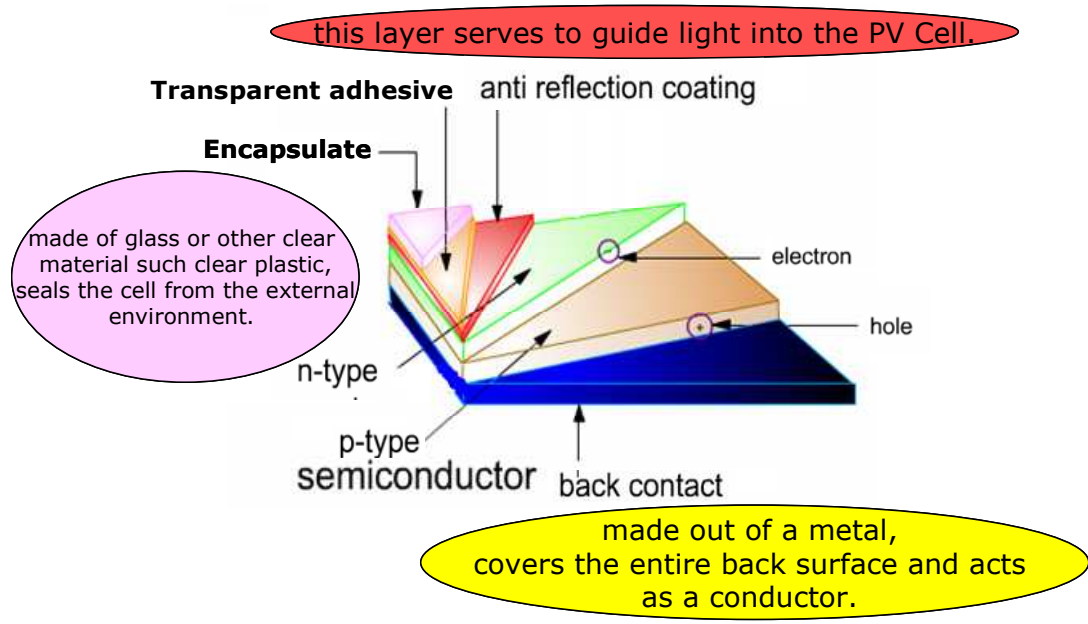
Fig. 6 The structure of conventional solar cell, including pn junction, back contact, anti reflection coating (ARC), transparent adhesive layer, and encapsulate. (Data source: ORACLE ThinkQuest, projects by students for students)
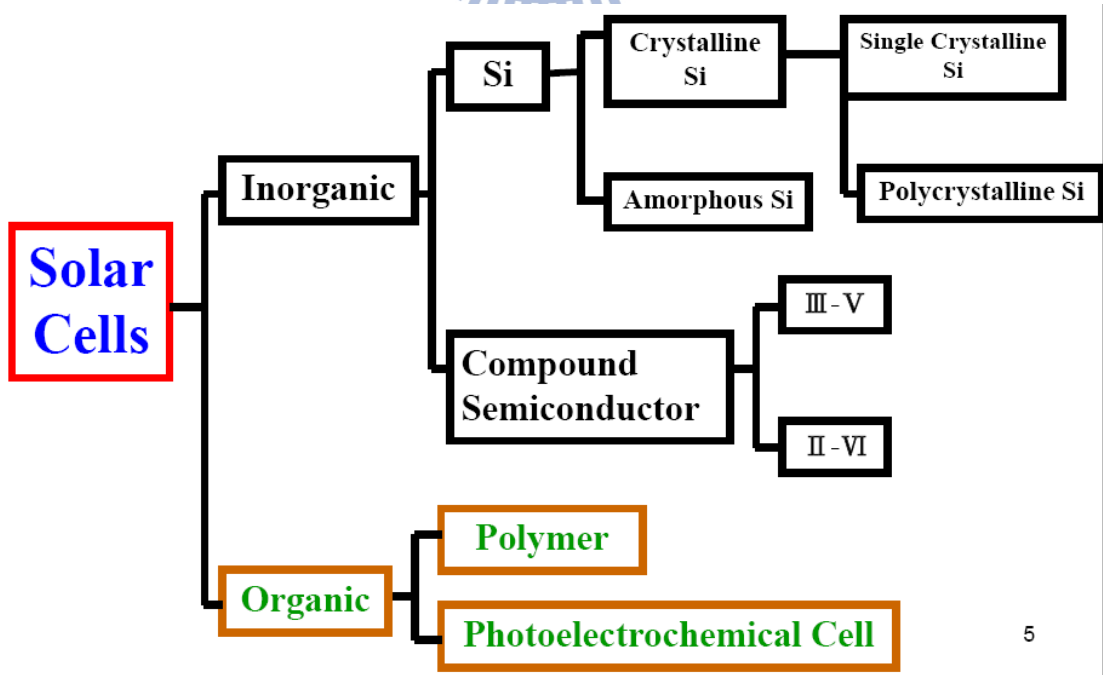
Fig. 7 The figure shows all kinds of solar cells. (Data source: SpringerImages)
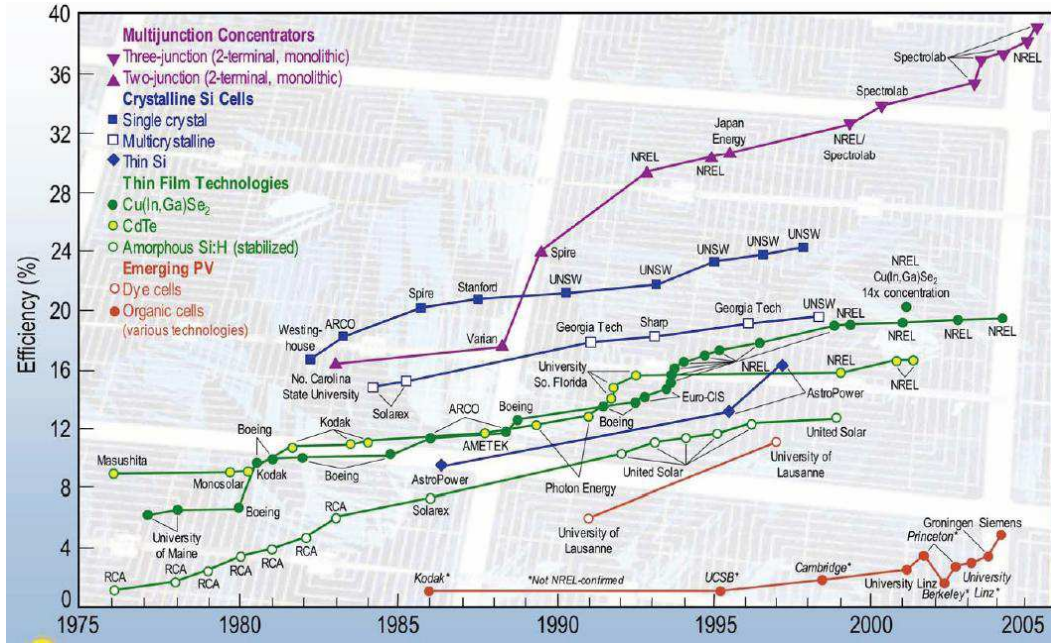
Fig. 8 The figure show some kinds of solar cells development (efficiency) during 1975~2005, and their main research institutions. (Data source: National Renewable Energy Laboratory (USA))
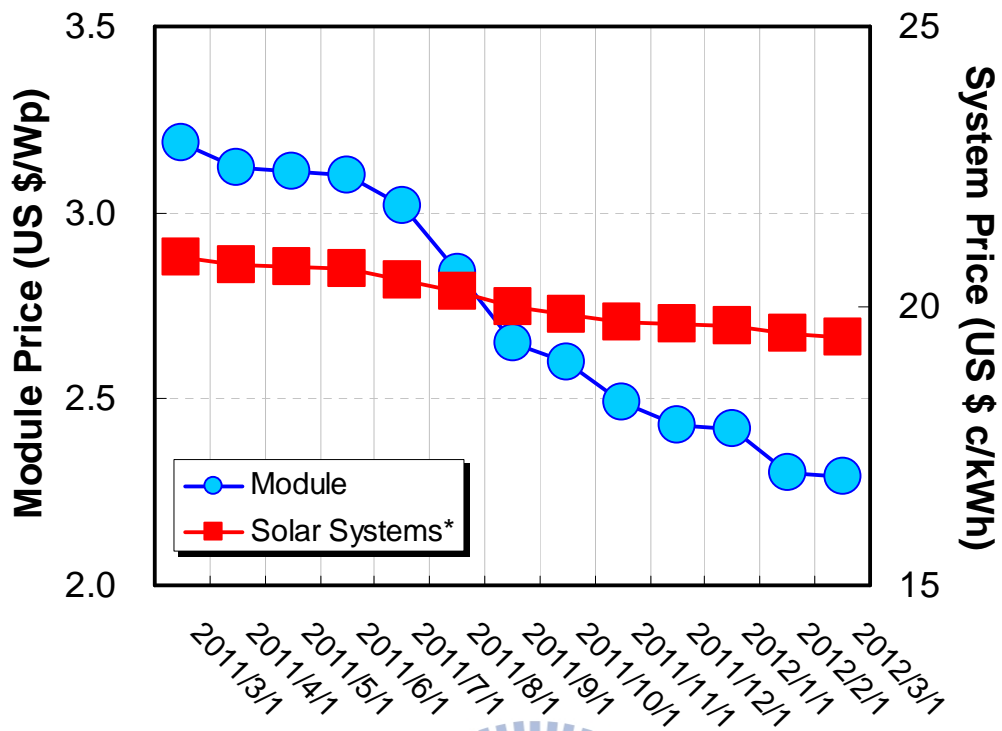
Fig. 9 The module price and system price of HIT solar cells during 2011/3/1~2012/3/1. (Data source: http://solarcellcentral.com/cost_page.html)
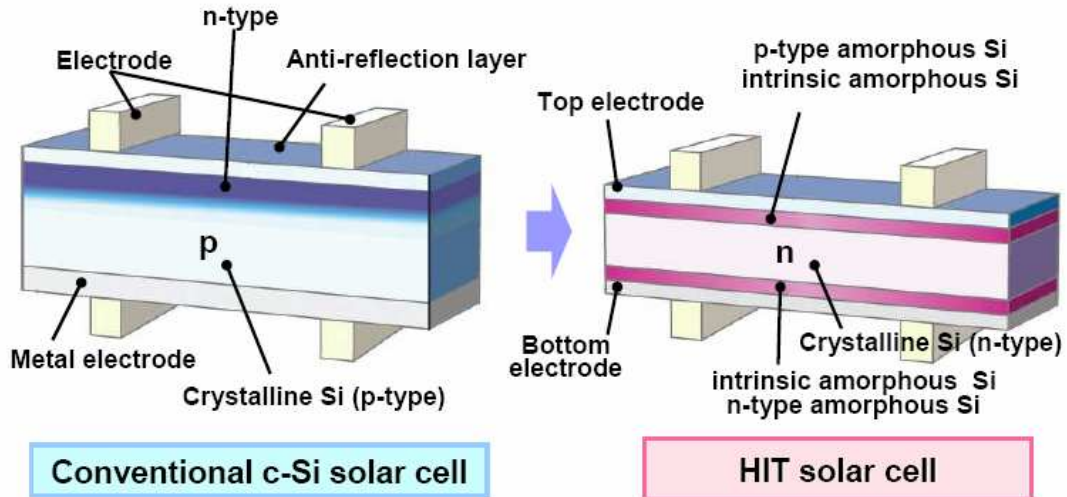
Fig. 10 The figure shows the comparison of conventional c-Si solar cell and HIT solar cell. (Data source: Copyright © SANYO Electric Co. Ltd. All Rights Reserved 2008)

Single-side HJ c-Si Solar Cell

(Al Back Surface Field)
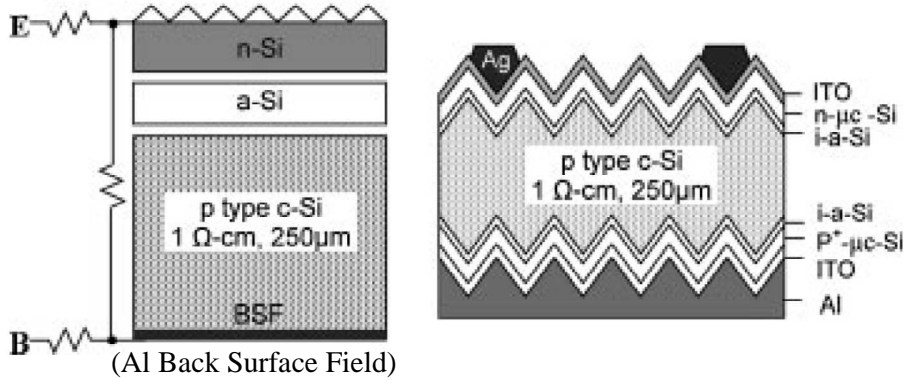
(a)

Double-side HJ c-Si Solar Cell
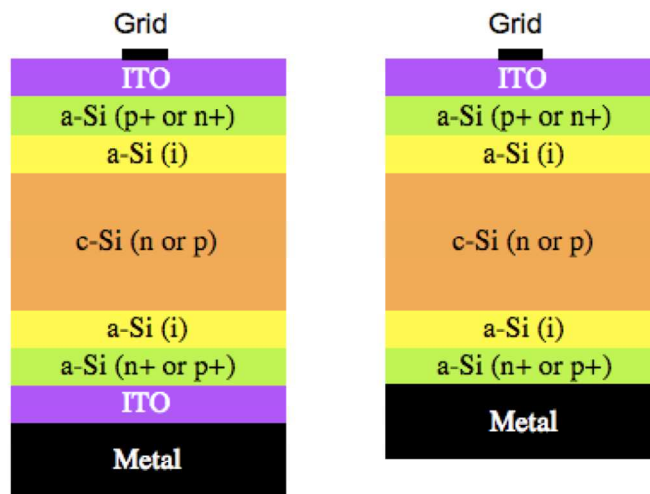
(b)

Fig. 11 (a) The structures of single side HIT solar cell. (Data source: Prog. Photovolt: Res. Appl. 2009; 17:489–501) (b) The structures of double side HIT solar cell. (Data source: *Conference Paper* **NREL/CP-520-42554 May 2008)**

(p) a-Si:H (i) a-Si:H

(n) c-Si

emitter

E_c

(i) a-Si:H (n) a-Si:H

E_f

E_v

back

n-type HIT solar cell

(a)

(i) a-Si:H (p) a-Si:H

(p) c-Si

(n) a-Si:H (i) a-Si:H

E_c
E_f

back

emitter

E_v
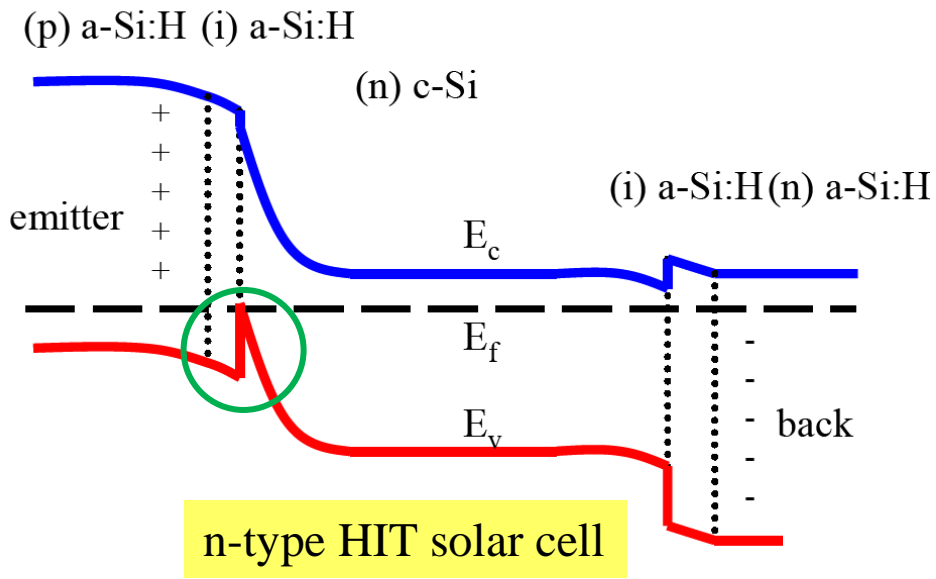
p-type HIT solar cell
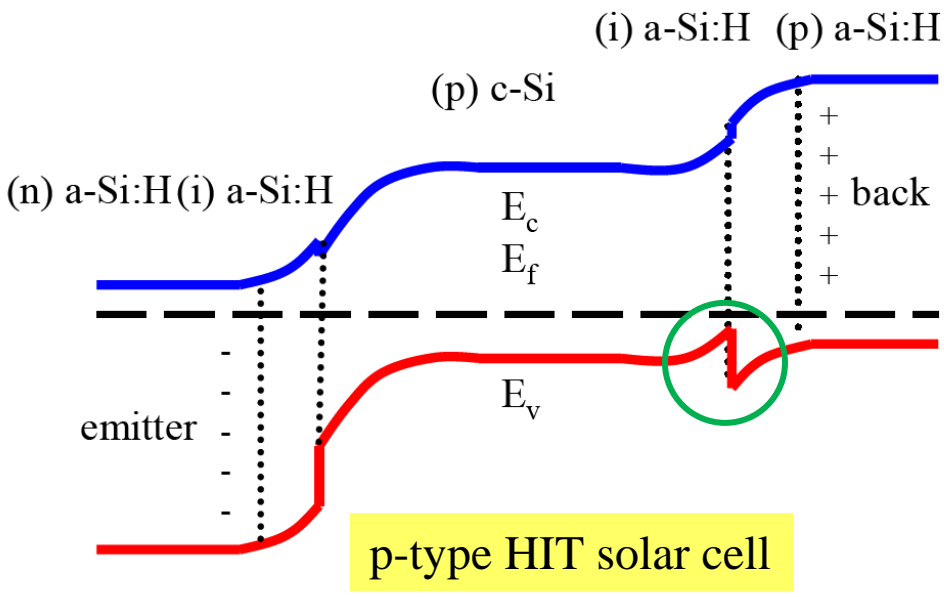
(b)

Fig. 12 (a) The energy bandgap of n-type HIT solar cell. (b) The energy bandgap of p-type HIT solar cell. (Data source: UNIVERSITAT POLITECNICA DE CATALUNYA)
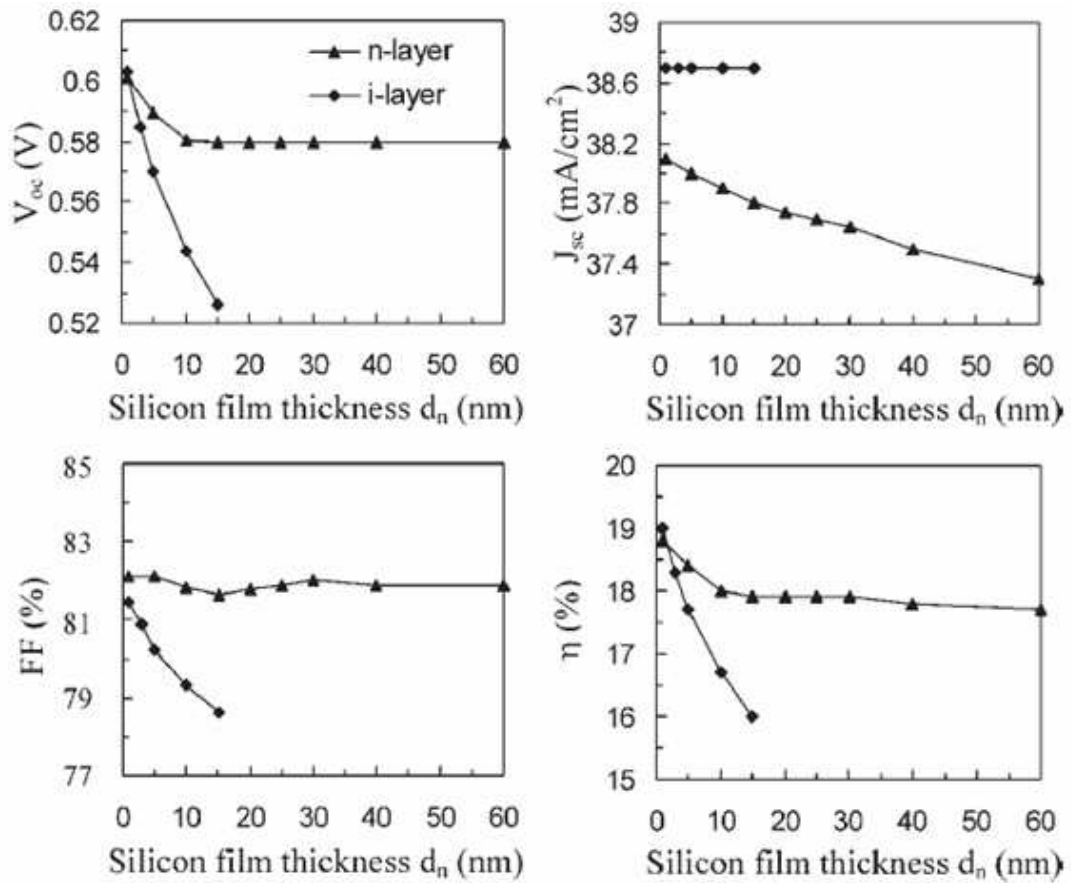
Fig. 13 Simulated dependence of the Voc, Jsc, FF and η data on the n-layer and

i-layer thicknesses for HIT solar cell samples.

(Data source: Prog. Photovolt: Res. Appl. 2009; 17:489–501)
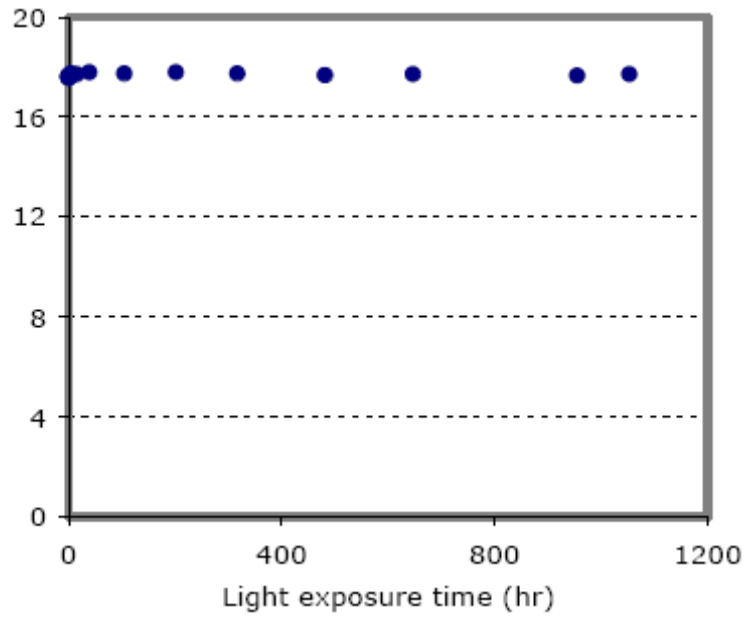
Fig. 14 Efficiency of a p-type CZ wafer HIT solar cell as a function of light exposure time. (Data source: *Conference Paper* NREL/CP-520-42554 May 2008)
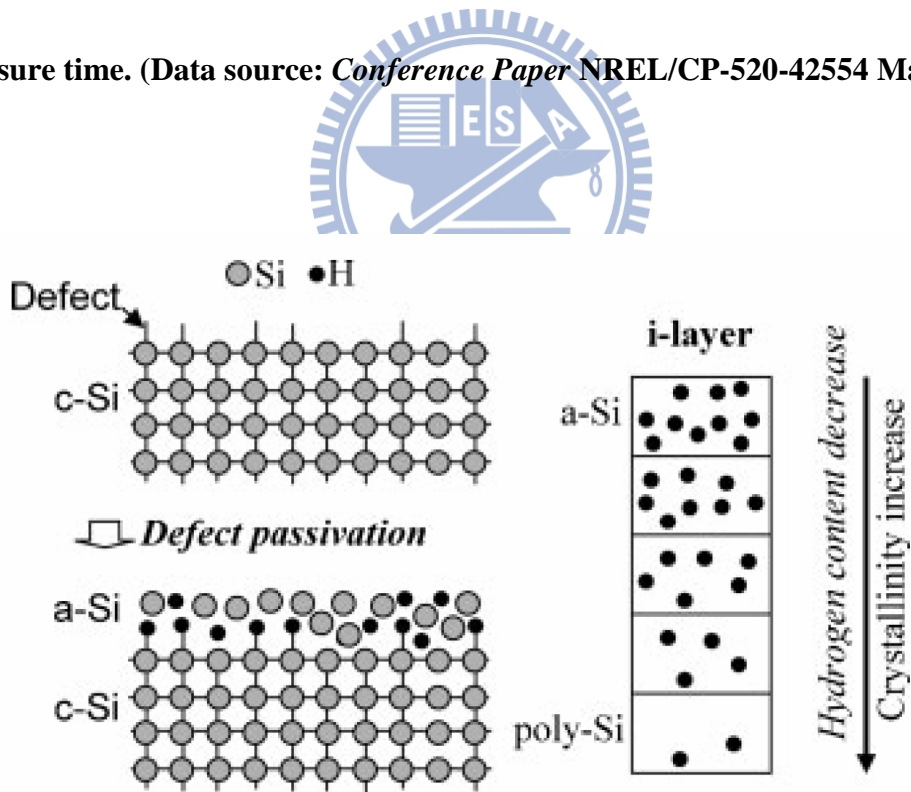
Fig. 15 Schematic representation shows the effects by hydrogen passivation.

(Data source: Prog. Photovolt: Res. Appl. 2009; 17:489–501)
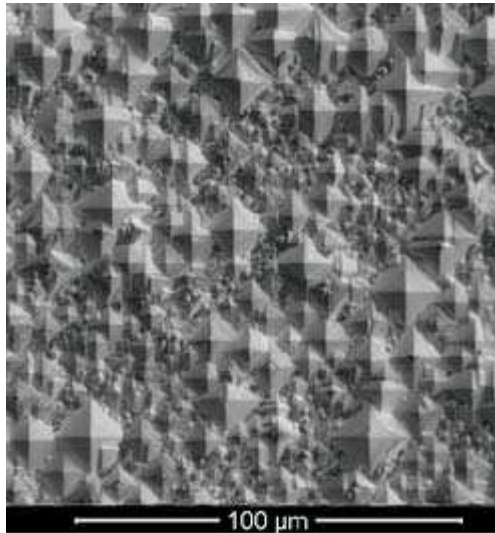
(a)
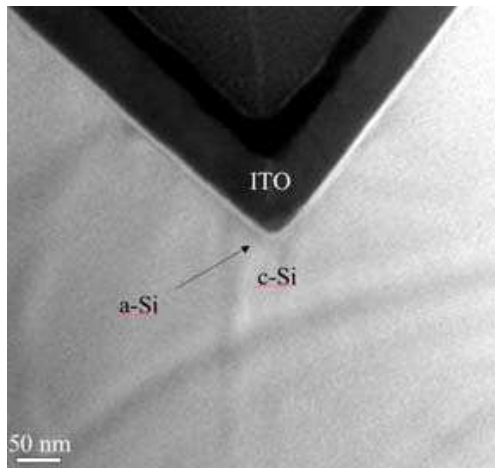
(b)

Fig.16 SEM (a) and TEM (b) picture of 19% HIT solar cell.

(Data source: Q. Wang, Conference Paper NREL/CP-520-42554, May 2008)
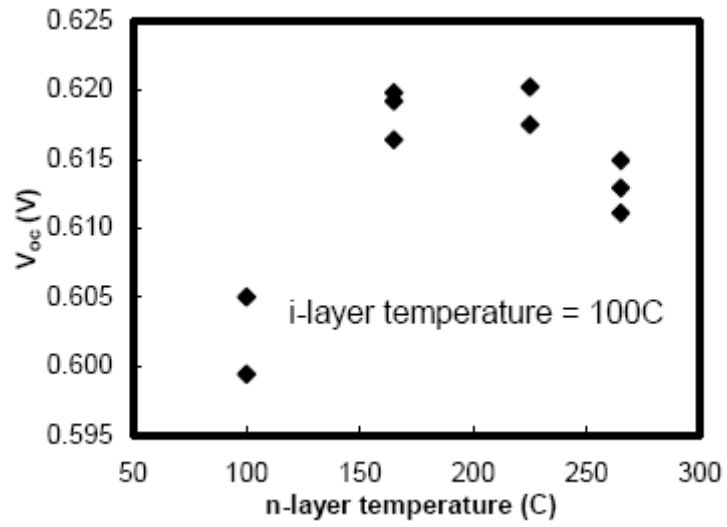
Fig. 17 The figure shows the effect of n-layer deposition temperature on Voc.

(Data source: *Conference Paper* NREL/CP-520-38942 November 2005)
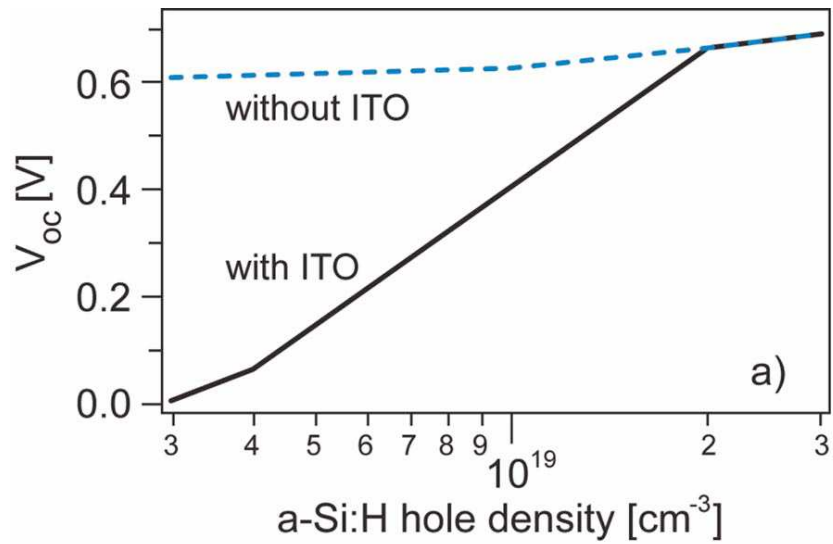
(a)
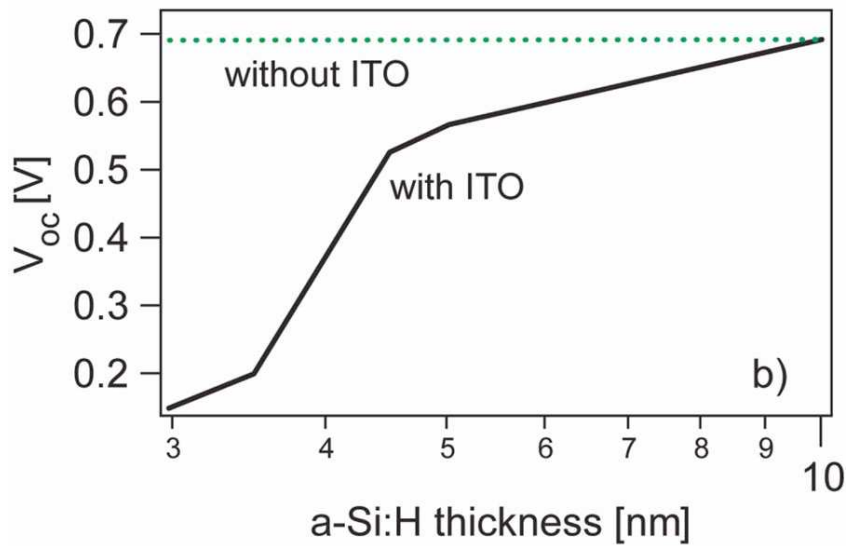
(b)

Fig. 18 (Color online) Impact of the (a) *a*-Si:H emitter doping and (b) emitter thickness on the *Voc* when ITO is included in analysis and when it is not. The entire *a*-Si:H layer is doped, and the simulations are done with an illumination of 5 mW/cm^2. The *a*-Si:H layer thickness in (a) is 10 nm, and the *a*-Si:H carrier density in (b) is 3_10^{19} cm^{-3}. (Data source: JOURNAL OF APPLIED PHYSICS 105, 094507 (2009))
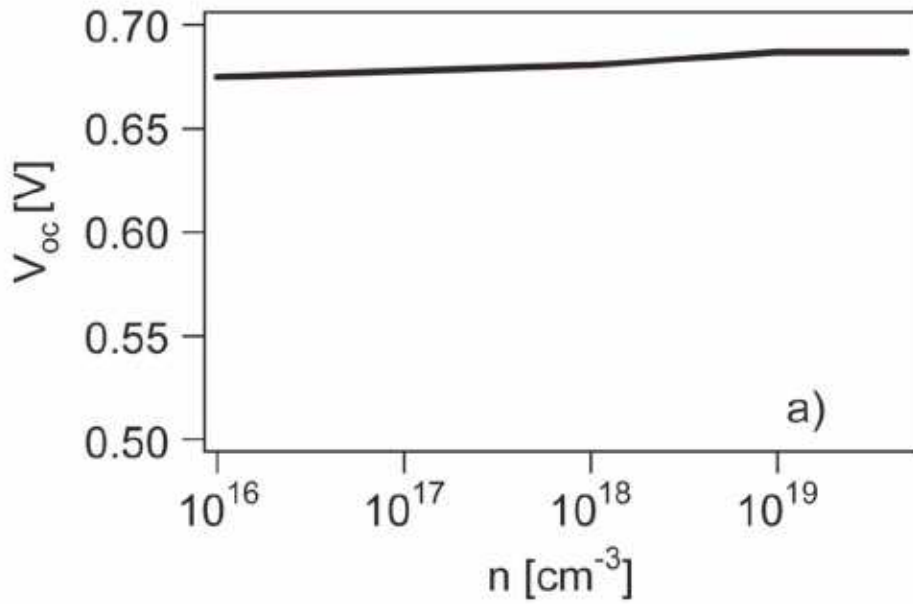
(a)
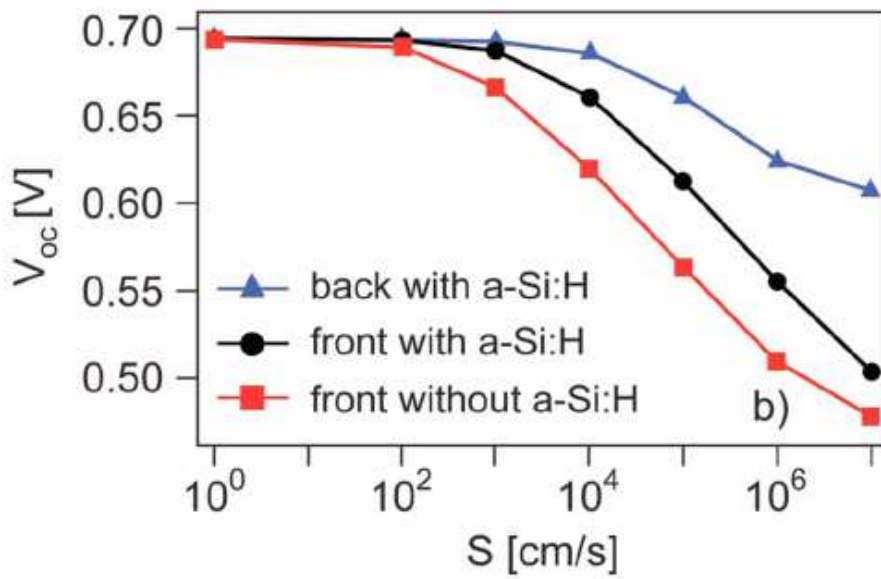
(b)

Fig. 19 (Color online) Dependence of the *Voc* for a *p*-wafer solar cell on the (a) electron density in the *n*-doped *a*-Si:H emitter and (b) surface recombination velocity at the front *c*-Si/*a*-Si:H interface (circles), back contact (triangles), and *c*-Si/ITO interface when *a*-Si:H is omitted (squares). (Data source: JOURNAL OF APPLIED PHYSICS 105, 094507 (2009))
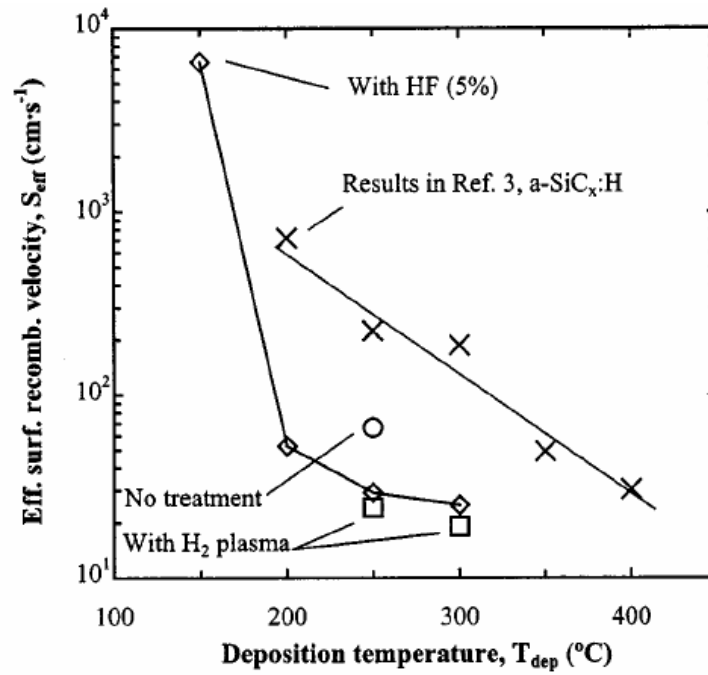
Fig. 20 S_{eff} values obtained in this study with wet cleaning (diamonds), H$_2$

plasma (squares), and no previous treatment (circle) vs deposition temperature.

(Data source: APPLIED PHYSICS LETTERS VOLUME 84, NUMBER 9 1

MARCH 2004)
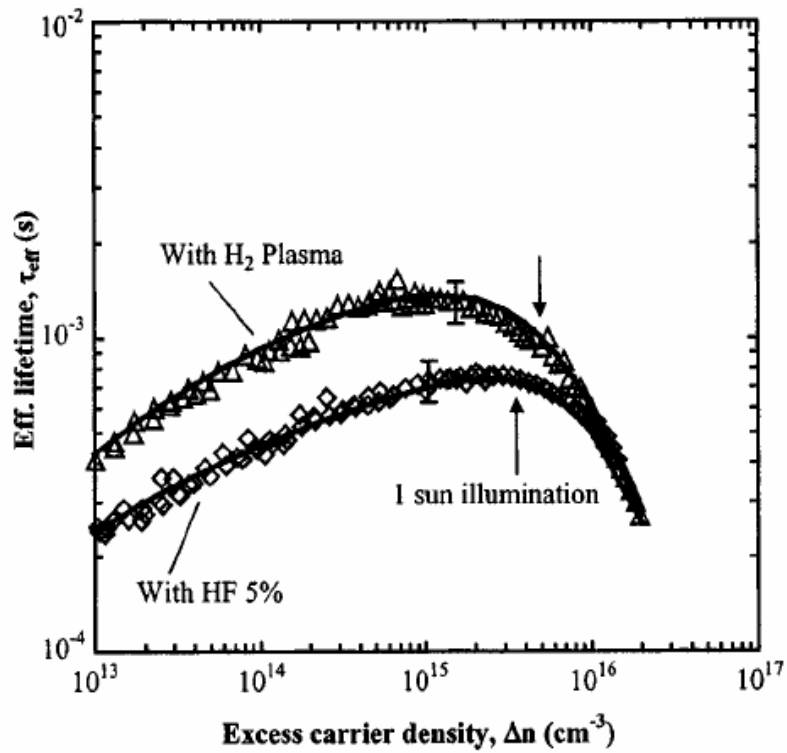
Fig. 21 Simulations (lines) and measured data (symbols) for two samples deposited at 300 °C with different cleaning procedures: H₂ plasma treatment and HF 5% dip. (Data source: Universitat Polite`cnica de Catalunya, and Laboratoire de Physique des Interfaces et des Couches Minces, Appl. Phys. Lett., Vol. 84, No. 9, 1 March 2004)

Fig. 22 The figure shows the deposition equipment- 40.68MHz VHF-PECVD.

(Data source: Industrial Technology Research Institute, ITRI)
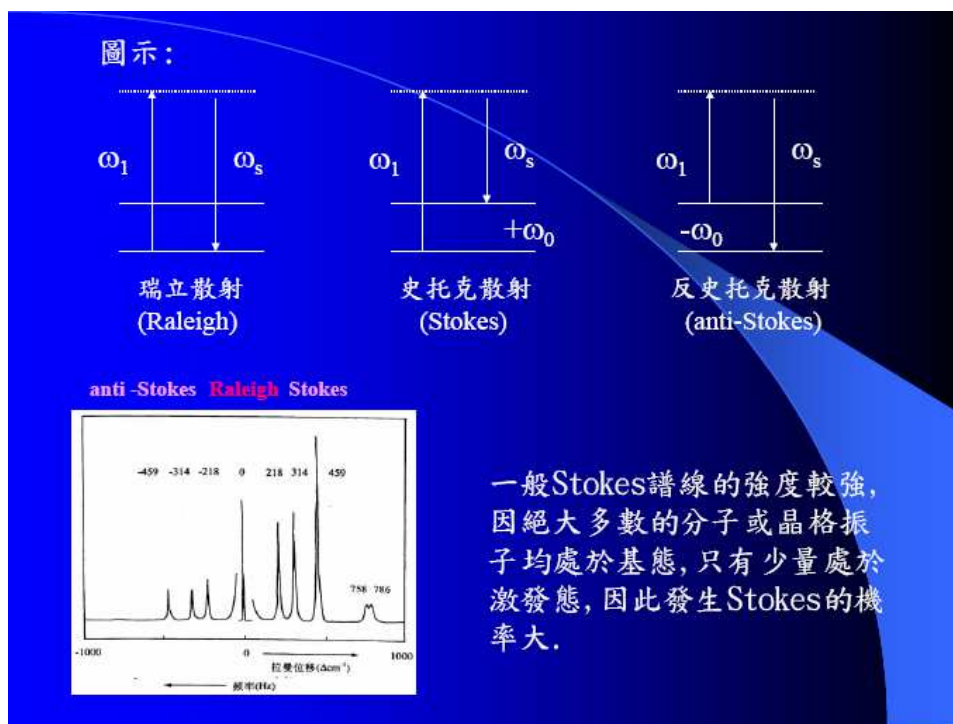
Fig. 23 The figure explains the process of Raman scattering.

(Data source: Center for Condensed Matter Sciences, 凝態科學研究中心

http://www.ntu-ccms.ntu.edu.tw/lab/homepage/ultrafast/paper/PDF/1-5-2-4.

pdf)
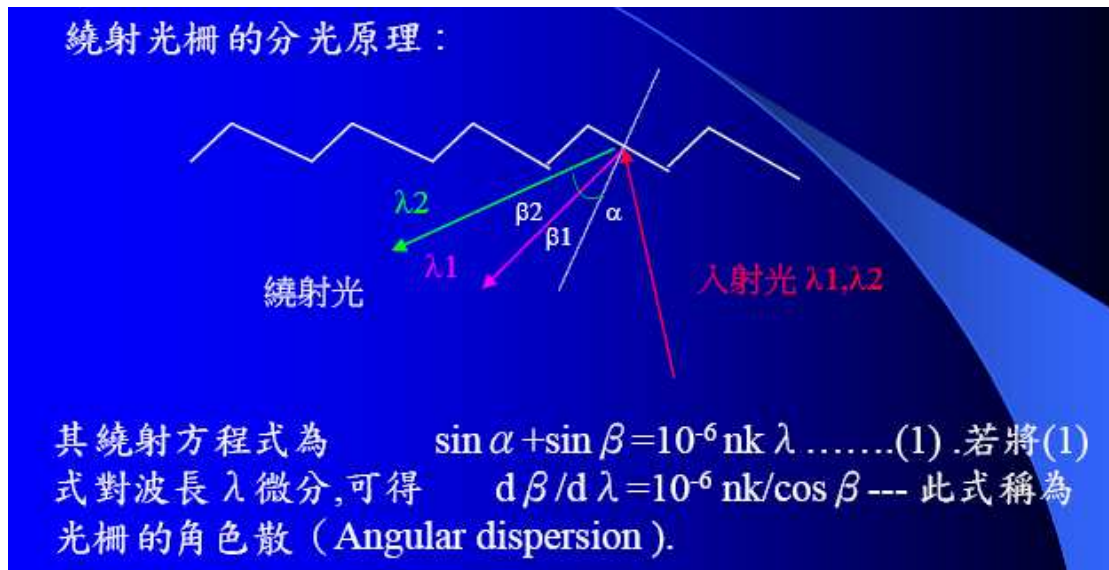
Fig. 24 The figure shows the process of angular dispersion.

(Data source: Center for Condensed Matter Sciences，凝態科學研究中心

http://www.ntu-ccms.ntu.edu.tw/lab/homepage/ultrafast/paper/PDF/1-5-2-4.pdf)
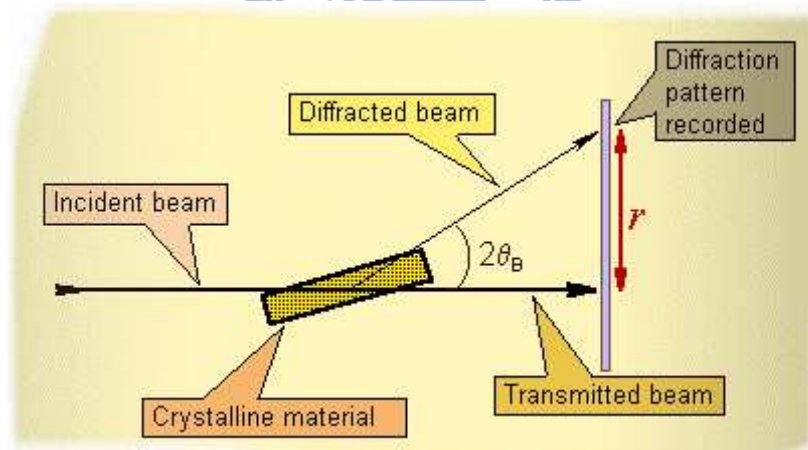
Fig. 25 The figure shows the formation of diffracted beam and diffraction pattern recorded during XRD measurement.

(Data source: www.micro.magnet.fsu.edu/primer/java/interference/index.html)
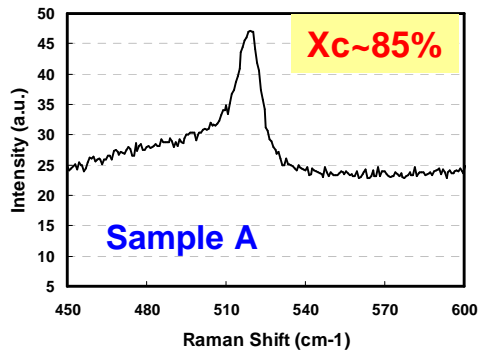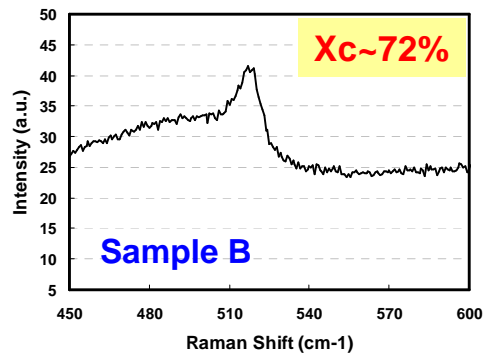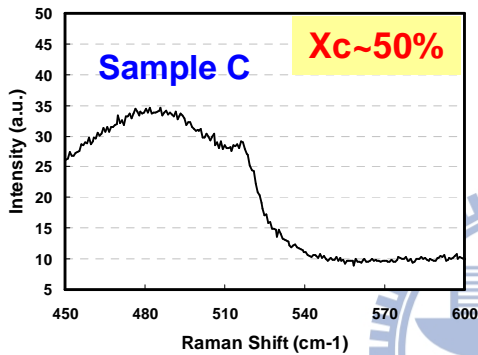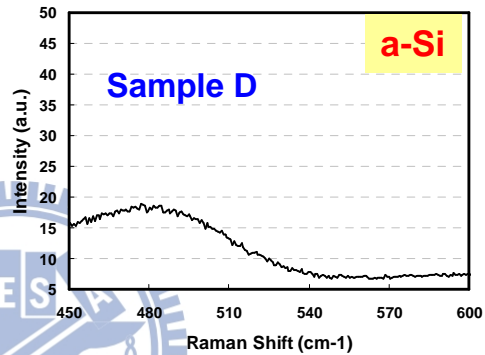
Fig. 26 The figures show Raman spectrum of Si films with various crystalline (Xc). (a) Raman spectrum of sample A (poly-Si film with Xc~85%). (b) Raman spectrum of sample B (poly-Si film with Xc~72%). (c) Raman spectrum of sample C (poly-Si film with Xc~50%). (d) Raman spectrum of sample D (a-Si film with Xc~0%).

(a)

(b)

(b)

(d)

(e)

(f)
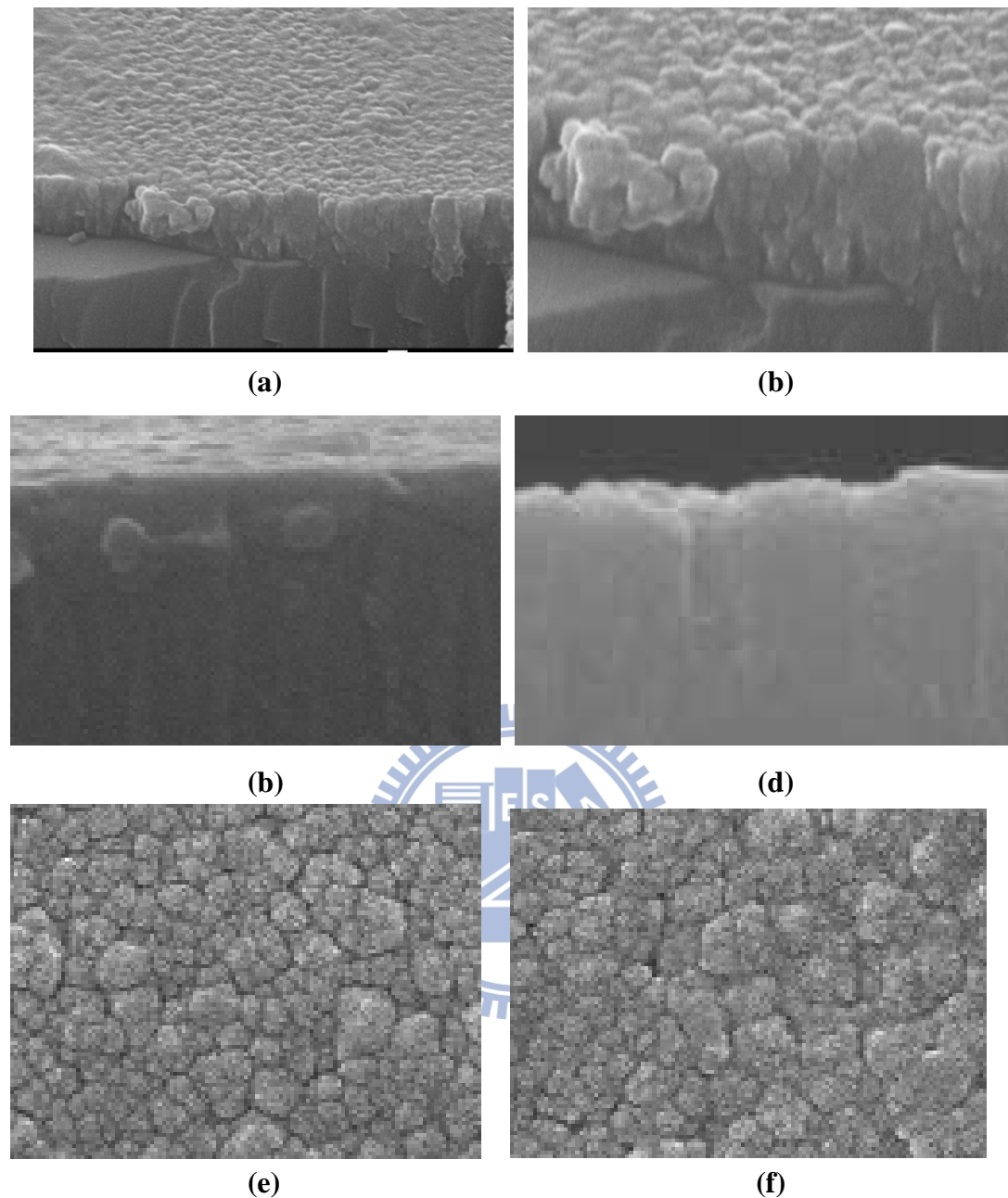
Fig. 27 The figures show the SEM images of Si films, including the plan-view and cross section. (a) The cross section SEM image of poly-Si film. (X10,000). (b) The cross section SEM image of poly-Si film. (X20,000). (c) The cross section SEM image of poly-Si film. (X50,000). (d) The cross section SEM image of poly-Si film. (X70,000). (e) The plan-view SEM image of poly-Si film. (10,000X). (f) The plan-view SEM image of poly-Si film. (10,000X).
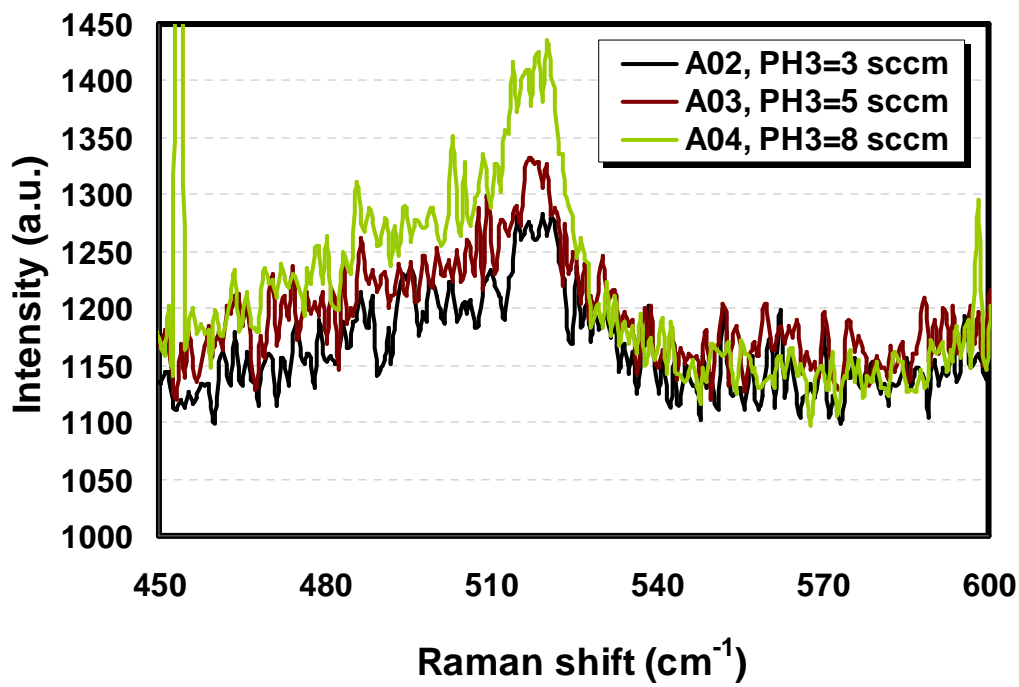
Fig. 28 The Raman spectrum of Si films when the [PH$_3$] flow rate increased from
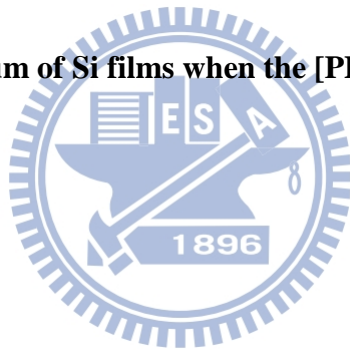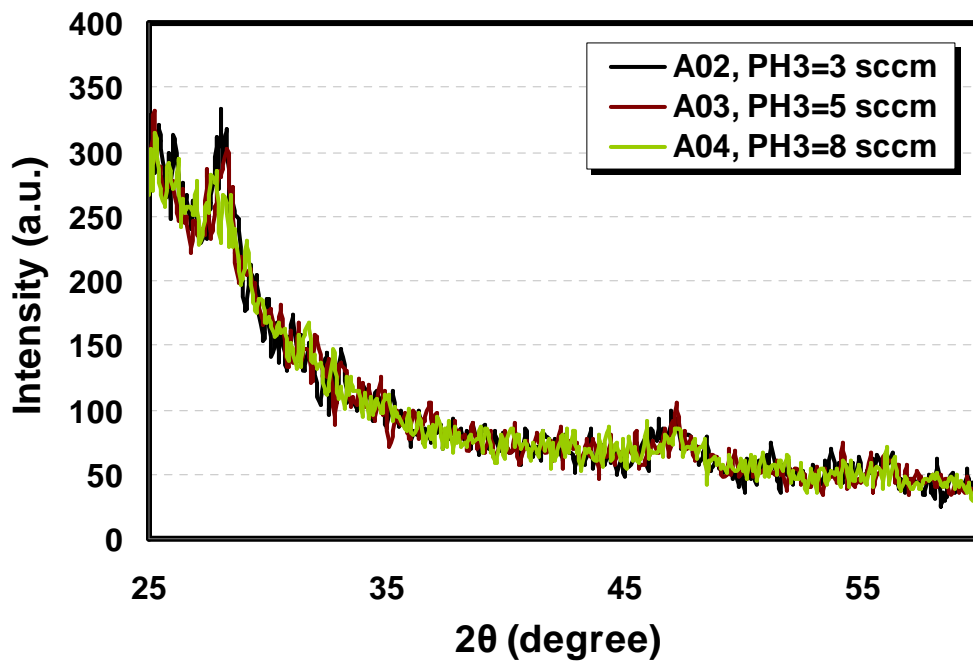
3/5/8 sccm.

Fig. 29 The XRD spectrum of Si film when the [PH$_3$] flow rate increased from
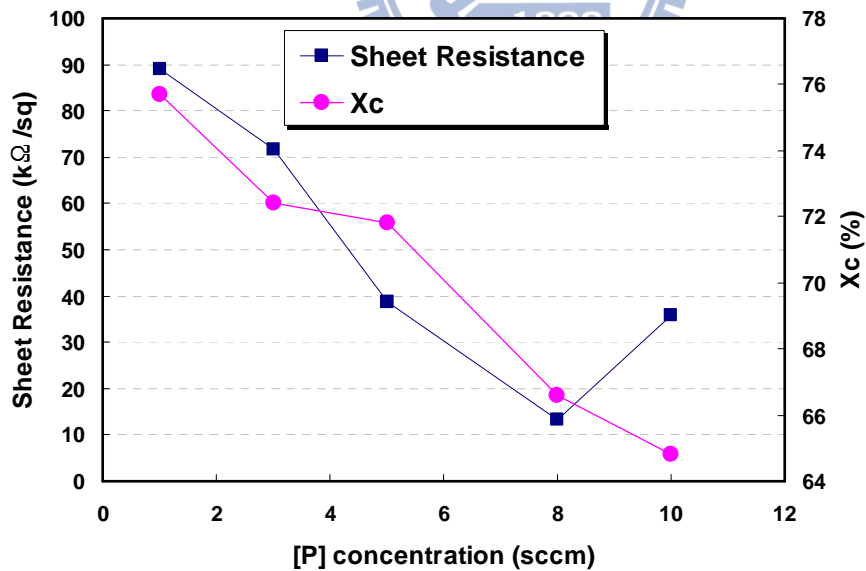
3/5/8 sccm.

Fig. 30 The sheet resistance (S.R., $\Omega/\square$) of Si films under different [P]

concentration ([PH$_3$] flow rates) and the corresponding Xc. We can see Xc

decreases when the [P] concentration increases.
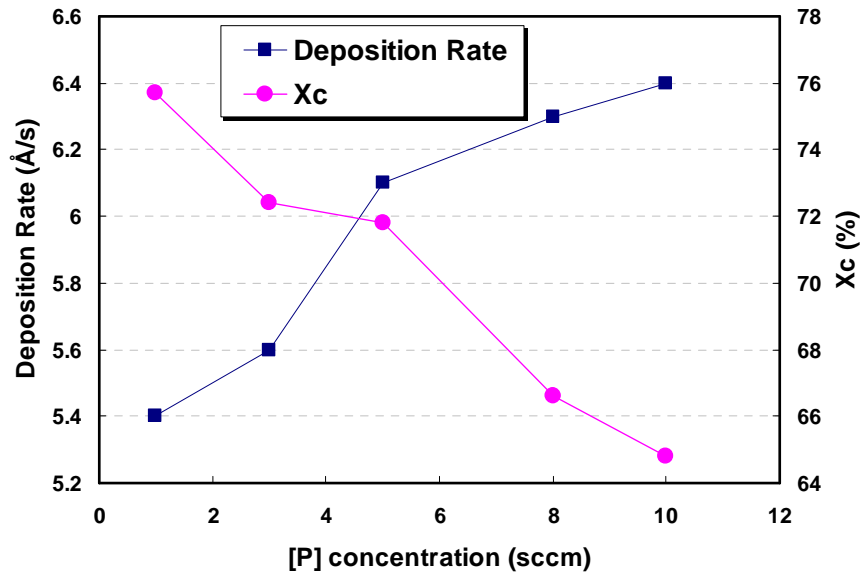
Fig. 31 The deposition rate (D.R., Å/s) of Si films under different [P] concentration ([PH₃] flow rates) and the corresponding Xc. We can see Xc decreases when the [P] concentration increases.
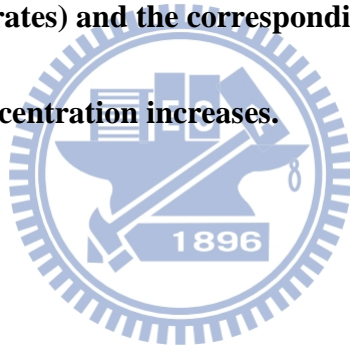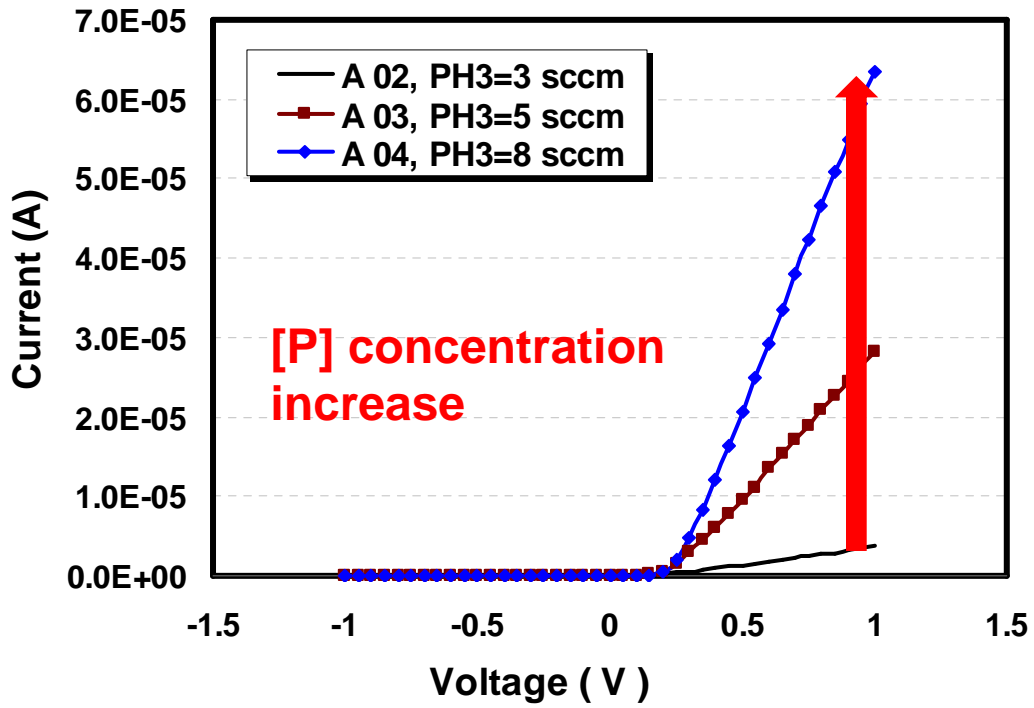
Fig. 32 The figure shows dark IV curves of sample A02, A03, and A04. We can see on-current (I_{on}) increases when the [P] concentration ($[PH_3]$ flow rates) increases from 3/5/8 sccm (A02/A03/A04).
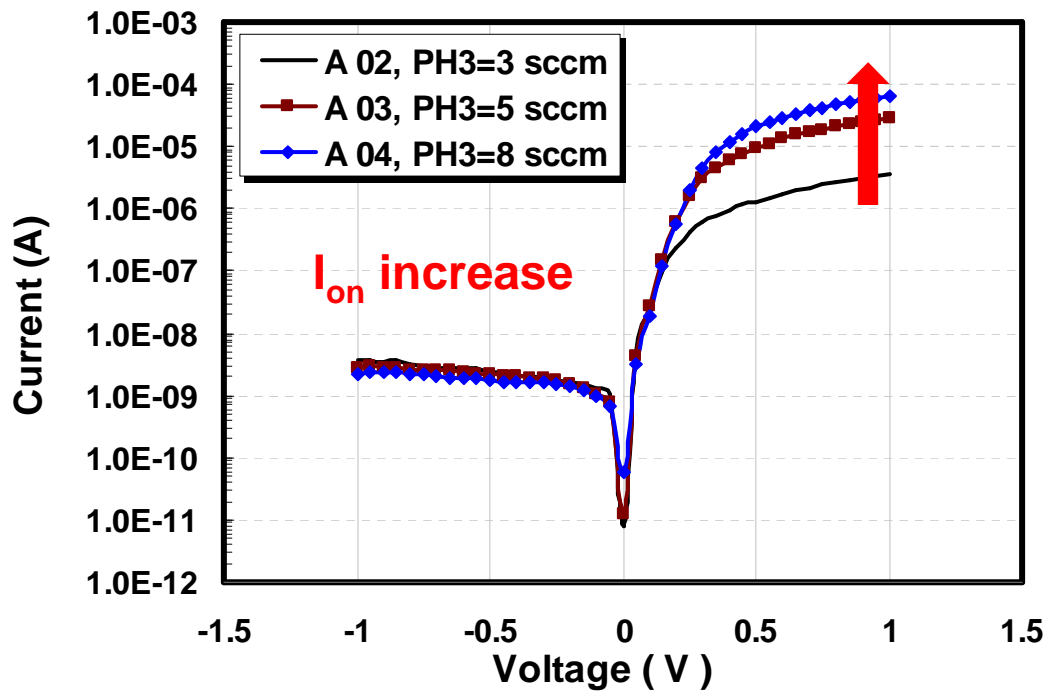
Fig. 33 The log scale of dark-IV curve show the same: I_{on} increases when the [P]

concentration ([PH_3] flow rates) increases.
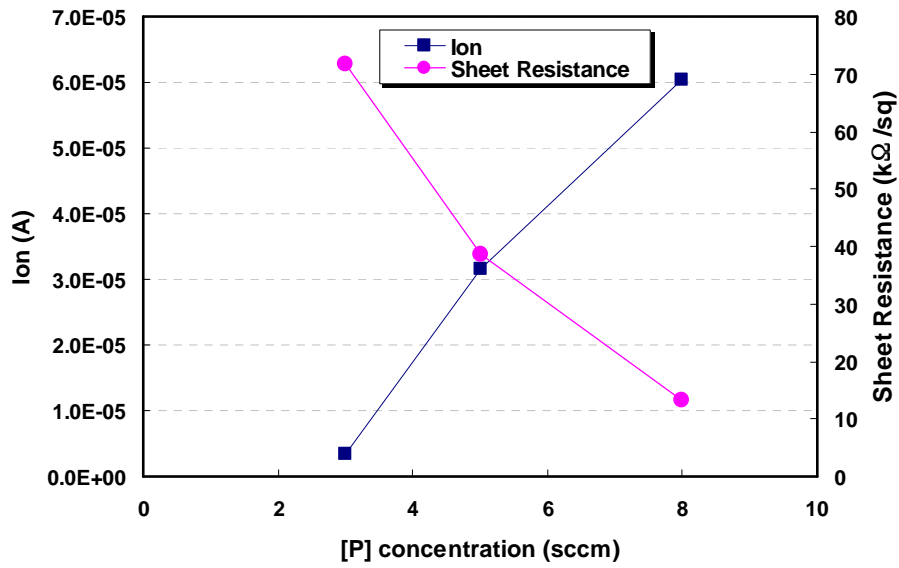
Fig. 34 The on-current (Ion) of Si films under different [P] concentration ([PH$_3$]

flow rates) and the corresponding sheet resistance (S.R.). From this figure, I$_{on}$

increases but sheet resistance (S.R.) decreases when the [P] concentration
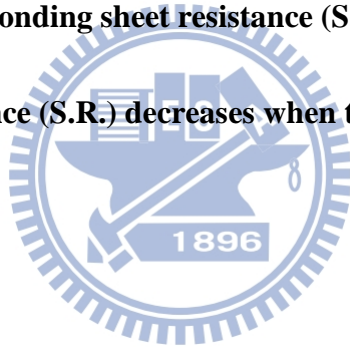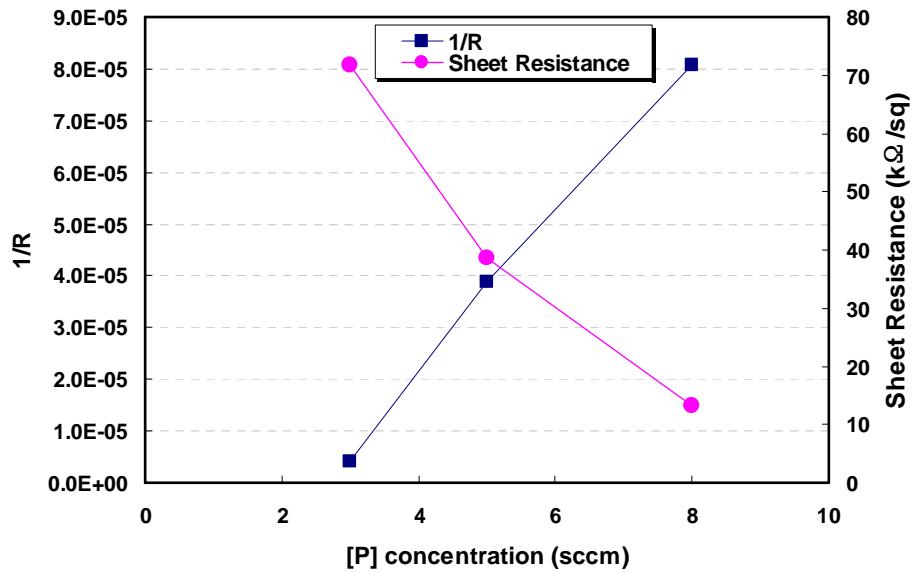
increases.

Fig. 35 The resistance (1/R) of Si films under different [P] concentration ([PH₃]

flow rates) and the corresponding sheet resistance (S.R.). From this figure, 1/R

increases but sheet resistance (S.R.) decreases when the [P] concentration
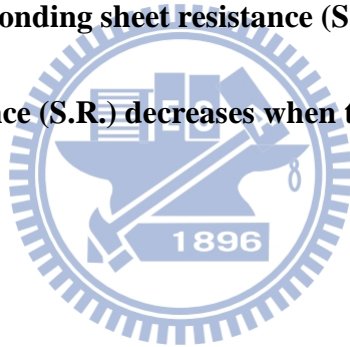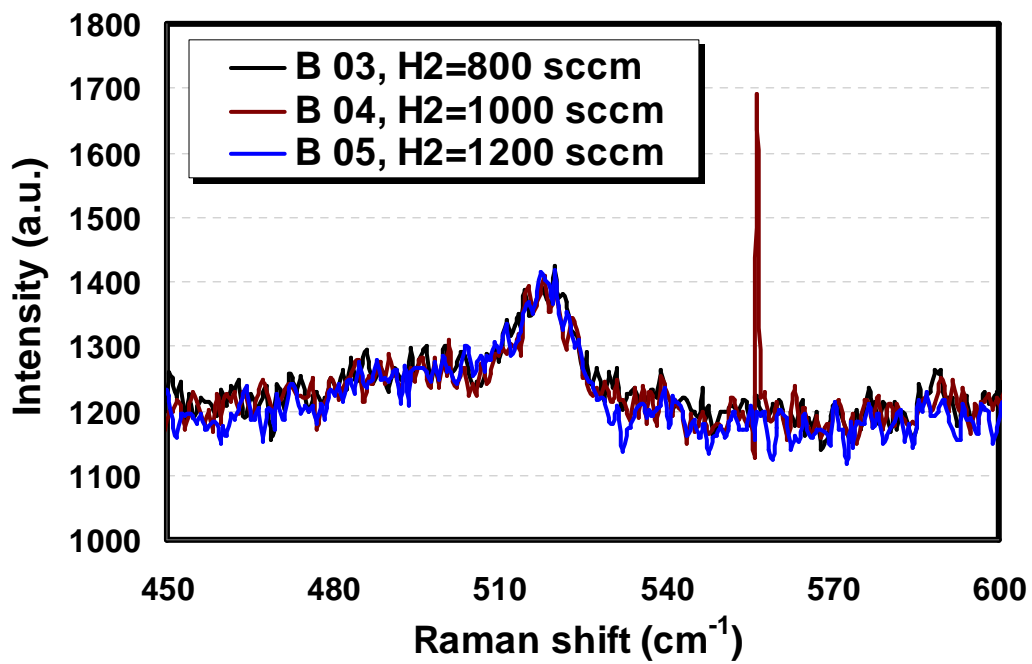
increases.

Fig. 36 The Raman spectrum of Si films when the H$_2$ flow increased from 800 sccm to 1000 sccm and 1200 sccm (B03/B04/B05).
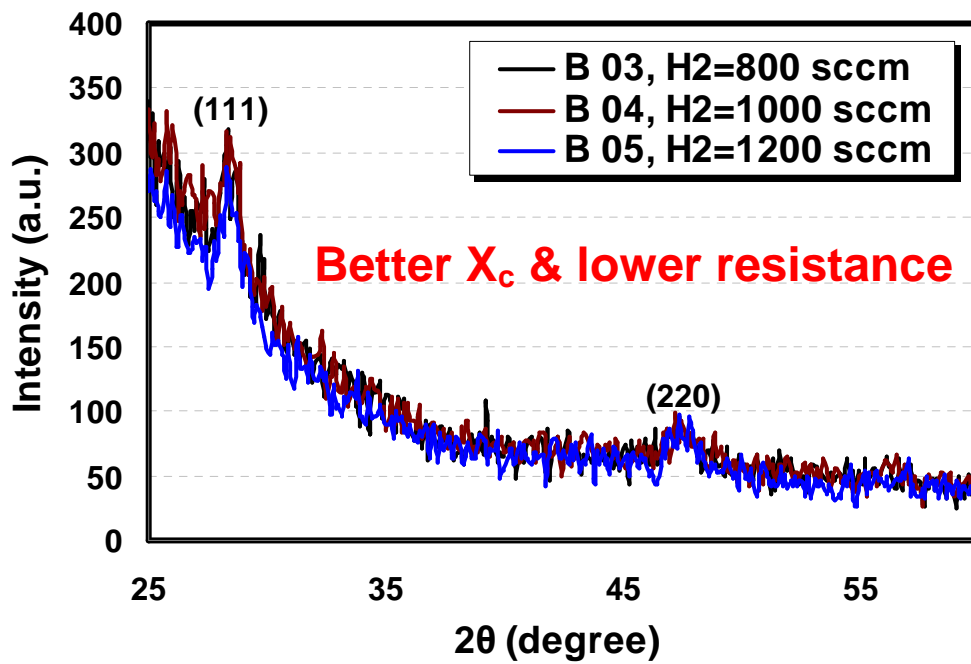
Fig. 37 The XRD spectrum of Si films when the H_2 flow increased from 800 sccm to 1000 sccm and 1200 sccm (B03/B04/B05).
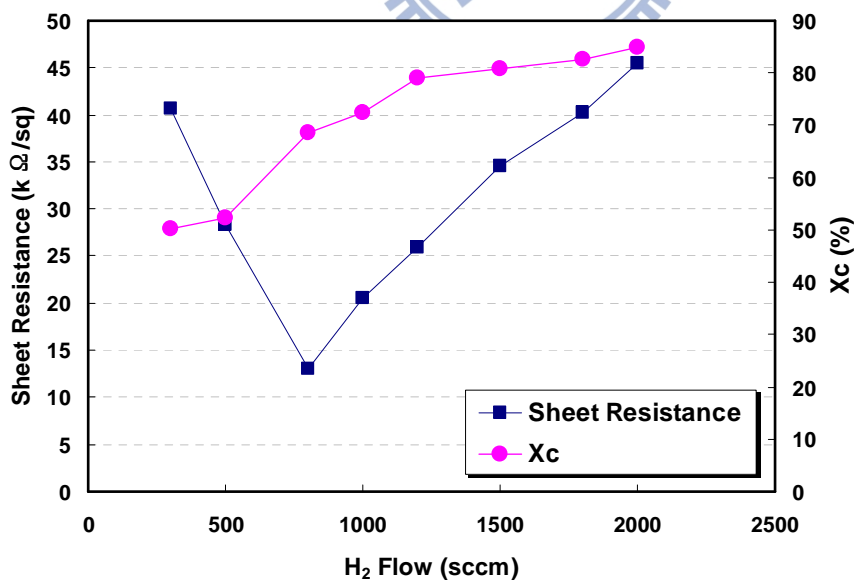
Fig. 38 The sheet resistance and Xc of Si film under different H_2 flow. We can see Xc increases when the H_2 flow increases.
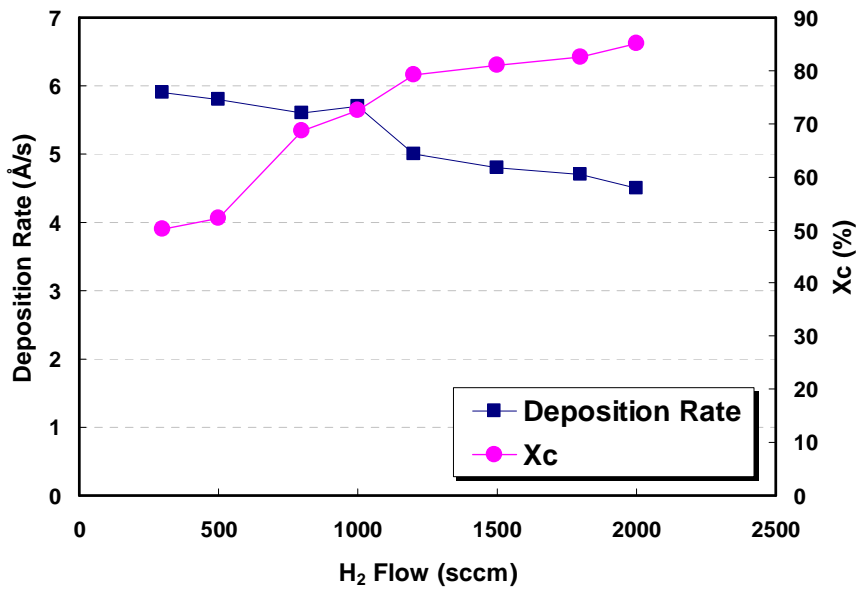
Fig. 39 The deposition rate and Xc of Si film under different H$_2$ flow. We can see deposition rate decreases, but Xc increases when the H$_2$ flow increases.

To much [B] degraded crystalline
(doping poison)
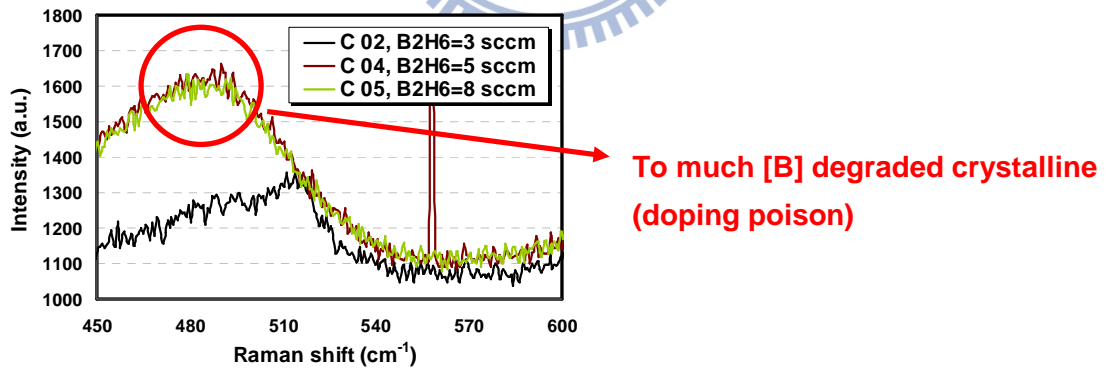
Fig. 40 Raman spectrum shows the Xc variations: [B] concentration ([B$_2$H$_6$] flow rates) increases from 3/5/8 sccm (C02/C04/C05), the decreases of Xc.
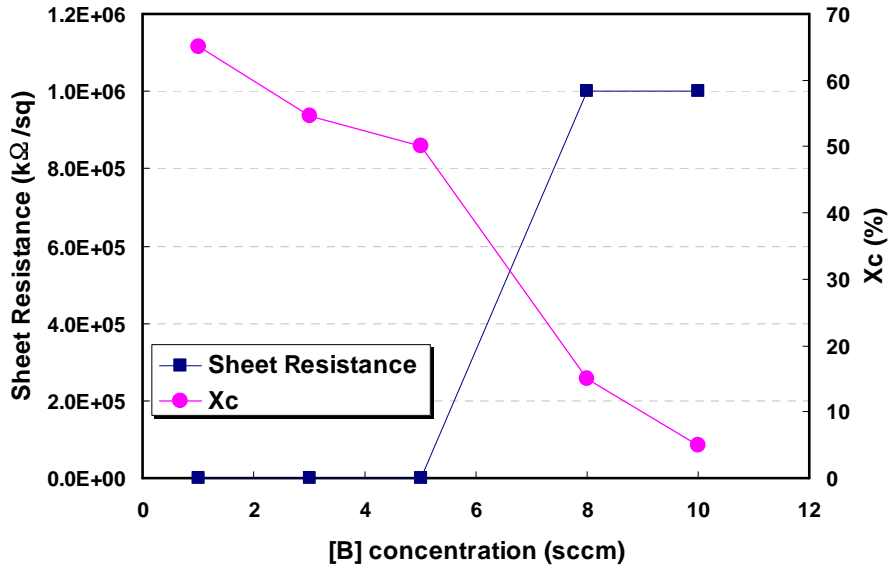
Fig. 41 The sheet resistance (S.R.) and Xc of Si film under different [B]

concentration ([B$_2$H$_6$] flow rates). Sheet resistance (S.R.) increases, but Xc

decreases when the [B] concentration increases.
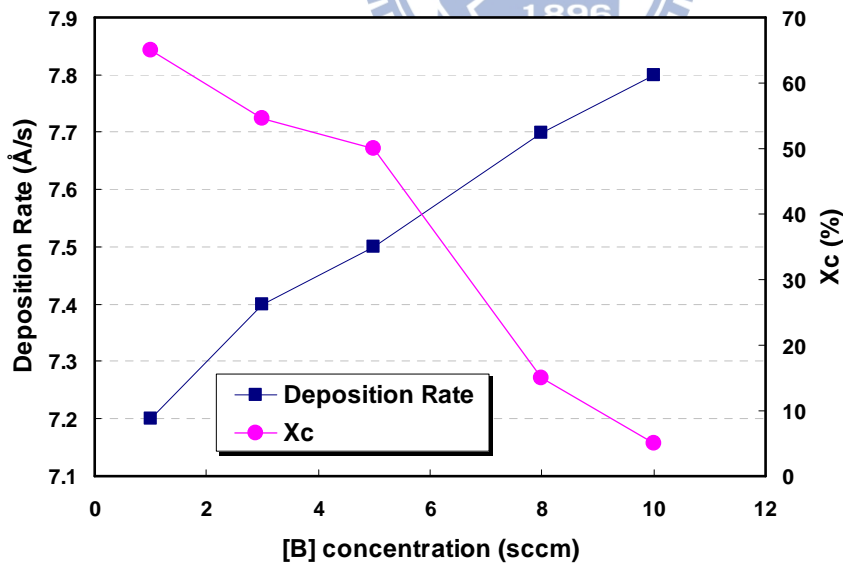
Fig. 42 The deposition rates (D.R.) and Xc of Si film under different [B]

concentration ([B$_2$H$_6$] flow rates). Deposition rate (D.R.) increases, but Xc

decreases when the [B] concentration increases.
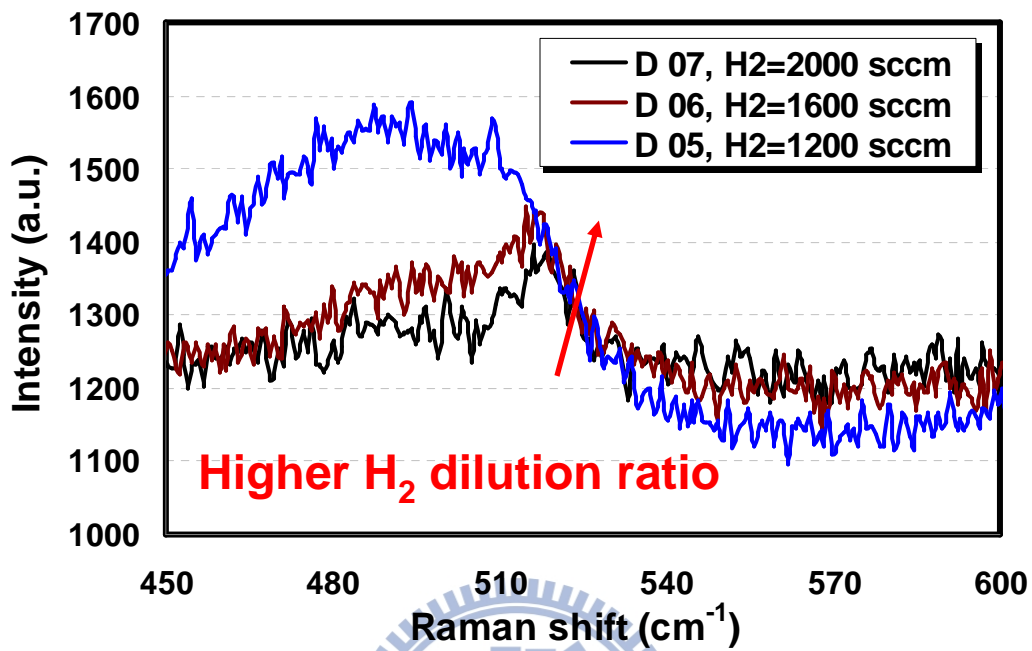
Fig. 43 Raman spectrum shows the Xc variations: H_2 flow increases from 1200/1600/2000 sccm (D05/D06/D07), the increases of Xc.
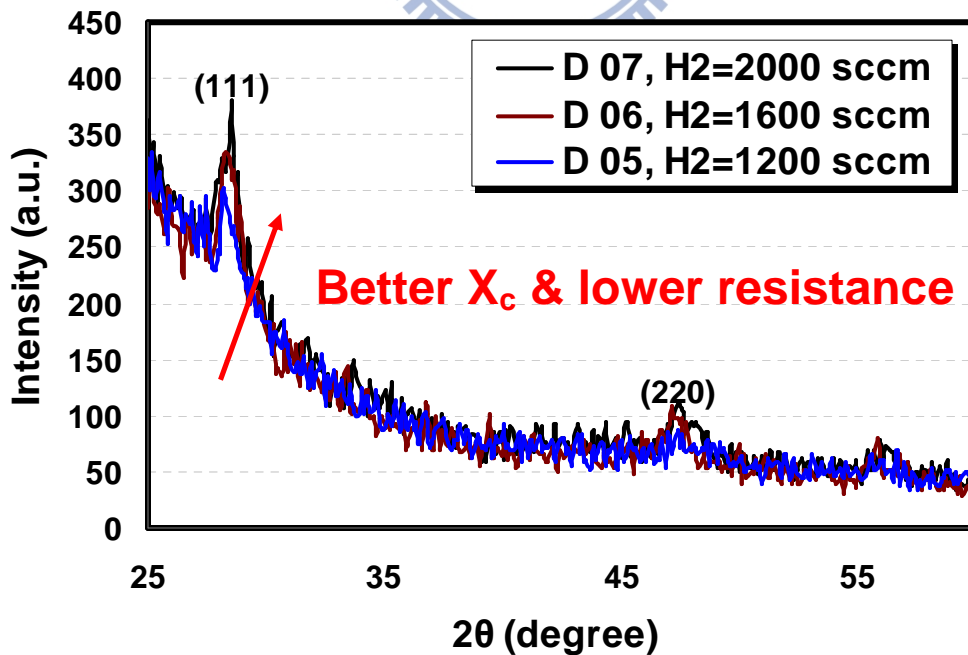
Fig. 44 XRD spectrum also shows the Xc variations: H_2 flow increases from 1200/1600/2000 sccm (D05/D06/D07), the increases of Xc
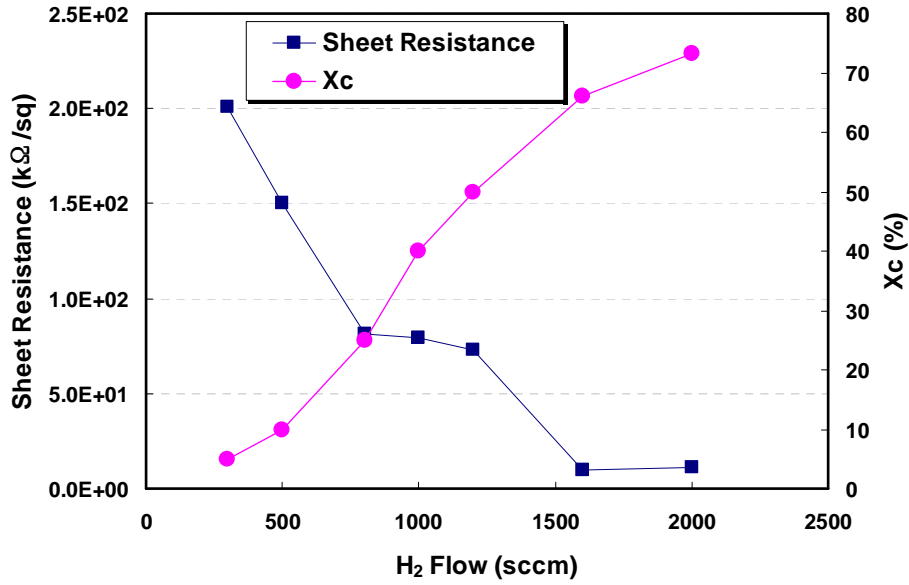
Fig. 45 The sheet resistance (S.R.) and Xc of Si film under different H₂ flow. We can see sheet resistance decreases, but Xc increases when the H₂ flow increases.
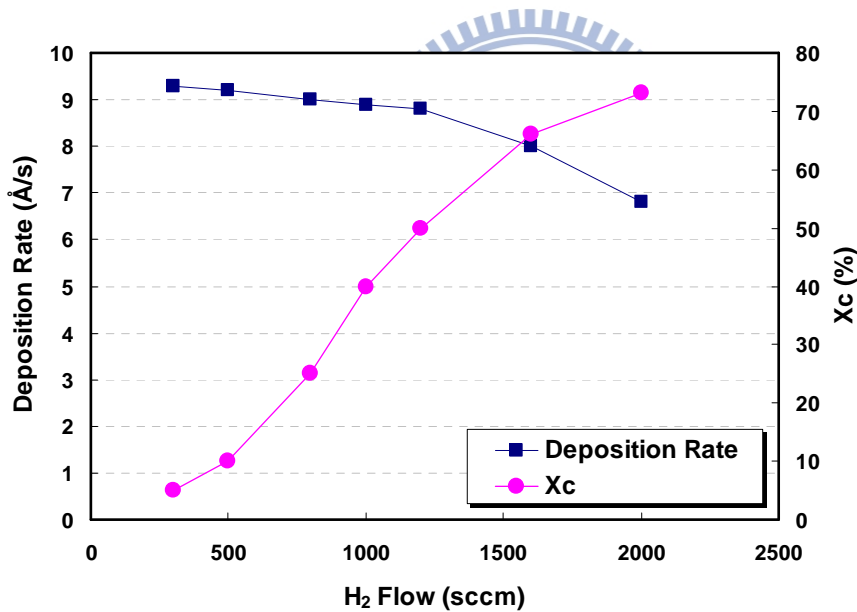
Fig. 46 The deposition rate (D.R.) and Xc of Si film under different H₂ flow. We can see deposition rate decreases, but Xc increases when the H₂ flow increases.
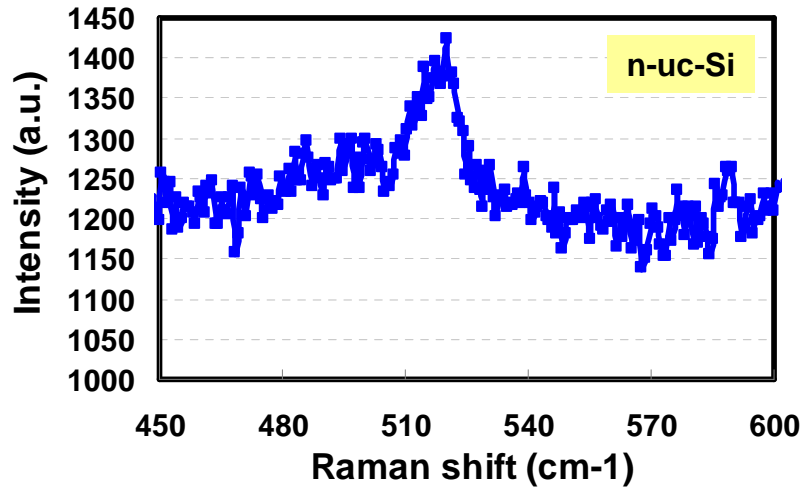
(a)
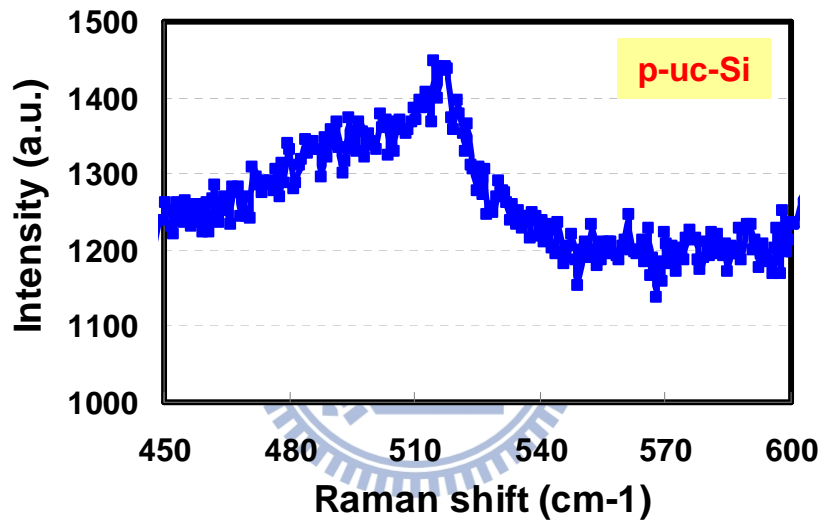
(b)

Fig. 47 Raman spectrum of optimized Si thin-film for HIT solar cell. (a) Raman spectrum of optimized n-type Si films. (b) Raman spectrum of optimized p-type Si films.
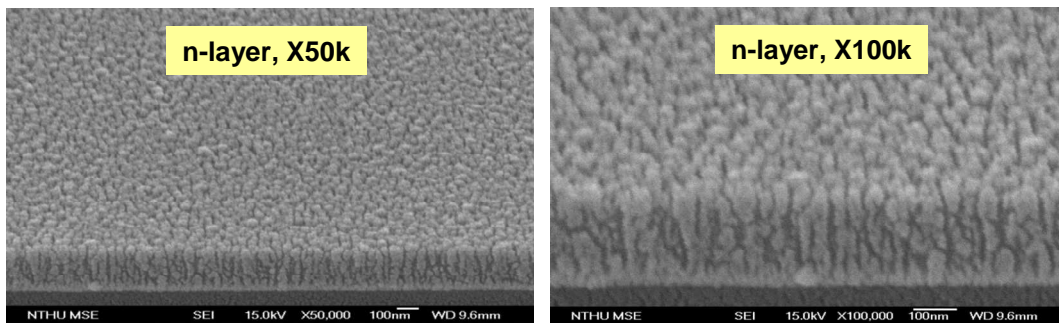
(a)   **(b)**

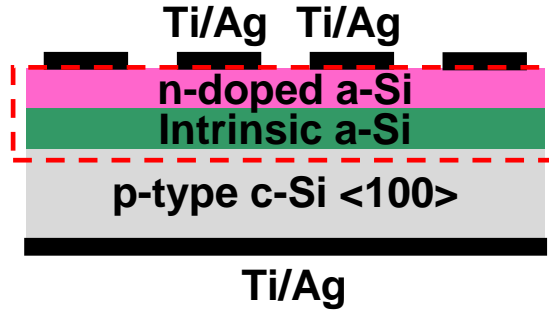**Fig. 48 The cross section SEM images of the n-uc-Si film. (a) X50k (b) X100k**
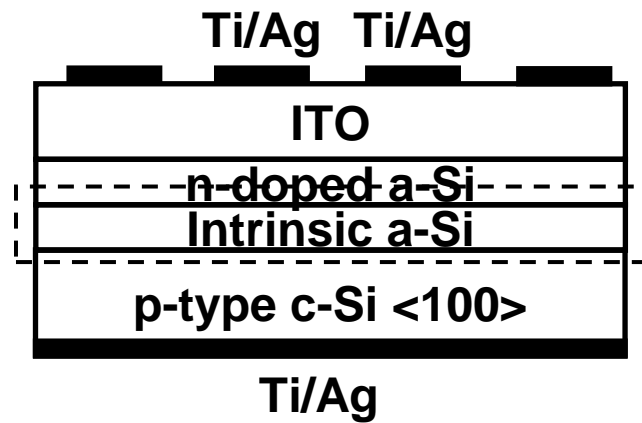
Fig. 49 The single side HIT solar cell structure. We used AMPS-1D to simulate

HIT solar cell performance under different i-a-Si film thickness (marked by

dotted line).
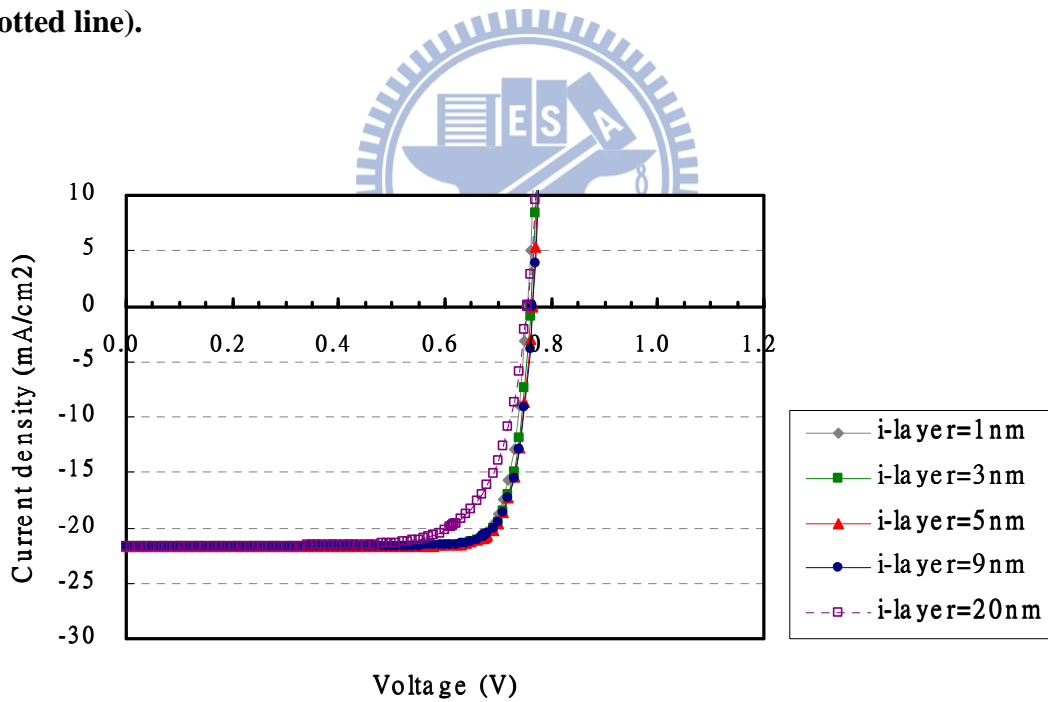
Fig. 50 The photo IV curves of AMPS-1D simulation by adjusting i-a-Si (i-layer)
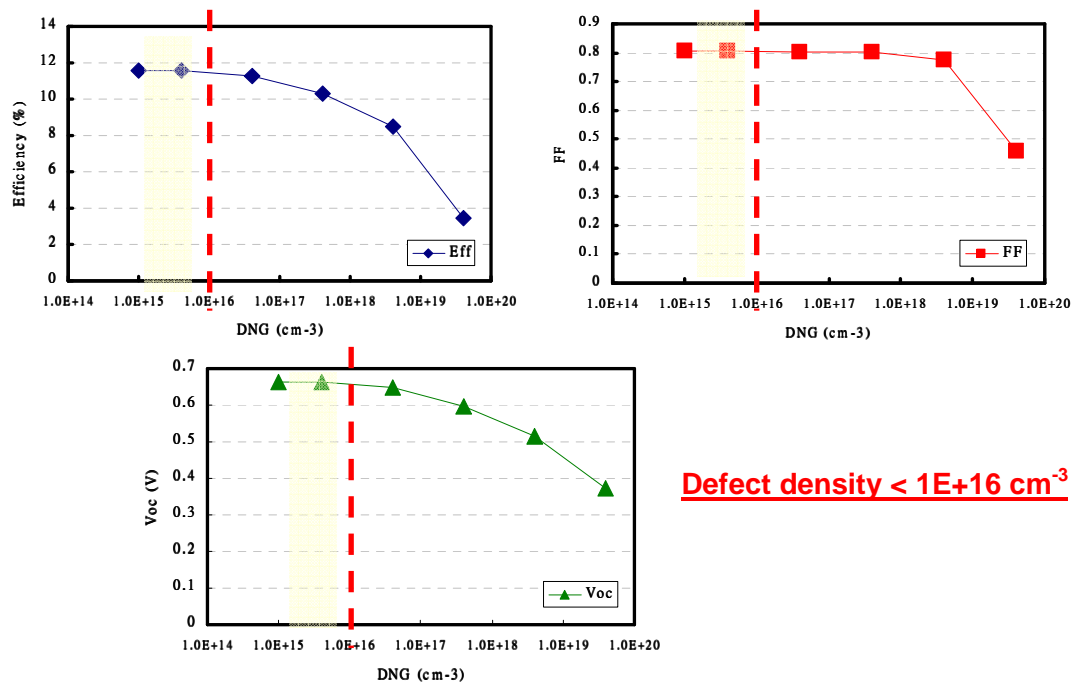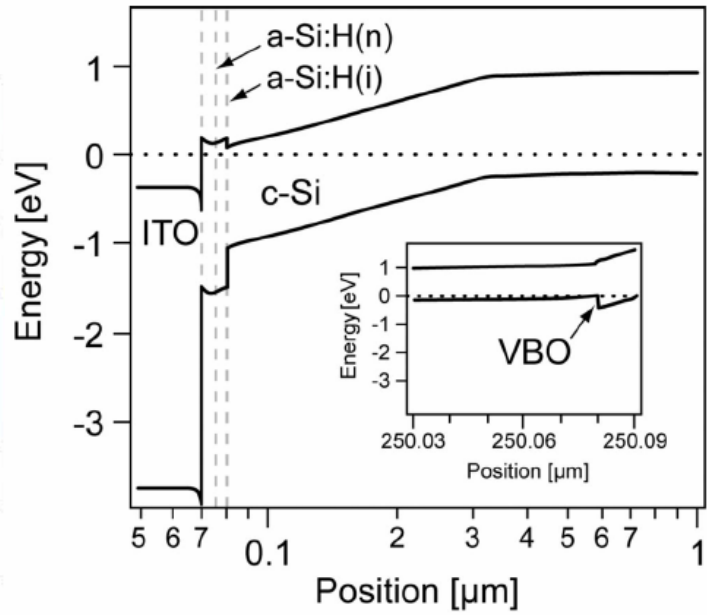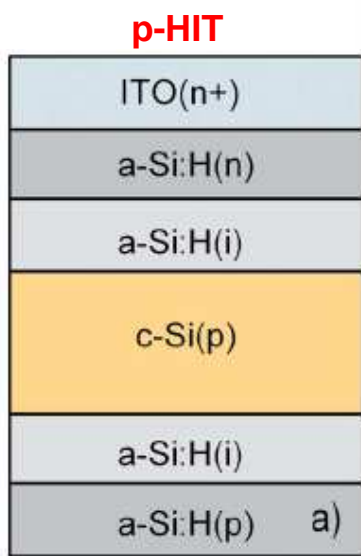
films of HIT solar cells.

(a)   **(b)**
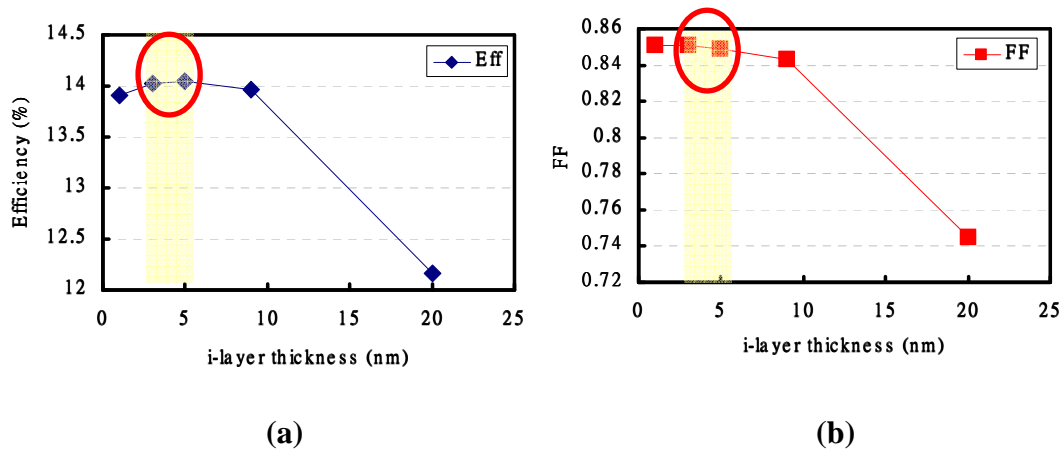
Fig. 51 The summary of AMPS-1D simulation results of HIT solar cells. (a) The

HIT solar cell efficiency (Eff.) under various i-a-Si (i-layer) film thicknesses. (b)

The HIT solar cell fill factor (F. F.) under various i-a-Si (i-layer) film thicknesses.

From these two figures, the optimization of i-a-Si (i-layer) film thickness in HIT

solar cell is 3~5 nm.
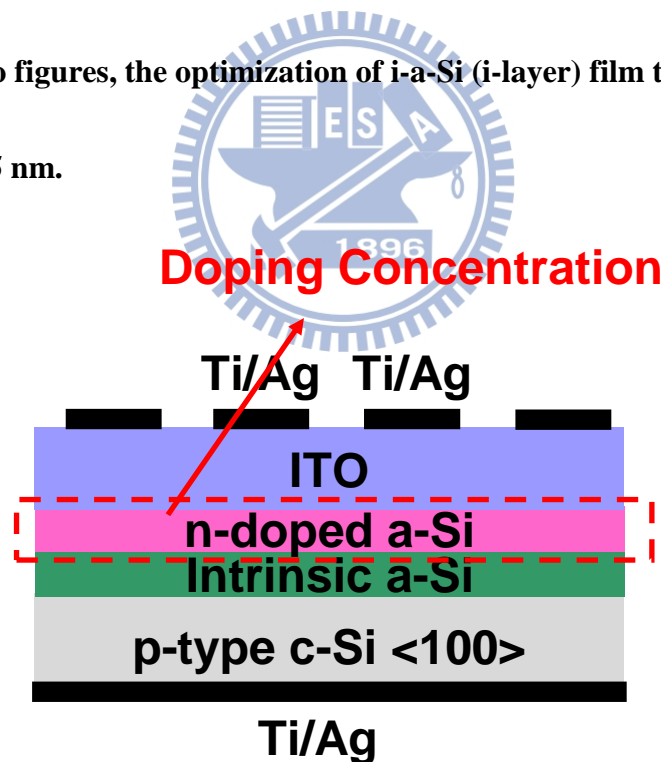
Fig. 52 The single side HIT solar cell structure. We used AMPS-1D to simulate

HIT solar cell performance under different n-a-Si film doping concentrations

(Marked by dotted line).
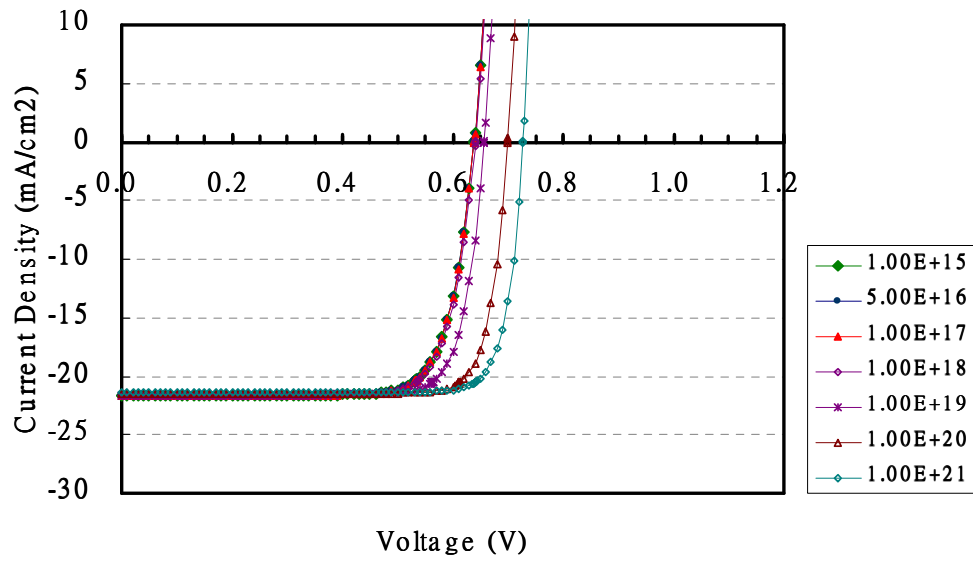
Fig. 53 The photo IV curves of AMPS-1D simulation by adjusting n-a-Si (n-layer)

doping concentrations of HIT solar cells.
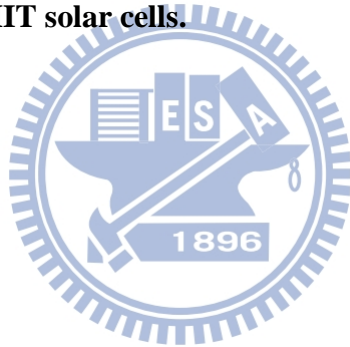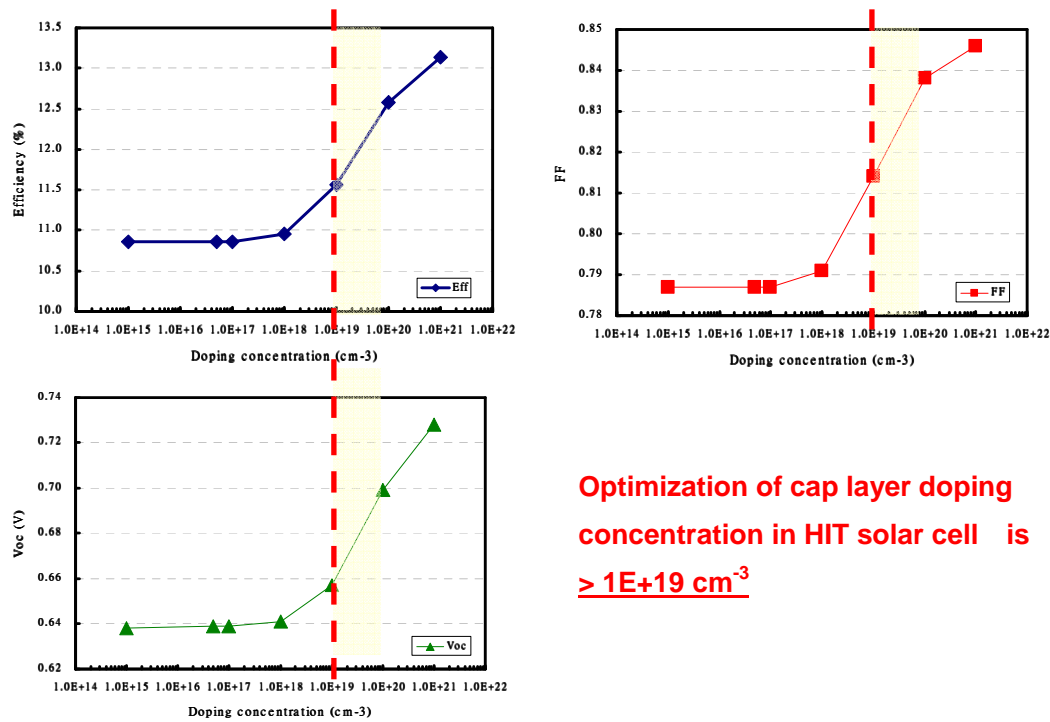
Optimization of cap layer doping concentration in HIT solar cell is > 1E+19 cm^{-3}

Fig. 54 The summary of AMPS-1D simulation results of HIT solar cells. (a) The HIT solar cell efficiency (Eff.) under various n-a-Si (n-layer) doping concentrations of HIT solar cells. (b) The HIT solar cell fill factor (F. F.) under various n-a-Si (n-layer) doping concentrations of HIT solar cells. (c) The HIT solar cell open-circuit voltage (Voc) under various n-a-Si (n-layer) doping concentrations of HIT solar cells. From these three figures, the optimization of n-a-Si (n-layer) doping concentrations in HIT solar cell is > 1E+19 cm^{-3}.

Fig. 55 The single side HIT solar cell structure. We used AMPS-1D to simulate HIT solar cell performance under different defect densities of n-a-Si / i-a-Si films (marked by dotted line).
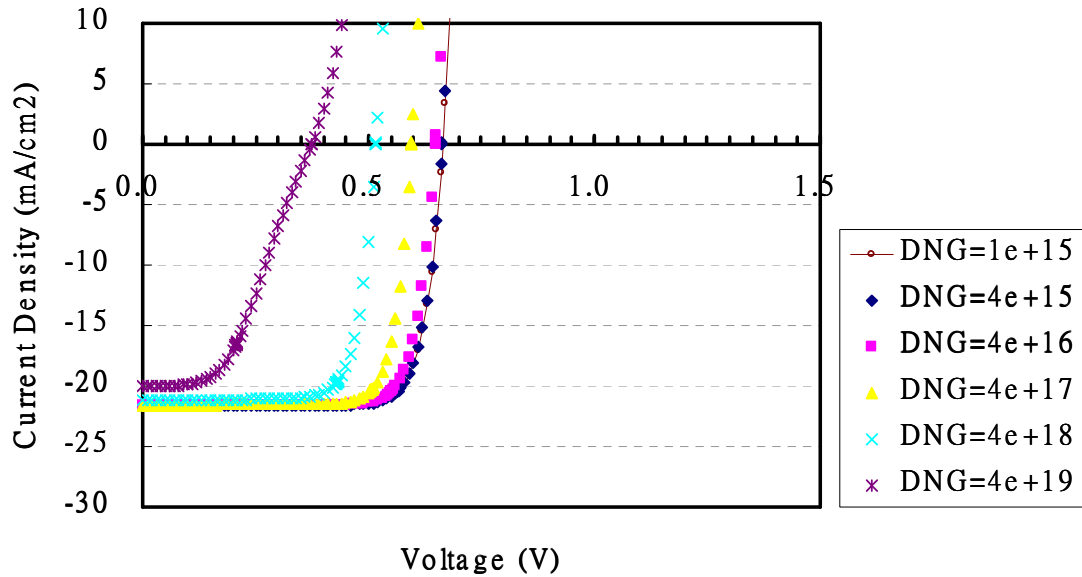
Fig. 56 The photo IV curves of AMPS-1D simulation by adjusting defect densities of n-a-Si / i-a-Si films in HIT solar cells.

Fig. 57 The summary of AMPS-1D simulation results of HIT solar cells. (a) The HIT solar cell efficiency (Eff.) under various defect densities of n-a-Si / i-a-Si films in HIT solar cells. (b) The HIT solar cell fill factor (F. F.) under various defect densities of n-a-Si / i-a-Si films in HIT solar cells. (c) The HIT solar cell open-circuit voltage (Voc) under various defect densities of n-a-Si / i-a-Si films in HIT solar cells. From these three figures, the defect densities of n-a-Si / i-a-Si films in HIT solar cells is < 1E+16 cm^{-3}.

p-HIT

| ITO(n+) |
| a-Si:H(n) |
| a-Si:H(i) |
| c-Si(p) |
| a-Si:H(i) |
| a-Si:H(p) a) |

(VBO: Valence Band Offset)

(a)   (b)

Fig. 58 (a) The structure of HIT solar cell with p-type c-Si substrate. (b) The

energy bandgap diagram of HIT solar cell with p-type c-Si substrate.
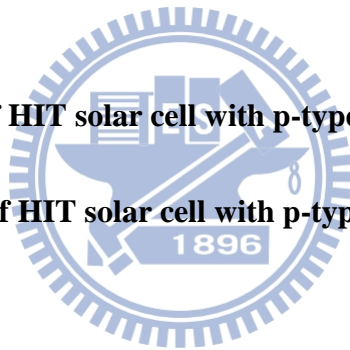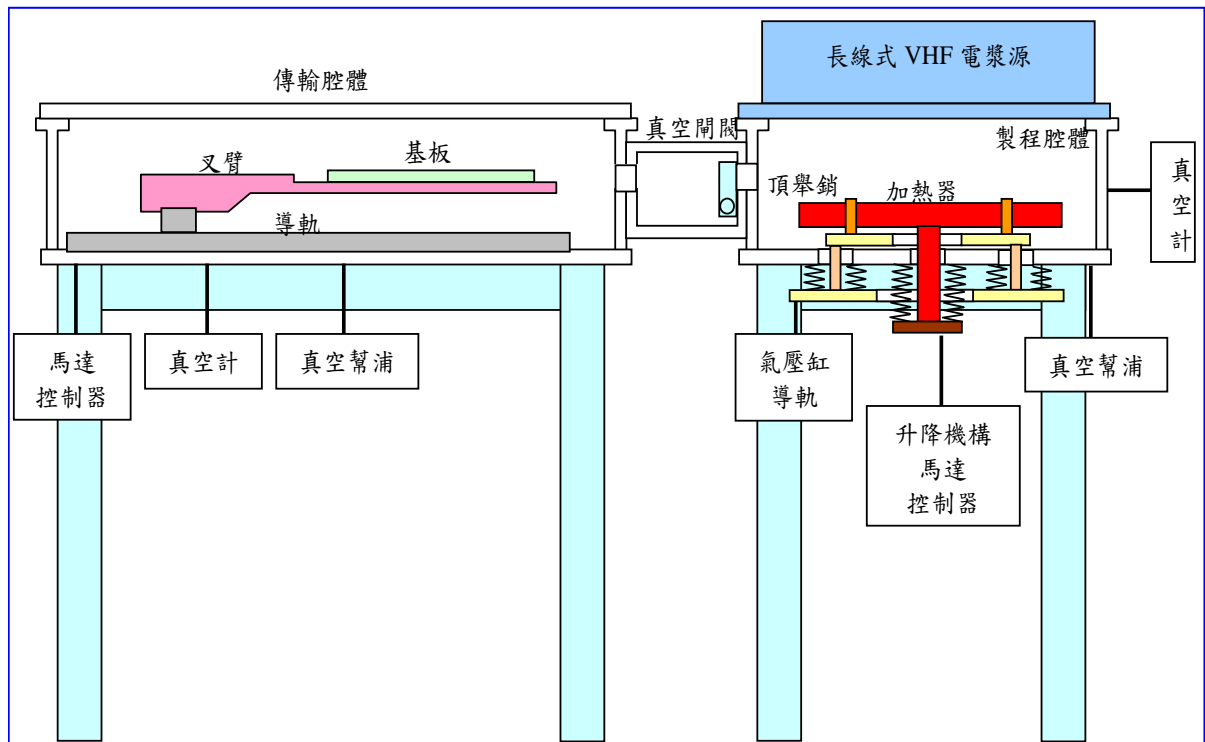
(a)傳輸與製程反應系統圖
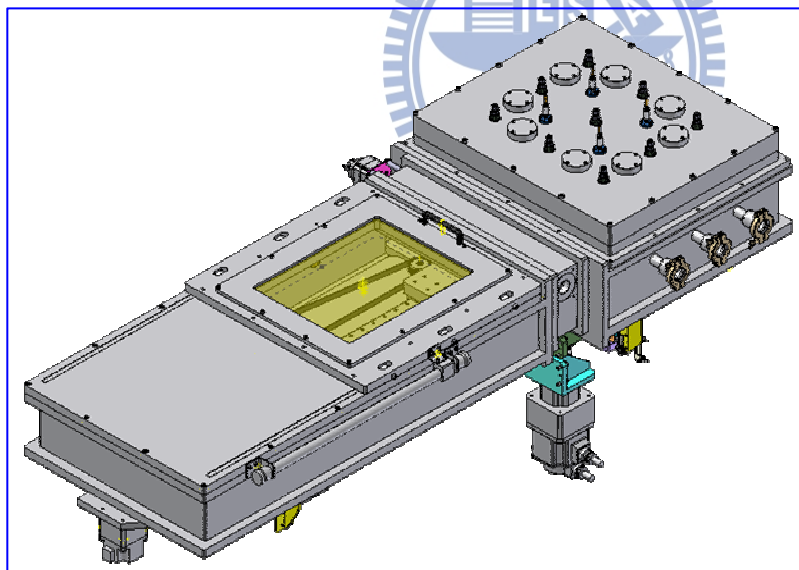
(b)傳輸與製程反應系統 3D 圖

Fig. 59 The 40.68MHz VHF-PECVD system. (a) The internal structure of 40.68MHz VHF-PECVD system. (b) The external structure of 40.68MHz VHF-PECVD system.

Single Side

Double Side (Solar Cell Structure)
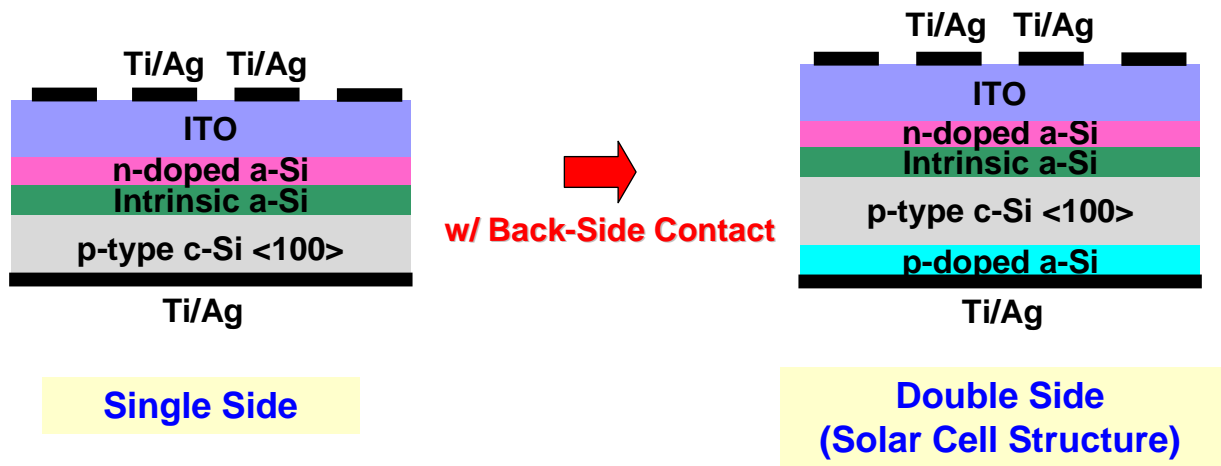
Fig. 60 The structures of single side HIT solar cell and double side HIT solar cell with back side contact (p-doped a-Si).

p-type c-Si <100>	**Standard RCA clean Dilute hydrofluoric acid (DHF) clean**

⬇

Intrinsic a-Si	**i-a-Si film deposition by VHF-PECVD**
p-type c-Si <100>	

⬇

n-doped a-Si	**n-a-Si film deposition by VHF-PECVD**
Intrinsic a-Si	
p-type c-Si <100>	

⬇

ITO	
n-doped a-Si	**ITO layer by E-gun Evaporation**
Intrinsic a-Si	
p-type c-Si <100>	

⬇

Ti/Ag Ti/Ag	**Electrode (Ti/Ag) by E-gun Evaporation**
ITO	
n-doped a-Si	**Single Side**
Intrinsic a-Si	
p-type c-Si <100>	
Ti/Ag	

Fig. 61 The single-side HIT solar cell fabrication.
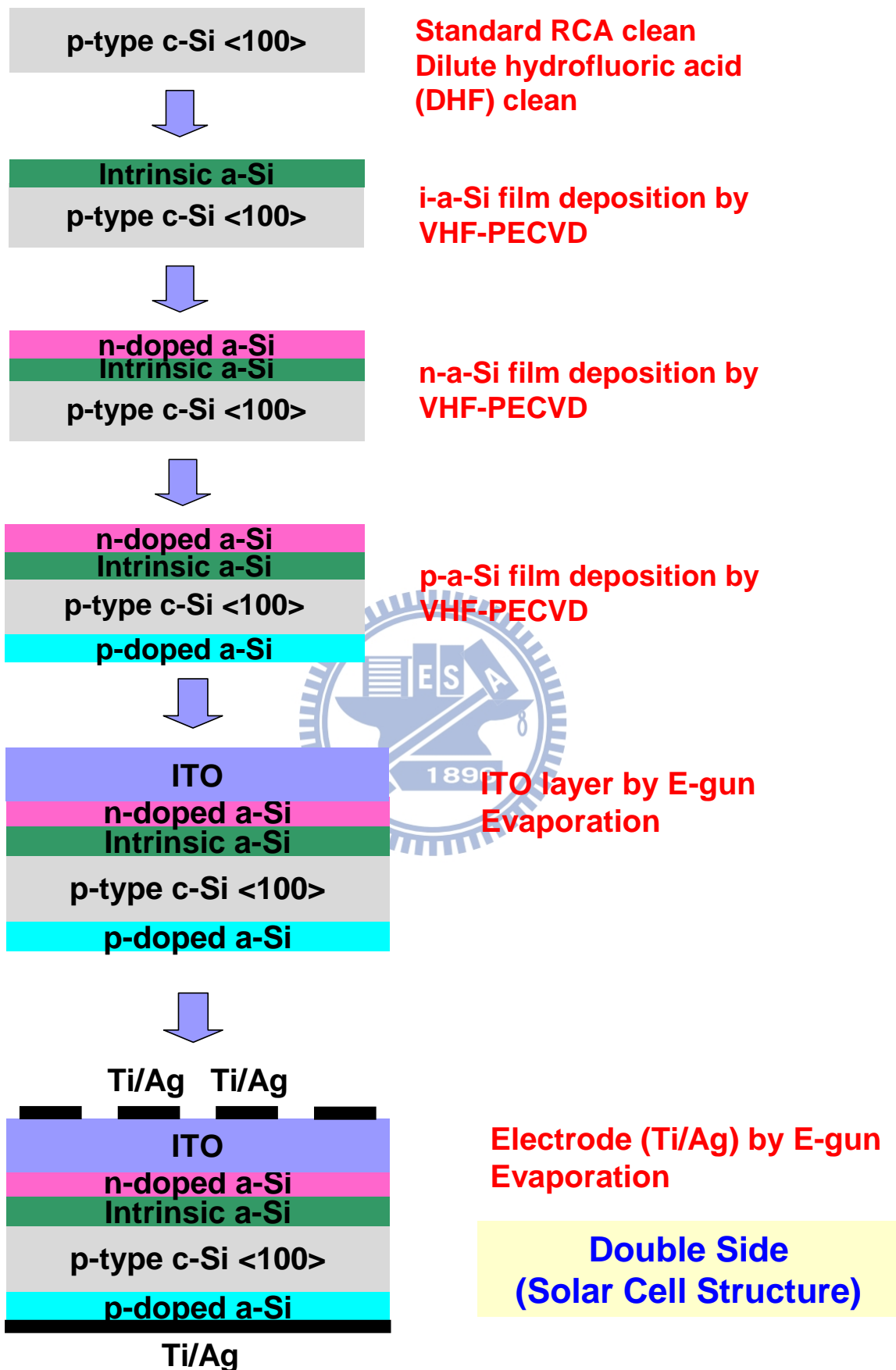
Fig. 62 The double-side HIT solar cell fabrication.

p-type c-Si <100>
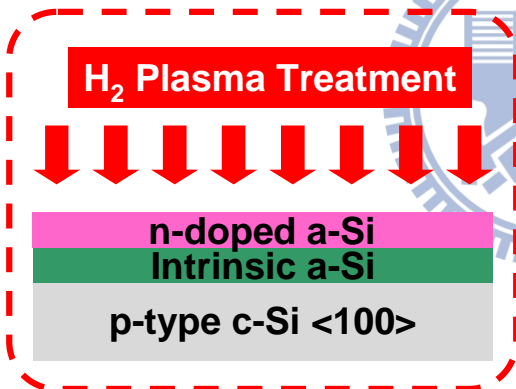
Standard RCA clean
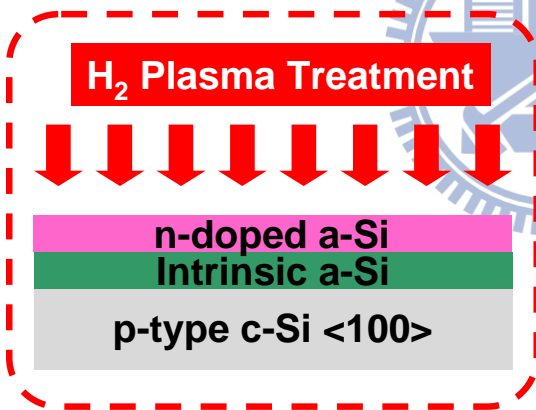Dilute hydrofluoric acid (DHF) clean

Intrinsic a-Si
p-type c-Si <100>

i-a-Si film deposition by VHF-PECVD

n-doped a-Si
Intrinsic a-Si
p-type c-Si <100>

n-a-Si film deposition by VHF-PECVD

H₂ Plasma Treatment

n-doped a-Si
Intrinsic a-Si
p-type c-Si <100>

Post-anneal H₂ treatment on HIT solar cell

ITO layer by E-gun Evaporation

Electrode (Ti/Ag) by E-gun Evaporation
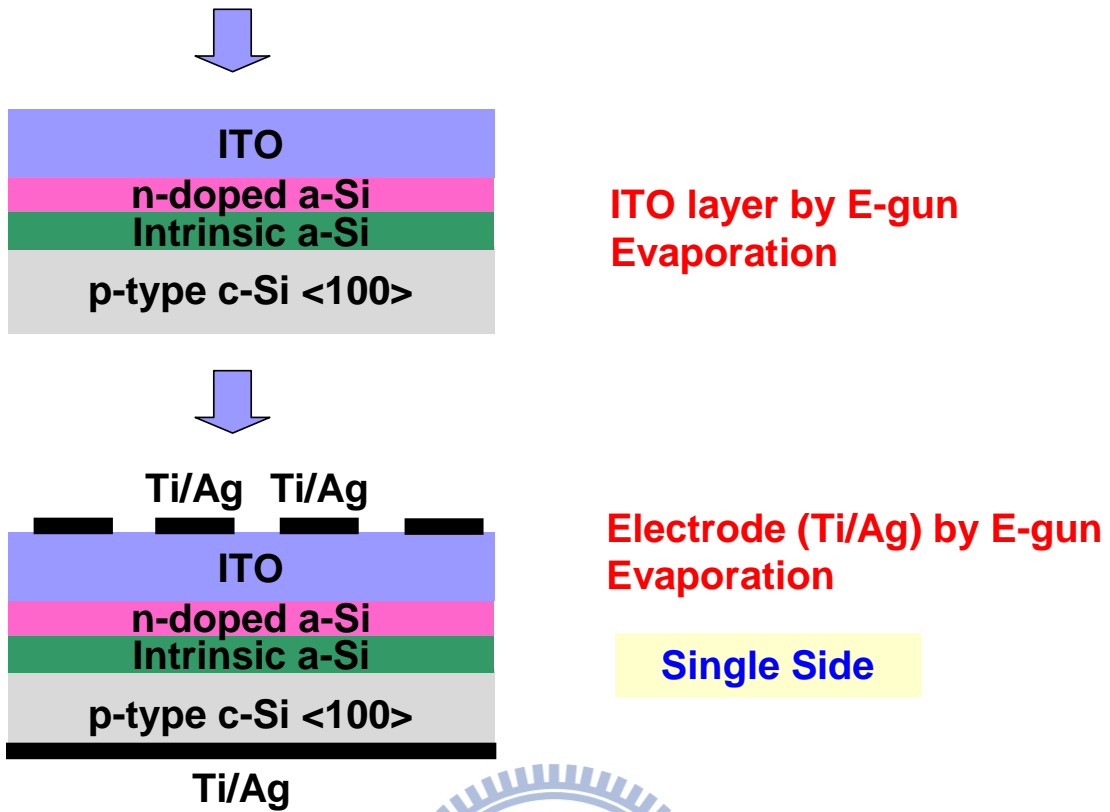
Single Side

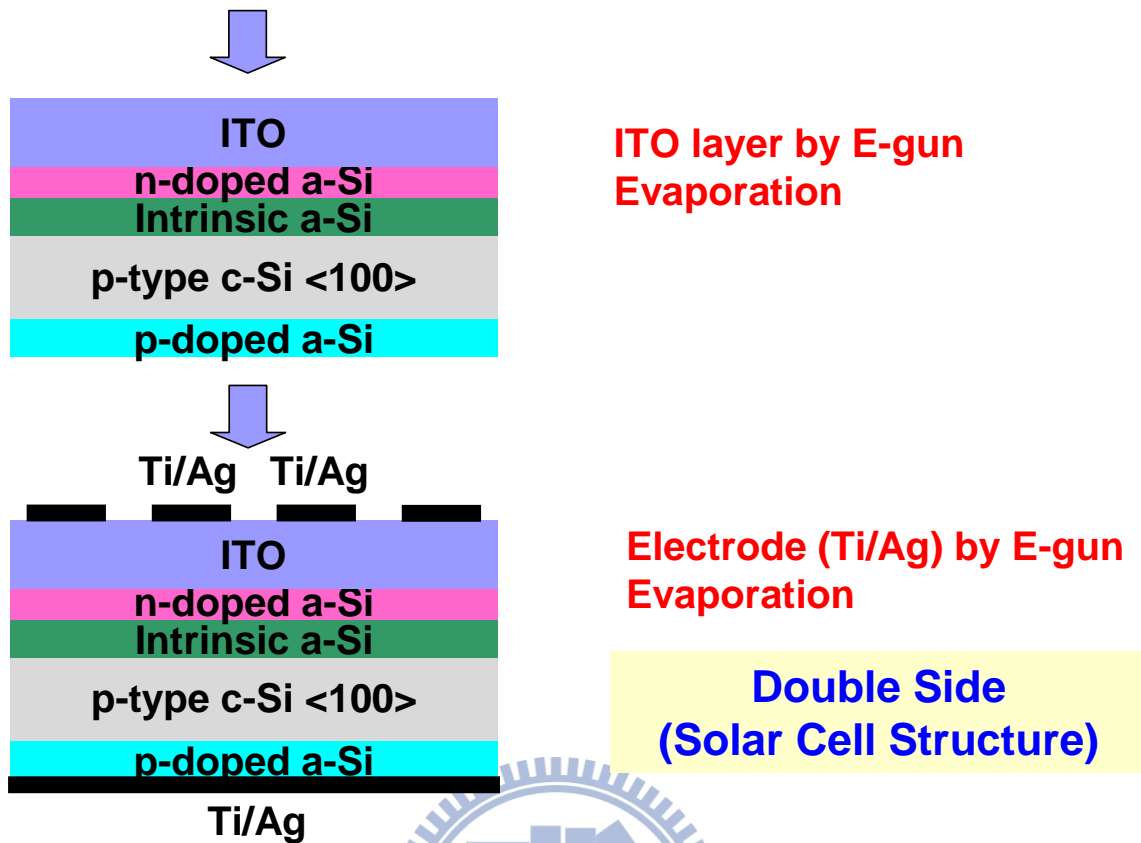**Fig. 63 The single-side HIT solar cell deposition under post H$_2$ plasma treatment process**

p-type c-Si <100>

Standard RCA clean
Dilute hydrofluoric acid (DHF) clean

Intrinsic a-Si
p-type c-Si <100>

i-a-Si film deposition by VHF-PECVD

n-doped a-Si
Intrinsic a-Si
p-type c-Si <100>

n-a-Si film deposition by VHF-PECVD

H$_2$ Plasma Treatment
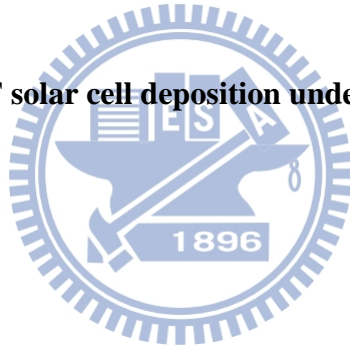
n-doped a-Si
Intrinsic a-Si
p-type c-Si <100>

Post-anneal H$_2$ treatment on HIT solar cell

n-doped a-Si
Intrinsic a-Si
p-type c-Si <100>
p-doped a-Si

p-a-Si film deposition by VHF-PECVD

ITO layer by E-gun Evaporation

Electrode (Ti/Ag) by E-gun Evaporation

Double Side (Solar Cell Structure)

Fig. 64 The double-side HIT solar cell deposition under post H$_2$ plasma treatment process
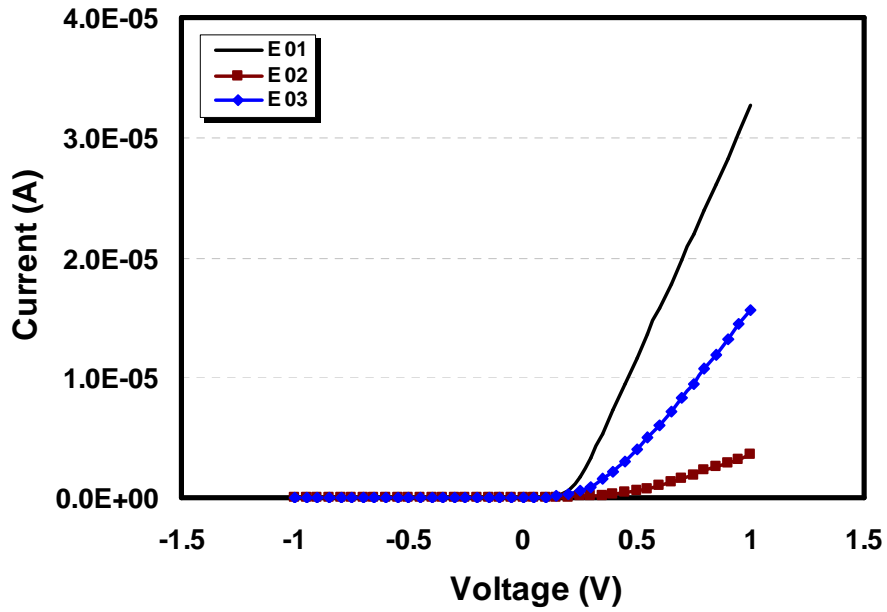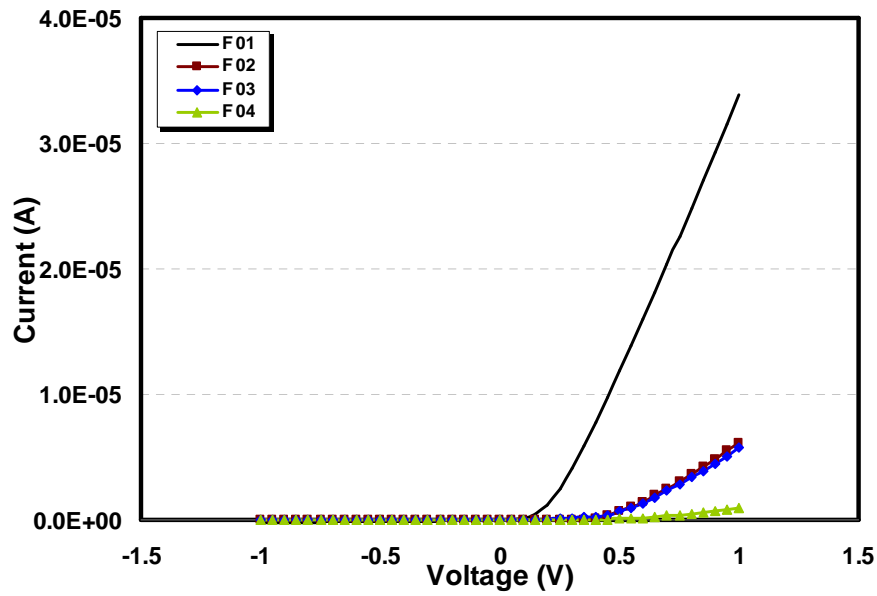
(a)
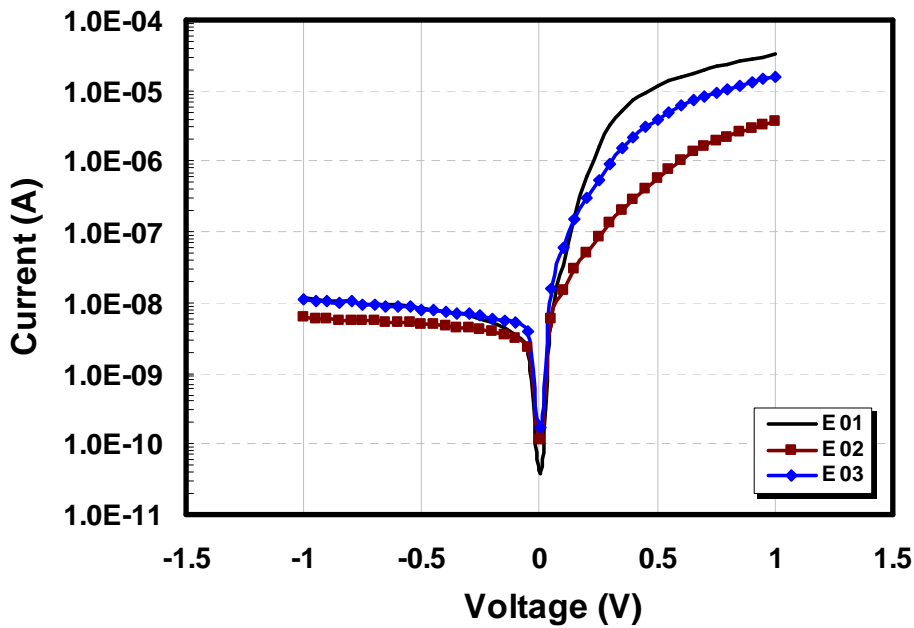
(b)

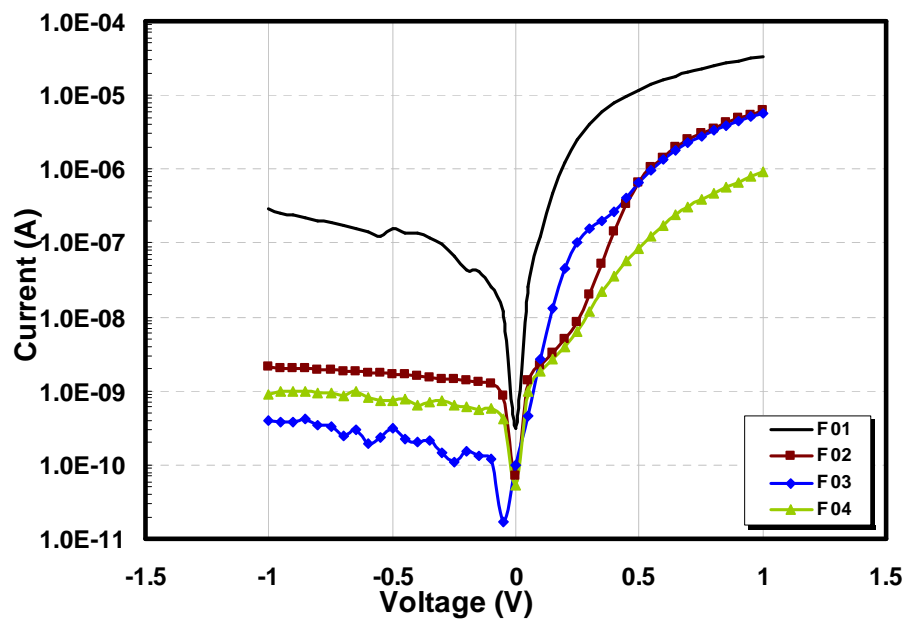**Fig. 65 Dark I-V curves of HIT solar cell deposited by 40.68MHz VHF-PECVD under various H_2 flow of post H_2 plasma treatment. Sample E01 is baseline. Sample E02 is treated by H_2 flux 600sccm, and Sample E03 is treated by H_2 flux 1200sccm. (a) Dark I-V curves. (b) Log scales of dark I-V curves from (a).**

Fig. 66 Dark I-V curves of HIT solar cell deposited by 40.68MHz VHF-PECVD under various H_2 plasma power of post H_2 plasma treatment. Sample F01 is baseline. Sample F02, F03, and F04 are under post H_2 plasma power 200W, 150W, and 100W, individually. (a) Dark I-V curves. (b) Log scales of dark I-V curves from (a).
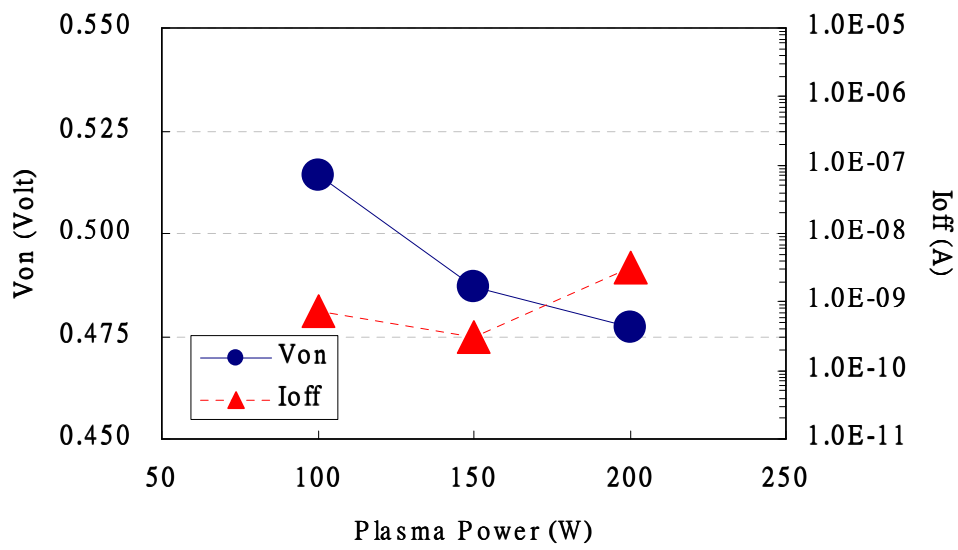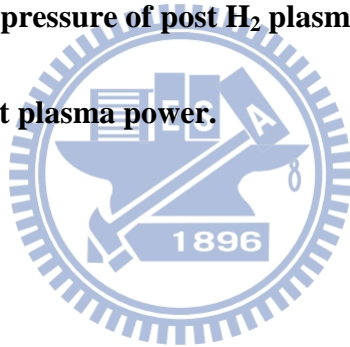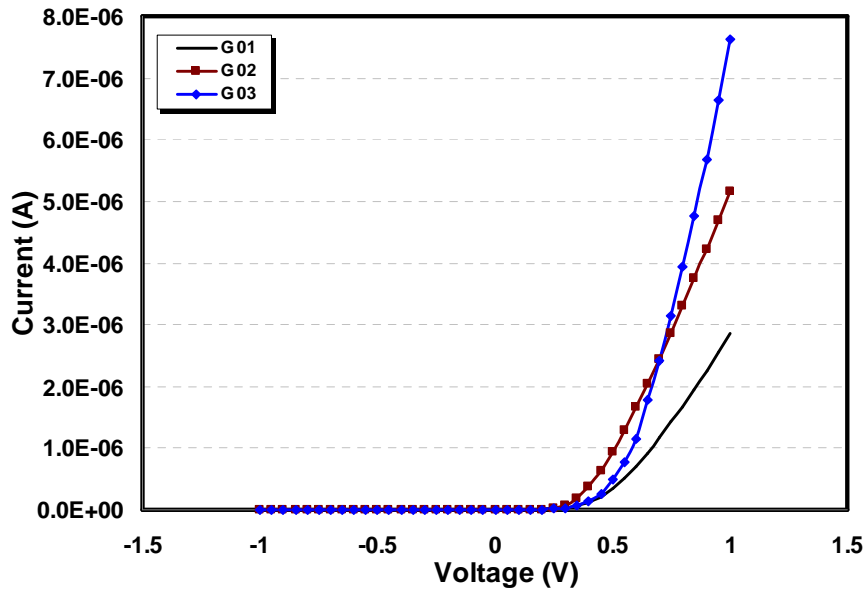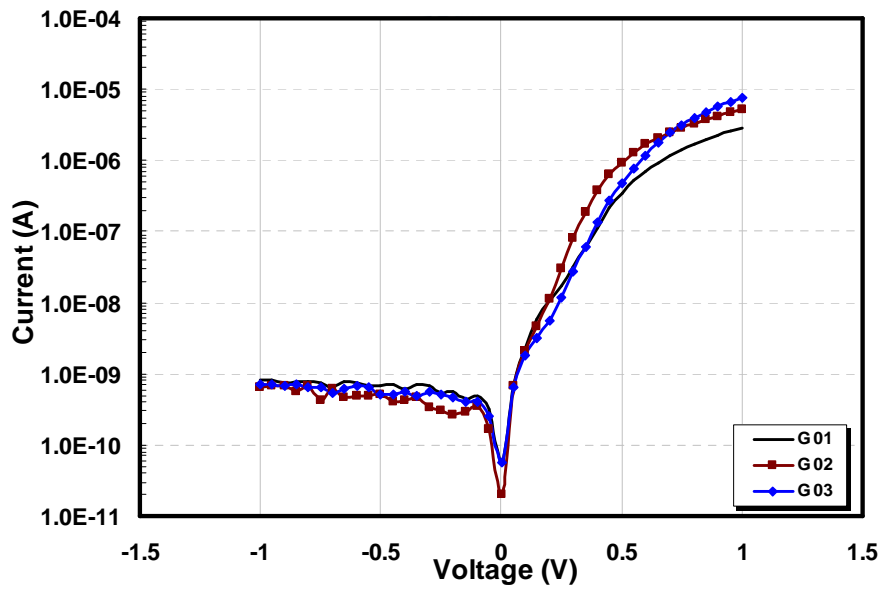
Fig. 67 The summary of HIT solar cell V_{on}, I_{on}, and I_{off} of HIT solar cell under various plasma power and pressure of post H_2 plasma treatment. The V_{on} and I_{off} were varied under different plasma power.

(a)

(b)

Fig. 68 Dark I-V curves of HIT solar cell deposited by 40.68MHz VHF-PECVD under various H_2 plasma pressure of post H_2 plasma treatment. Sample G01, G02, and G03 are under post H_2 plasma pressure 2.25 Torr, 1.5 Torr, and 0.75 Torr, individually. (a) Dark I-V curves. (b) Log scales of dark I-V curves from (a).
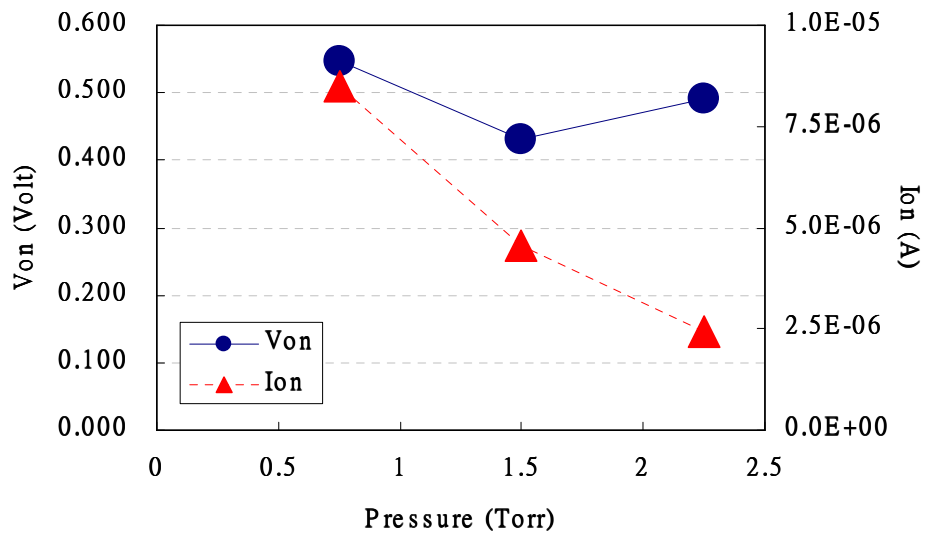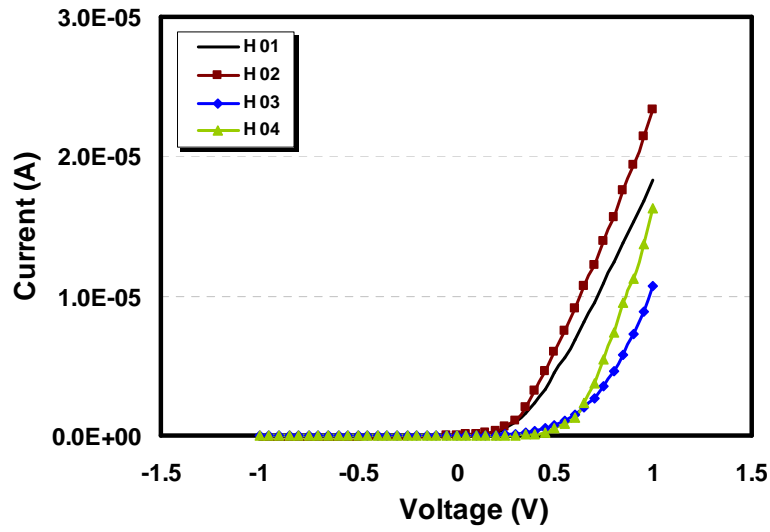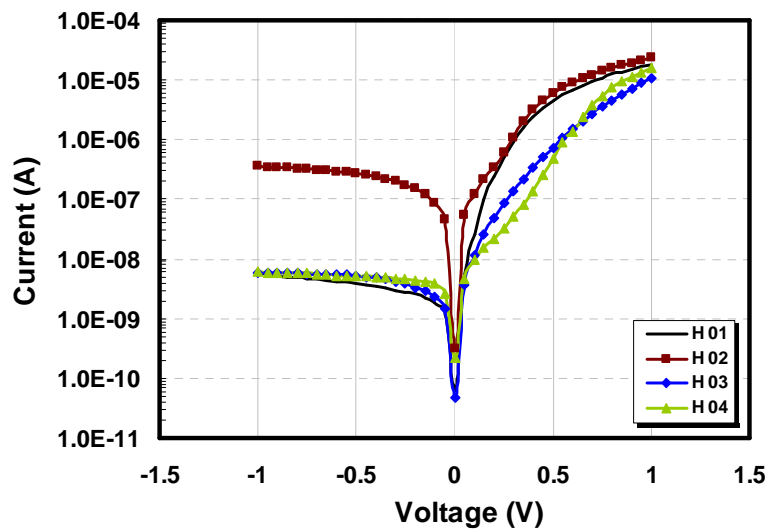
Fig. 69 The summary of HIT solar cell V_{on}, I_{on}, and I_{off} of HIT solar cell under various pressure of post H_2 plasma treatment. The V_{on} and I_{on} were changed under various pressure.

(a)

(b)

Fig. 70 Dark I-V curves of HIT solar cell deposited by 40.68 MHz VHF-PECVD under various post H$_2$ plasma treatment time. Sample H01 is baseline without post H$_2$ plasma treatment. Sample H02, H03, and H04 are under post H$_2$ plasma time 10 sec, 30 sec, and 50 sec, individually. (a) Dark I-V curves. (b) Log scales of dark I-V curves from (a).

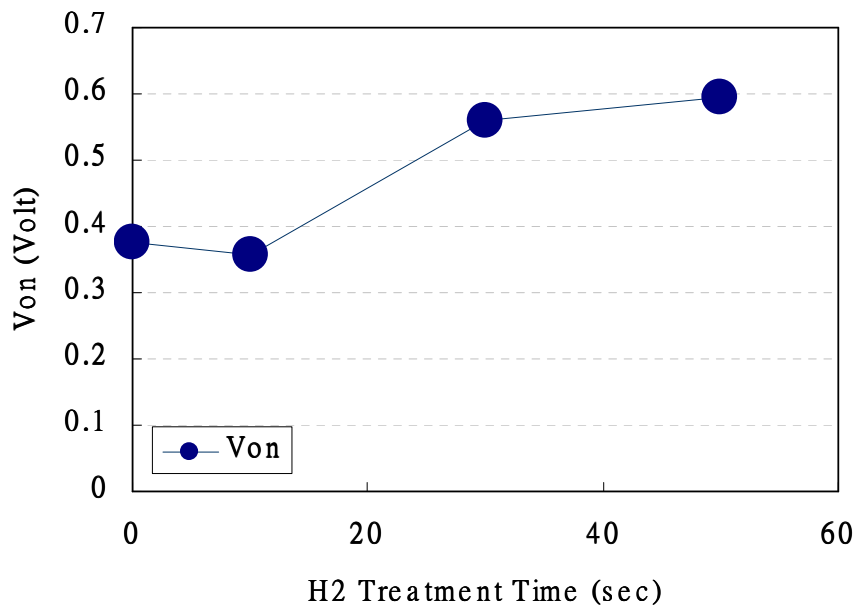**Fig. 71 The V_{on} of HIT solar cell deposited by VHF-PECVD under various post H$_2$ treatment time.**
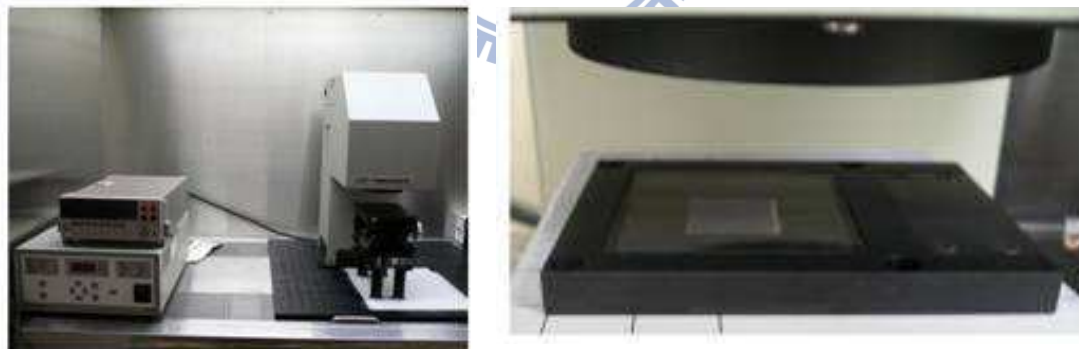
Fig. 72 The solar simulator is for HIT solar cell measurement.

(Center for Nanotechnology, Materials Science, and Microsystems 清大奈微中心)

Ti/Ag   Ti/Ag

ITO

n-doped a-Si

Intrinsic a-Si

p-type c-Si <100>

Ti/Ag

Single Side

Fig. 73 The single-side HIT solar cell structure.

H_2 **treatment improve efficiency 1~2%**

— No H2 Treatment
—■— H2 Treatment

Current Density (mA/cm2)

Voltage (V)

Fig. 74 The photo IV curves of the single-side HIT solar cells. Sample I01 is deposited by VHF-PECVD without post H_2 plasma treatment, and sample I02 is deposited with post H_2 plasma treatment.

Ti/Ag   Ti/Ag

ITO

n-doped a-Si

Intrinsic a-Si

p-type c-Si <100>

p-doped a-Si
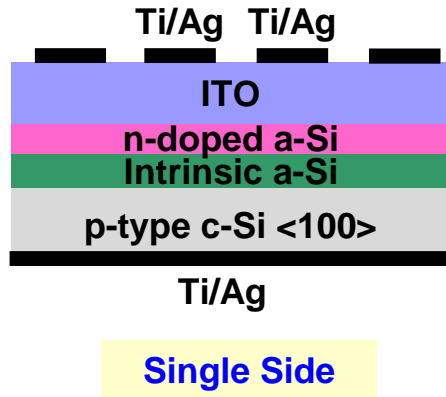
Ti/Ag

Double Side
(Solar Cell Structure)

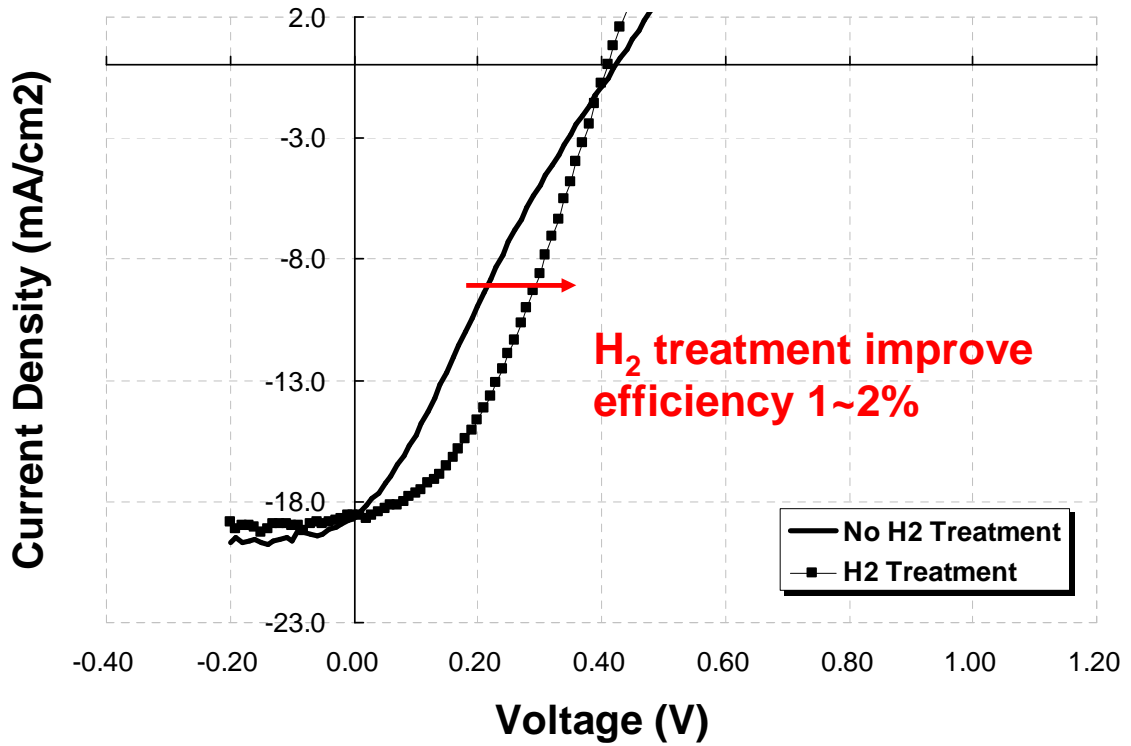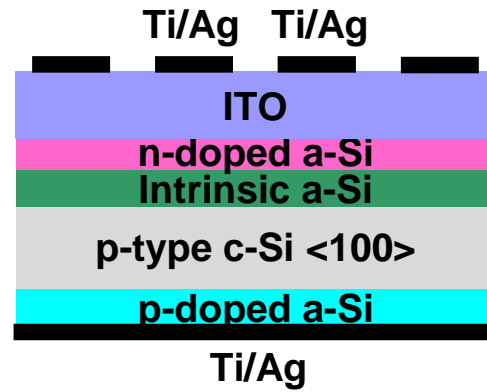Fig. 75 The double-side HIT solar cell structure.
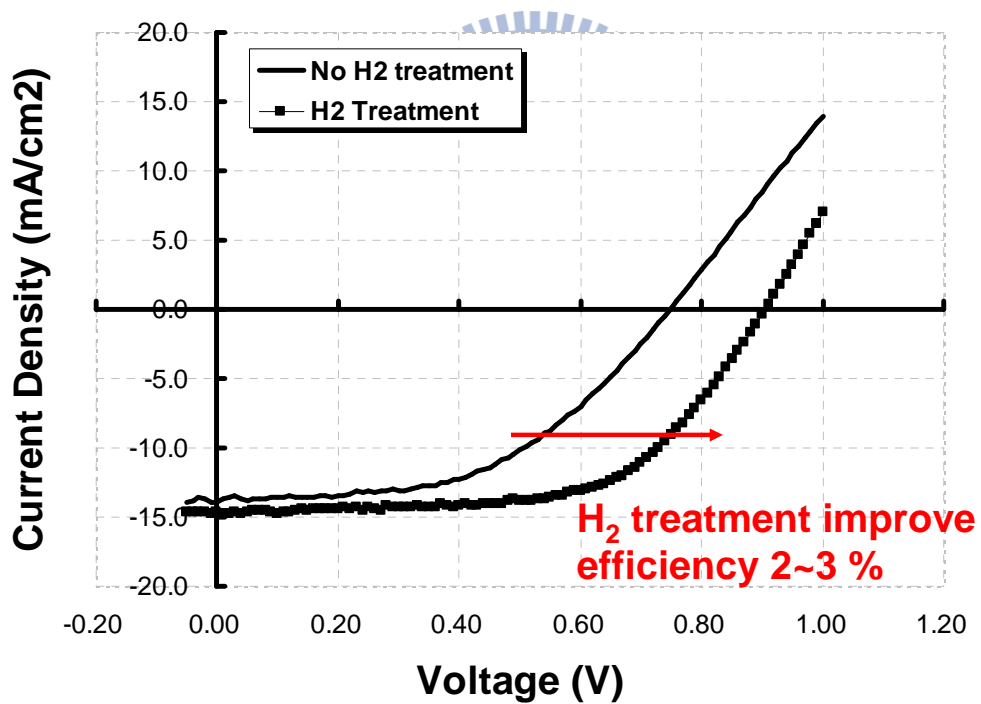
Fig. 76 The photo IV curves of the single-side HIT solar cells. Sample J01 is

deposited by VHF-PECVD without post H_2 plasma treatment, and sample J02 is

deposited with post H_2 plasma treatment.

8.05%
(reducing i-layer)

Ti/Ag   Ti/Ag

ITO

n-doped a-Si

Intrinsic a-Si

p-type c-Si <100>

p-doped a-Si

Ti/Ag

Double Side
(Solar Cell Structure)

Fig. 77 The double-side HIT solar cell structure. In this experiment, we tried to reduce the i-a-Si (i-layer) film thickness. (Marked by the dotted line)
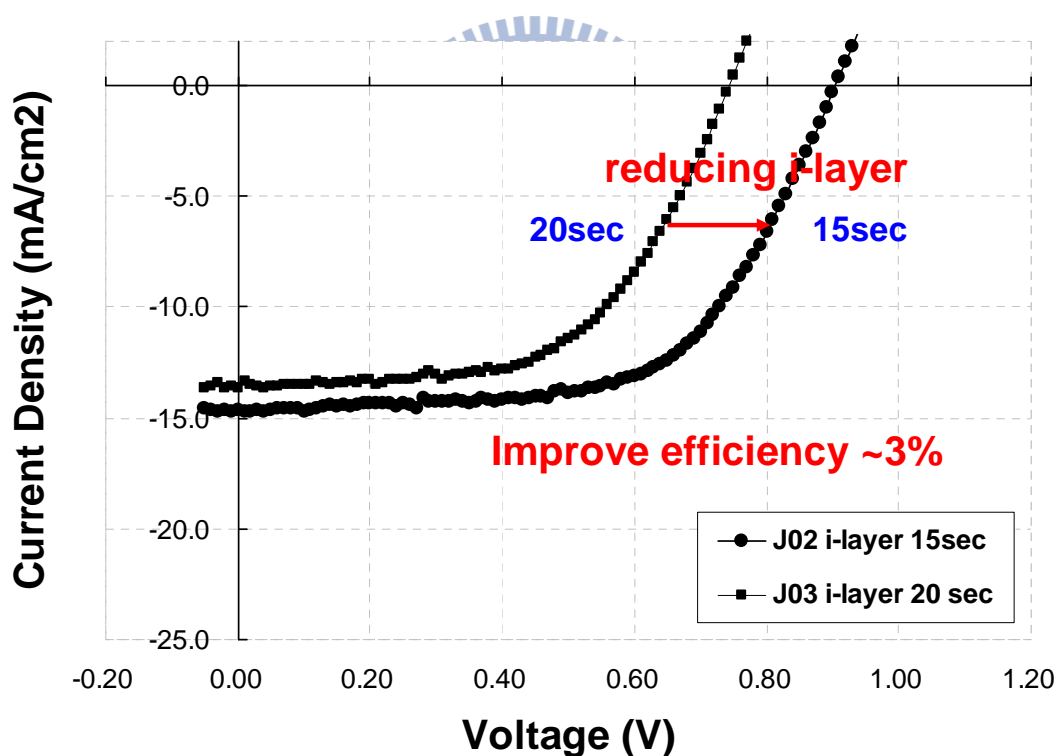
reducing i-layer

20sec → 15sec

Improve efficiency ~3%

J02 i-layer 15sec
J03 i-layer 20 sec
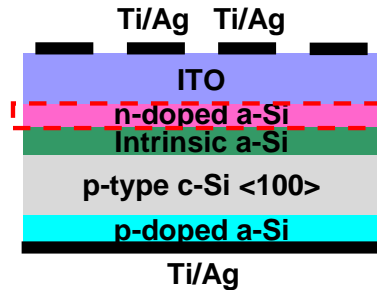
Fig. 78 The photo IV curves of the double-side HIT solar cells. Sample J02 is deposited by VHF-PECVD with 15sec i-a-Si (i-layer) film deposition time, and sample J03 is deposited with 20 sec i-a-Si (i-layer) film deposition time.

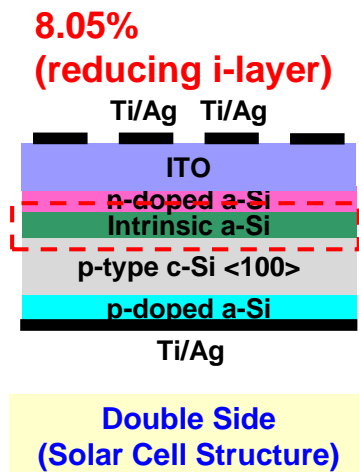**Fig. 79 The double-side HIT solar cell structure. In this experiment, we tried to reduce the n-a-Si (n-layer) film thickness. (Marked by the dotted line)**
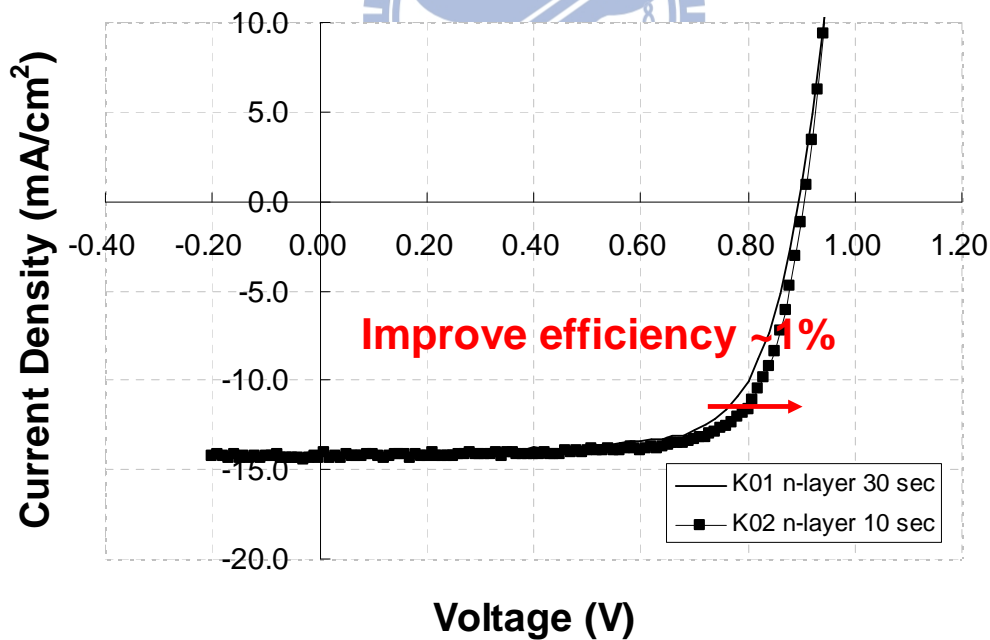
Fig. 80 The photo IV curves of the double-side HIT solar cells. Sample K01 is deposited by VHF-PECVD with 30 sec n-a-Si (n-layer) film deposition time, and sample K02 is deposited with 10 sec i-a-Si (i-layer) film deposition time.
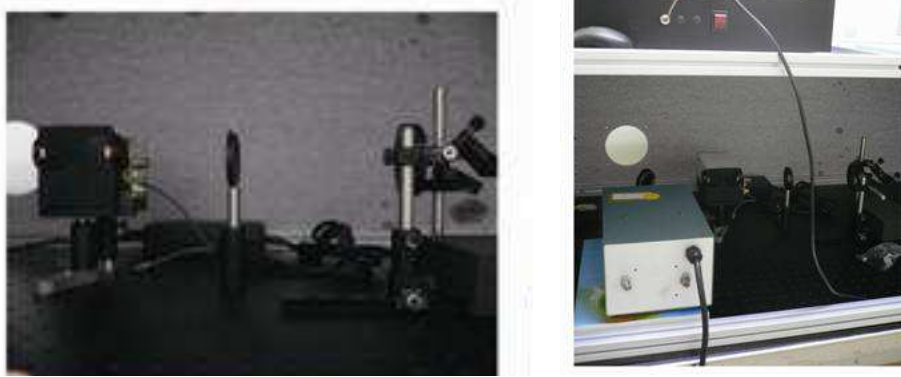
Fig. 81 E.Q.E. measurement on HIT solar cell (Center for Nanotechnology, Materials Science, and Microsystems, 清大奈微中心)

**Double Side
(Solar Cell Structure)**
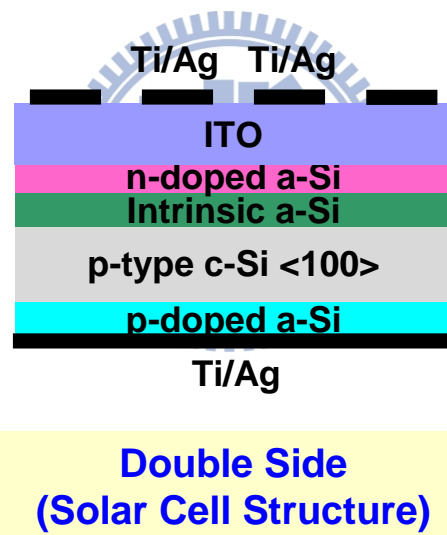
Fig. 82 The double-side HIT solar cell structure.
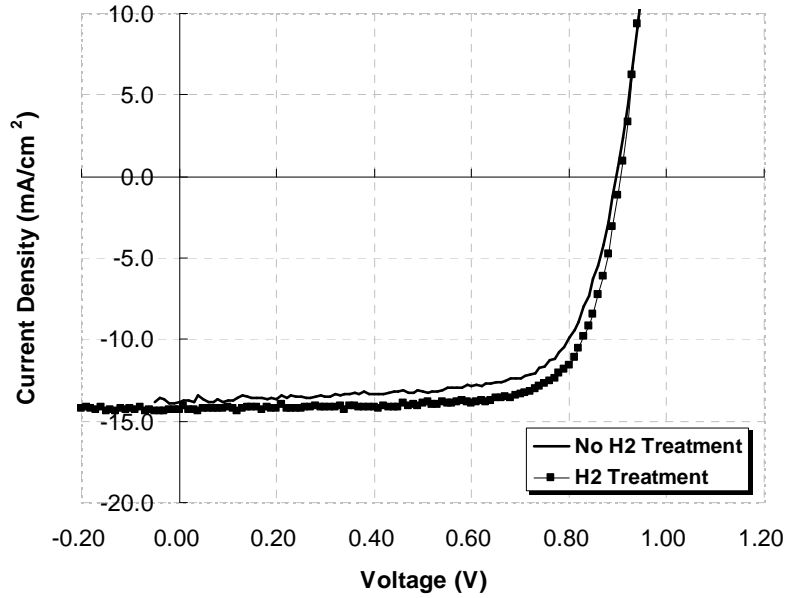
Fig. 83 The photo IV curves of the double-side HIT solar cells. Sample K03 is baseline without post H$_2$ plasma treatment. Sample K02 is deposited by VHF-PECVD with post H$_2$ plasma treatment.
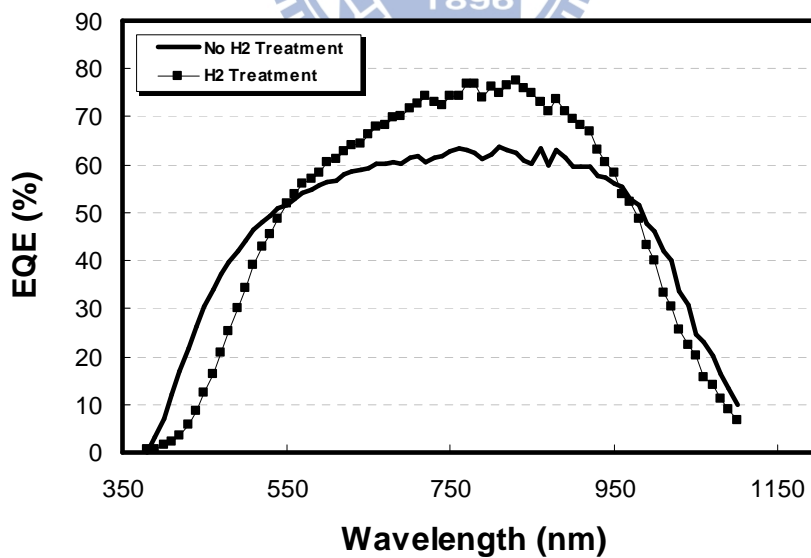
Fig. 84 The E.Q.E. curves of HIT solar cells. Sample K03 is baseline without post H$_2$ plasma treatment. Sample K02 is deposited by VHF-PECVD with post H$_2$ plasma treatment.

p-type c-Si <100>	**Standard RCA clean** **Dilute hydrofluoric acid** **(DHF) clean**

⬇

Intrinsic a-Si **p-type c-Si <100>**	**i-a-Si film deposition by** **VHF-PECVD**

⬇

n-doped a-Si **Intrinsic a-Si** **p-type c-Si <100>**	**n-a-Si film deposition by** **VHF-PECVD**

⬇

H$_2$ Plasma Treatment

⬇ ⬇ ⬇ ⬇ ⬇ ⬇ ⬇ ⬇

n-doped a-Si **Intrinsic a-Si** **p-type c-Si <100>**	**Post-anneal H$_2$ treatment** **on HIT solar cell**

⬇

ITO **n-doped a-Si** **Intrinsic a-Si** **p-type c-Si <100>**	**ITO layer by E-gun** **Evaporation**

Ti/Ag   Ti/Ag

| ITO |
| n-doped a-Si |
| Intrinsic a-Si |
| p-type c-Si <100> |

Ti/Ag

Electrode (Ti/Ag) by E-gun Evaporation

Single Side

RTA Treatment

Ti/Ag   Ti/Ag

| ITO |
| n-doped a-Si |
| Intrinsic a-Si |
| p-type c-Si <100> |

Ti/Ag

RTA treatment on HIT solar cell

Fig. 85 The single-side HIT solar cell deposition under post H$_2$ plasma treatment and RTA treatment.

p-type c-Si <100>	**Standard RCA clean**
	Dilute hydrofluoric acid
	(DHF) clean

↓

| **Intrinsic a-Si** | **i-a-Si film deposition by** |
| p-type c-Si <100> | **VHF-PECVD** |

↓

n-doped a-Si	**n-a-Si film deposition by**
Intrinsic a-Si	**VHF-PECVD**
p-type c-Si <100>	

↓

H$_2$ Plasma Treatment

↓↓↓↓↓↓↓↓

n-doped a-Si	**Post-anneal H$_2$ treatment**
Intrinsic a-Si	**on HIT solar cell**
p-type c-Si <100>	

↓

n-doped a-Si	
Intrinsic a-Si	**p-a-Si film deposition by**
p-type c-Si <100>	**VHF-PECVD**
p-doped a-Si	

↓

ITO

n-doped a-Si

Intrinsic a-Si

p-type c-Si <100>

p-doped a-Si

ITO layer by E-gun Evaporation

Ti/Ag Ti/Ag

ITO

n-doped a-Si

Intrinsic a-Si

p-type c-Si <100>

p-doped a-Si

Ti/Ag

Electrode (Ti/Ag) by E-gun Evaporation

Double Side (Solar Cell Structure)

RTA Treatment

Ti/Ag Ti/Ag

ITO

n-doped a-Si

Intrinsic a-Si

p-type c-Si <100>

p-doped a-Si

Ti/Ag
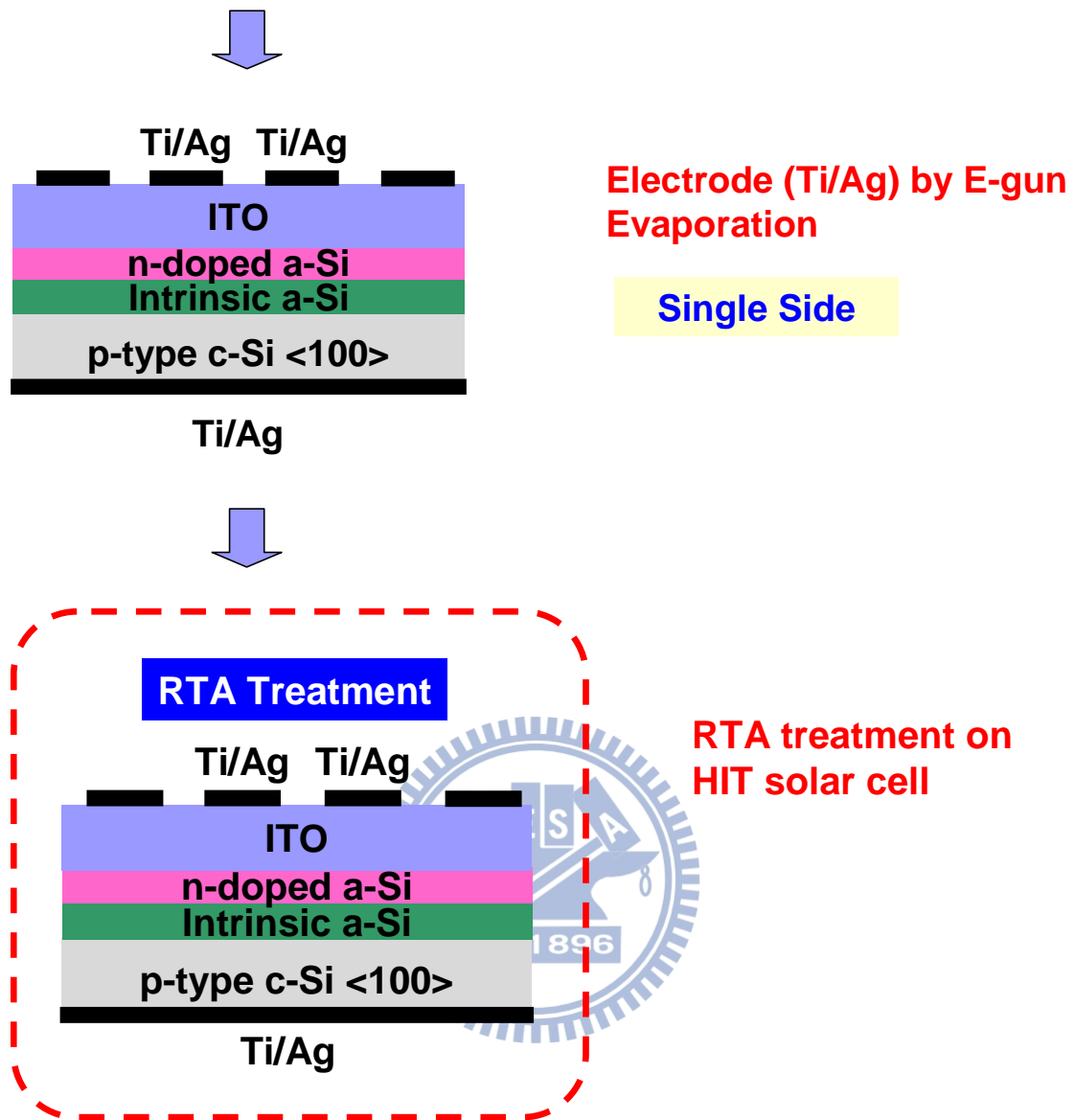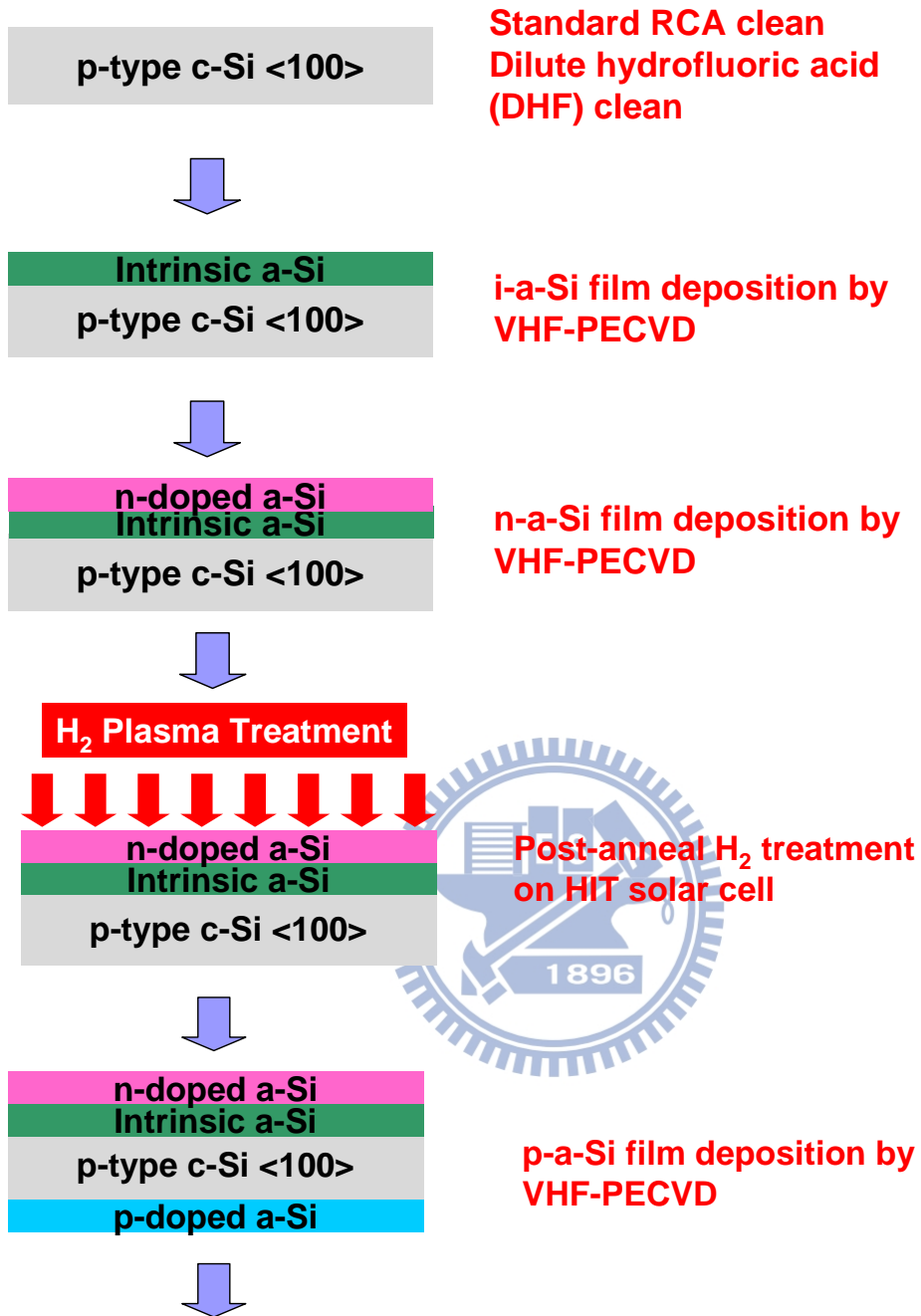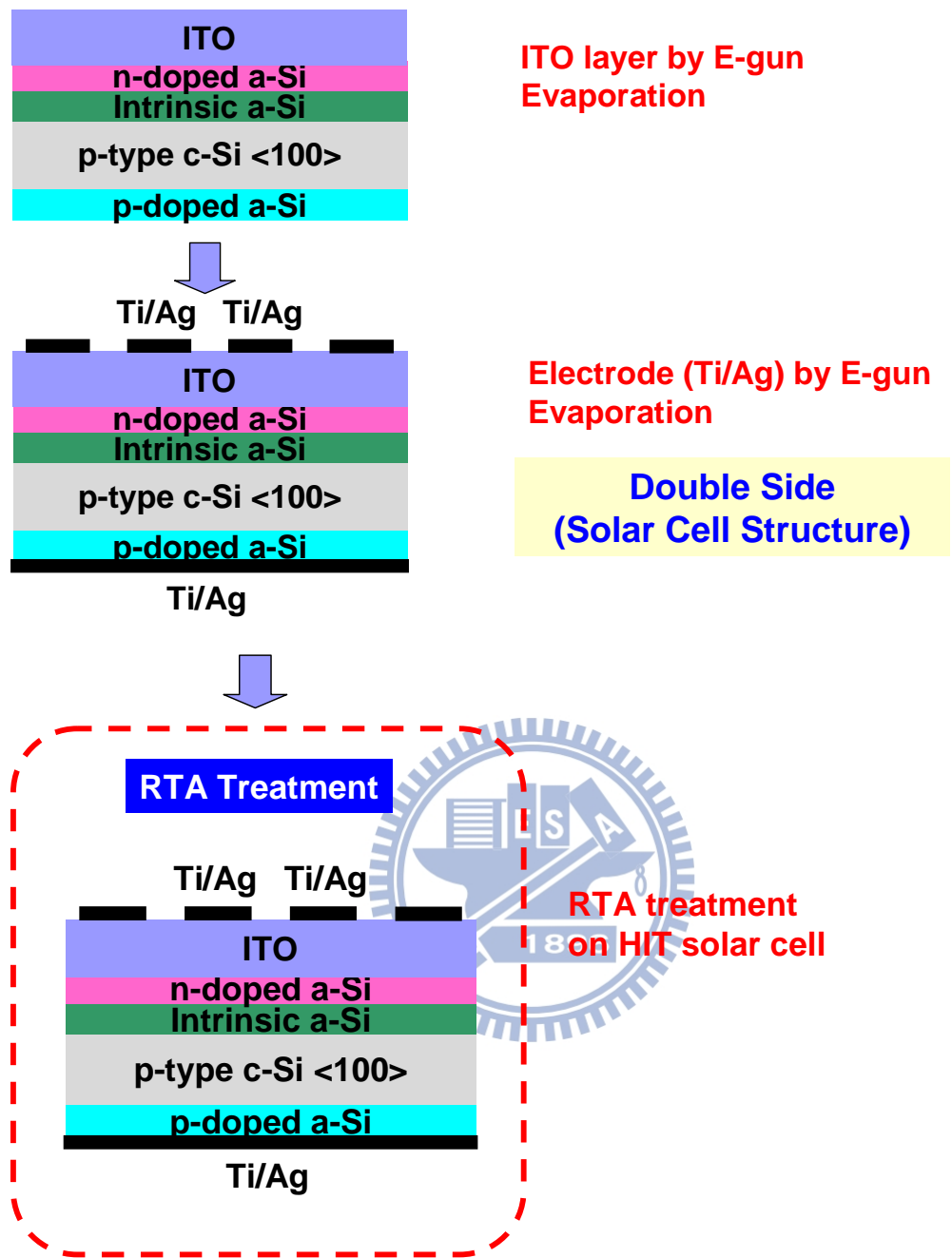
RTA treatment on HIT solar cell

Fig. 86 The double-side HIT solar cell deposition under post H$_2$ plasma

treatment and RTA treatment.

(a)
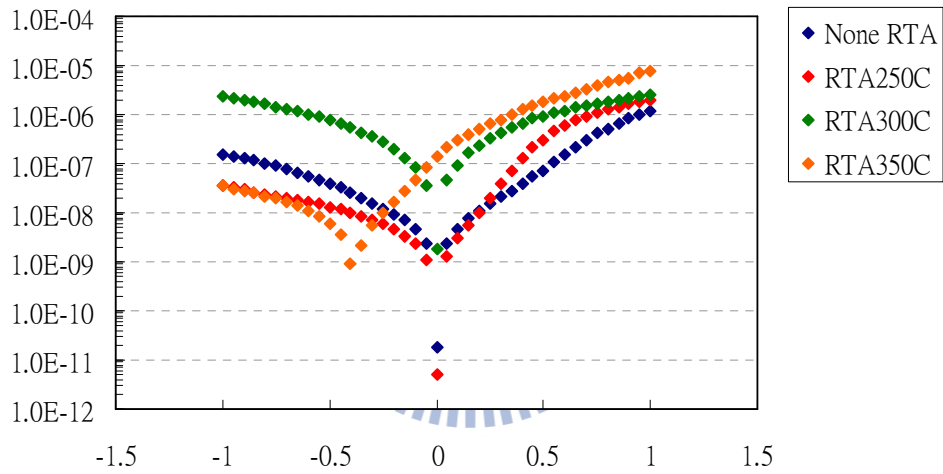
(b)

Fig. 87 The HIT solar cell under various RTA temperature. (a) Dark I-V curves.

(b) Log scales of dark I-V curves from (a).

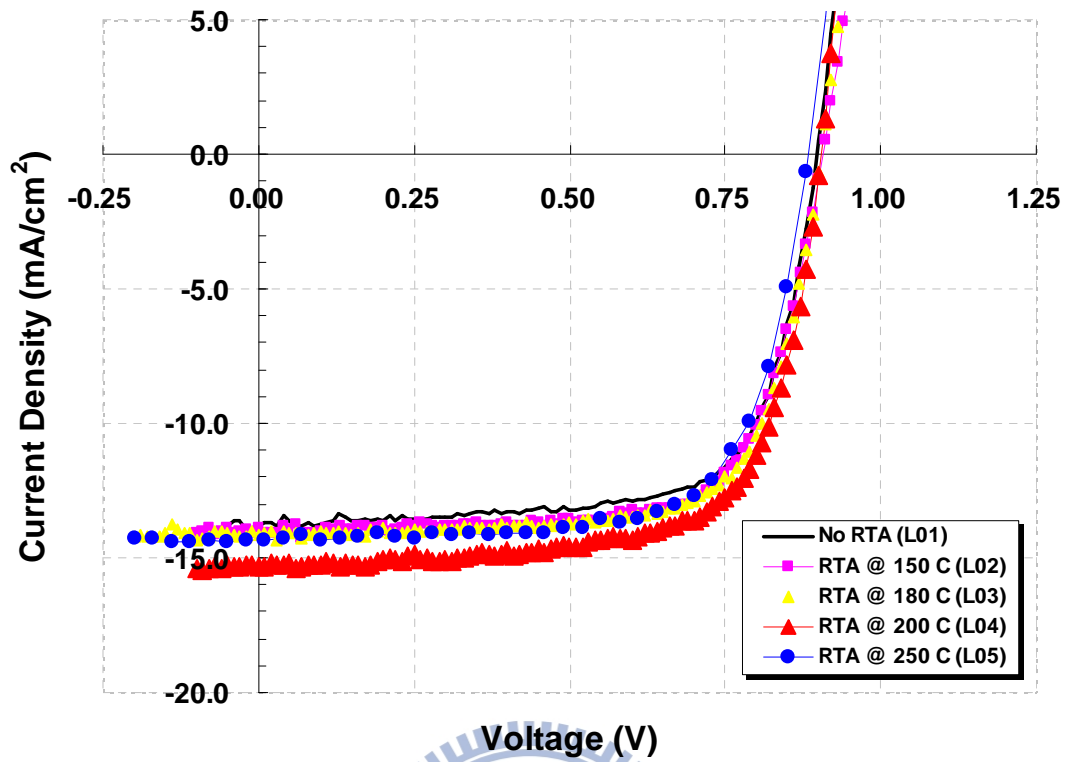**Fig. 88 The photo IV curves of the double-side HIT solar cells. Sample L01 is baseline without RTA treatment. Sample L02, L03, L04, and L05 were treated under various RTA temperatures.**
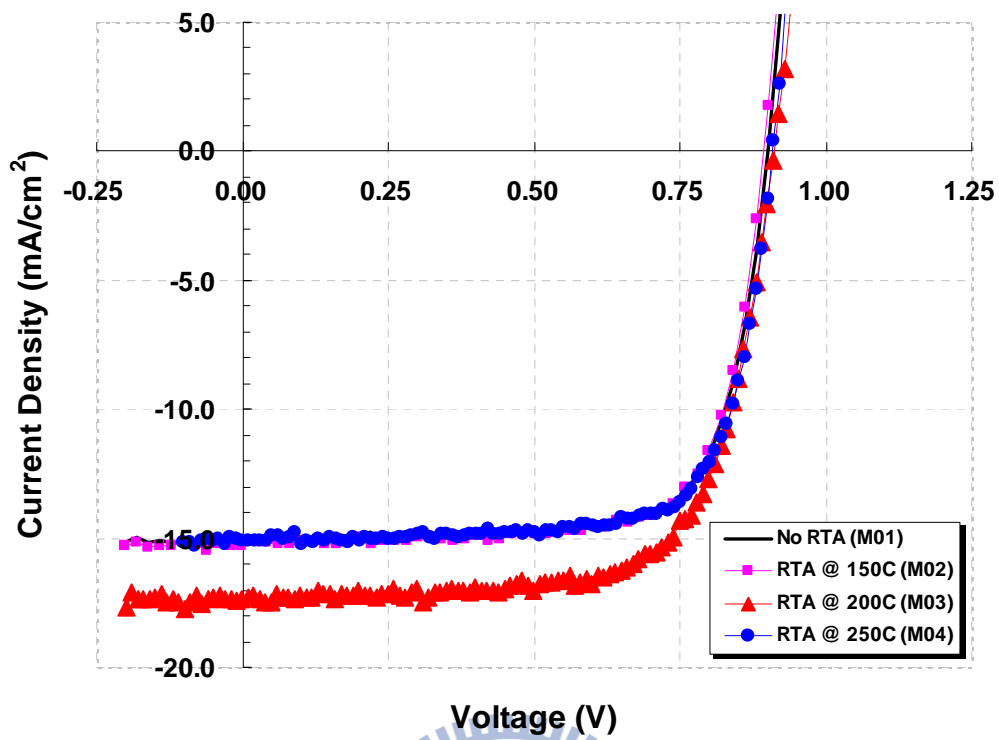
Fig. 89 The photo IV curves of the double-side HIT solar cells with post H$_2$ plasma treatment. Sample M01 is baseline without RTA treatment. Sample M02, M03, and M04 were treated under various RTA temperatures.

Reference

[1] G. Ganguly, T. Ikeda, T. Nishimiya, K. Saitoh, M. Kondo, and A. Matsuda, Appl. Phys. Lett. **69**, 4224 _1996_.

[2] R. Carius, J. Fölsch, D. Lundszien, L. Houben, and F. Finger, Mater. Res.Soc. Symp. Proc. **507**, 813 _1998_.

[3] M. Isomura, K. Nakahata, M. Shima, S. Taira, K. Wakisaka, M. Tanaka,and S. Kiyama, Sol. Energy Mater. Sol. Cells **74**, 519 _2002_.

[4] T. Matsui, M. Kondo, K. Ogata, T. Ozawa, and M. Isomura, Appl. Phys.Lett. **89**, 142115 _2006_.

[5] H. Li *, R.L. Stolk, C.H.M. van der Werf, R.H. Franken, J.K. Rath, R.E.I. Schropp, Journal of Non-Crystalline Solids 352 (2006) 1941–1944

[6] J. Yang, A. Banerjee, S. Guha, Appl. Phys. Lett. 70 (1997) 2975.

[7] P. Agarwal, H. Povolny, S. Han, X. Deng, J. Non-Cryst. Solids 299 (2002) 1213.

[8] J. Yang, B. Yan, G. Yue, S. Guha, in: 31st IEEE PVSEC proceedings, Lake Buena Vista, FL, January 3–7, 2005, p. 1359.

[9] R. Jimenez Zambrano, F.A. Rubinelli, W.M. Arnoldbik, J.K. Rath, R.E.I. Schropp, Sol. Energy Mater. Sol. Cells 81 (2004) 73

[10] A. J. M. van Erven, R. C. M. Bosch and M. D. Bijker, Prog. Photovolt: Res. Appl. 2008; 16:615–627

[11] W. Beyer, J. Hüpkes □, H. Stiebig, Thin Solid Films 516 (2007) 147–154

[12] Wenhui Dua,_, Xianbo Liaoa,1, Xiesen Yanga, Henry Povolnya, Xianbi Xianga,1, Xunming Denga, Kai Sunb, Solar Energy Materials & Solar Cells 90 (2006) 1098–1104

[13] Kartika Chandra Sahoo A Men-Ku Lin A,Edward-Yi Chang A Yi-Yao Lu A Chun-Chi Chen A Jin-Hua Huang A Chun-Wei Chang, Nanoscale Res Lett (2009) 4:680–683

[14] Janez Krc *, Franc Smole, Marko Topic, Journal of Non-Crystalline Solids 352 (2006) 1892–1895

[15] Tsutomu YAMAZAKI, Yoshiaki MATSUMURA, Yukihara URAOKA and Takashi FUYUKI, Jpn. J .of Appl. Phys.,Vol.45,No.8A (2006) pp.6342-6345.

[16] S.Gall, J. Schneider,   J.Klein, et.al, The Solid Film 511-512 (2006) 7-14

[17] Tomoya Fujisaki, Akira Yamada, and Makoto Konagai, Solar Energy Material & Solar Cell 74 (2002) 331-337

[18] Kenji Yamamoto, Akihiko Nakajima, et. al, Solar Energy 77 (2004) 939-949

[19] Kenji Yamamoto, Masashi Yoshimi, et.al, Solar Energy Material & Solar Cells 66 (2001) [1]   Jeffrey Yang, Baojie Yan, Subhendu Guha, Thin Solid Films 487 (2005) 162– 169

[20] C. Y. Chang,"New Green Thin Film Solar Cells",Patent Pending.含太陽電池 感

[21]   Wenhui Du, Xianbo Liao, Xiesen Yang and etc., Solar Energy Materials & Solar Cells 90 (2006) 1098-1104

[22] Jia-Hung Wu,a Jia-Min Shieh,b,z Bau-Tong Dai,b and YewChung Sermon Wua, *Electrochemical and Solid-State Letters, 7 ~6! G128-G130 ~2004!*

117-125

[23]Shui-Yang Lien,and Dong-Sing Wuu, Prog. Photovolt: Res. Appl. (2009)

[24]T.H. Wang, M.R. Page, E. Iwaniczko, Q. Wang, Y. Xu, Y. Yan, L. Roybal, D. Levi, R. Bauer, and H.M. Branz, *National Renewable Energy Laboratory,* Presented at the 2005 DOE Solar Energy Technologies, Program Review Meeting November 7–10, 2005 Denver, Colorado
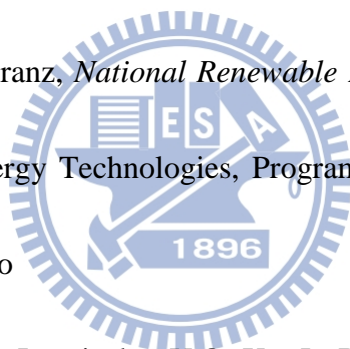
[25]Q. Wang, M.R. Page, E. Iwaniczko, Y.Q. Xu, L. Roybal, R. Bauer, B. To, H.C. Yuan, A. Duda, and Y.F. Yan, *National Renewable Energy Laboratory,* Presented at the 33rd IEEE Photovoltaic Specialists Conference ,San Diego, California ,May 11–16, 2008

[26] Hyun Jin Yang, Kwang-sun Ji, Junghoon Choi, Heon Min Lee * "Annealing effect on surface passivation of a-Si:H/c-Si interface in terms of crystalline volume fraction," Current Applied Physics 10 (2010) S375–S378

[27] S. Kontermann, A. Wolf*,y, D. Reinwand, A. Grohe, D. Biro and R. Preu,"

Optimizing Annealing Steps for Crystalline Silicon Solar Cells with Screen Printed Front Side Metallization and an Oxide-Passivated Rear Surface with Local Contacts," Prog. Photovolt: Res. Appl. 2009; 17:554–566

[28] JaeSung Youa,1, Jinmo Kangb, Donghwan Kimb,*, James Jungho Pakc, Choon Sik Kanga," Copper metallization for crystalline Si solar cells," Solar Energy Materials & Solar Cells 79 (2003) 339–345

[29] Y. Abe!, H. Nagayoshi", T. Kawaba!, N. Arai!, T. Saitoh!,K. Kamisako!,*"Effect of high temperature steam annealing for SiO2 passivation," Solar Energy Materials & Solar Cells 65 (2001) 607~612

[30] Stefaan De Wolf,1,2 Hiroyuki Fujiwara and Michio Kondo "IMPACT OF ANNEALING ON PASSIVATION OF a-Si:H I c-Si HETEROSTRUCTURES,"

[31] A.Froitzheim, K.Brendel, L.Elstner, W.Fuhs, K.Kliefoth, M.Schmidt, Interface recombination inheterojunctionsofamorphousandcrystallinesilicon, J. Non-Cryst.Solids299–302(2002)663–667.

[32]Q.Zhang,M.Zhu,F.Liu,Y.Zhou,Theoptimizationofinterfacialpropertiesof nc-Si:H/c-Si solarcellsinhot-wirechemicalvapordepositionprocess, J. Mater.Sci.Mater.Electron.18(2007)S33–S36.

[33] Y.Tsunomura,Y.Yoshimine,M.Taguchi,T.Baba,T.Kinoshita,H.Kanno H. Sakata,E.Maruyama,M.Tanaka, Twenty-twopercent efficiencyHIT solar cell,

Sol.EnergyMater.Sol.Cells93(2009)670–673.

[34] H.Angermann, W.Henrion,A. Roseler,M.Rebien, Wet-chemicalpassivation of Si(111)-andSi(100)-substrates,Mater.Sci.Eng.B73(2000)178–183.

[35] A.G.Aberle,Surface passivation of crystalline silicon solarcells AReview, Prog. Photovolt.:Res.Appl.8(2000)473–487.

[36] Z.Chen, S.K.Pang, K.Yasutake, A.Rohatgi, Plasma-enhanced chemical-vapor-deposited oxide for low surface recombination velocity and high effective lifetime insilicon,J.Appl.Phys.74(1993)2856–2860.

[37] M.Taguchi, H.Sakata, Y.Yoshimine, E.Maruyama, A.Terakawa, M.Tanaka, An approach for the higher efficiency in the HIT cells, in:Proceedings of the 31st IEEEPhotovoltaicSpecialistsConference,FL,2005,pp.866–871.

[38]I.Martin,M.Vetter,A.Orpella,J.Puigdollers,A.Cuevas,R.Alcubilla,Surface assivation of p-type crystallineSibyplasmaenhancedchemicalvapor deposited amorphousSiCx:H films,Appl.Phys.Lett.79(2001)2199–2201.

[39]   S.Dauwe,J.Schmidt,R.Hezel,Verylowsurfacerecombinationvelocitieson p-andn-typesiliconwaferspassivatedwithhydrogenatedamorphous silicon films,in:Proceedingsofthe29thIEEEPhotovoltaicSpecialists Conference, NewOrleans,2002,pp.1246–1249.

[40]   L.Korte,E.Conrad,H.Angermann,R.Stangl,M.Schmidt,Advancesina-Si:H/ c-Si

heterojunctionsolarcellfabricationandcharacterization,Sol.Energy Mater. Sol.Cells93(2009)905–910.

[41] M.Tanaka,M.Taguchi,T.Matsuyama,T.Sawada,S.Tsuda,S.Nakano H. Hanafusa,Y.Kuwano,Developmentofnewa-Si/c-Siheterojunctionsolar cells: ACJ-HIT(artificiallyconstructedjunction–heterojunctionwithintrinsic thin-layer), Jpn.J.Appl.Phys.31(1992)3518–3522.

[42] T. Lauinger, J. Schmidt, A. G. Aberle, and R. Hezel, Appl. Phys. Lett. **68**, 1232 ~1996!.

[43] M. Cuscunà, A. Bonfiglietti, R. Carluccio, L.Mariucci, F.Mecarini, A. Pecora, M. Stanizzi,A. Valletta, and G. Fortunato, Solid-State Electron,46, 1351 (2002).

[44] M. Kunst, O. Abdallah, and F. Wu¨nsch, Sol. Energy Mater. Sol. Cells **72**, 335 ~2002!.

[45] I. Martı´n, M. Vetter, A. Orpella, J. Puigdollers, A. Cuevas, and R. Alcubilla, Appl. Phys. Lett. **79**, 2199 ~2001

[46] I. Martı´n, M. Vetter, A. Orpella, C. Voz, J. Puigdollers, and R. Alcubilla, *Proceedings of the 17th European Photovoltaic Solar Energy Conference, Munich, October 2001* ~Mani Fotolito, Florence, 2002!, Vol. 3, p. 2954.

[47] I. Martı´n, M. Vetter, A. Orpella, C. Voz, J. Puigdollers, and R. Alcubilla, Appl. Phys. Lett. **81**, 4461 ~2002!.

[48] M. W. M. van Cleef, F. M. Schuurmans, A. S. H. van der Hiede, A. Schonecker, and R. E. I. Schropp, *Proceedings of the Second World Conference on Photovoltaic Solar Energy Conversion, Vienna* ~Stephens, Bedford, 1998!, p. 1661.

[49] P. Roca i Cabarrocas, J. B. Che´vrier, J. Huc, A. Lloret, J. Y. Parey, and J. P. M. Schmitt, J. Vac. Sci. Technol. A **9**, 2331 1991!.

[50] F. M. Schuurmanns, A. Schoenecker, A. R. Burgers, and W. C. Sinke, Appl. Phys. Lett. **71**, 1795 1997

[51] A. G. Aberle, Prog. Photovoltaics **8**, 473   2000.

[52] J. Brody and A. Rohatgi, Solid-State Electron. **45**, 1549 ~2001!.

[53] P. P. Altermatt, J. Schmidt, G. Heiser, and A. G. Aberle, J. Appl. Phys. **82**, 4938 ~1997!.

[54] M. Vetter, I. Martı´n, A. Orpella, C. Voz, J. Puigdollers, and R. Alcubilla, Mater. Res. Soc. Symp. Proc. **715**, 539 ~2002.

[55] E. A. Irene, Thin Solid Films **233**, 96 ~1993!

[56] K.-H. Hwang, E. Yoon, K.-W. Whang, and J. Y. Lee, J. Electrochem. Soc. **144**, 335 ~1997.

[57] H. C. Neitzert, N. Layadi, P. Roca i Cabarrocas, R. Vanderhaghen, and M. Kunst, J. Appl. Phys. **78**, 1438 ~1995.

Publish List

[1] F. C. Tung, M. C. Huang, T. S. Chin, N. C. Lang, P. S. Wu, E. Y. Chang, and J. H. Huang,1" Control of crystalline volume fraction of μc-Si thin film using 40.68 MHz PECVD system for solar cell application, *35th IEEE Photovoltaic Specialists Conference", Nov. 2010, 003748 - 003751*

[2] F.C. Tung, P. S. Wu, T. S. Chin, Tetsuya Suzukic, M. C. Huang, Edward Yi-Chang, and J. H. Huang, 6-10 September 2010, "GROWTH OF MICROCRYSTALLINE SILICON THIN FILM USING 40.68 MHZ PECVD SYSTEM FOR SOLAR CELL APPLICATION", *25th European Photovoltaic Solar Energy Conference and Exhibition / 5th World Conference on Photovoltaic Energy Conversion, 3AV.2.18 (3201 – 3204)*

[3] 董福慶、金崇碩、黃曼琦、張翼、黃金花、羅展興，May 2010, "矽薄膜太陽能電池與 HIT 電池介紹，機械工業雜誌 326 期、99 年 5 月號

[4] B. T. Tran, E. Y. Chang, K. L. Lin, Y. Y. Wong, K. C. Shahoo, H. Y. Lin, M. C. Huang, H. Q. Nguyen and H. D. Trinh., "The Growth of High Quality In0.4Ga0.6N Film on Si Substrate by Metal Organic Chemical Vapor Deposition", Journal of Crystal Growth.(*Revised* manuscript)

[5] Binh-Tinh Tran, Edward-Yi Chang, Kung-Liang Lin, Hai-Dang Trinh, Man-Chi Huang, Viraj Man Shrestta, Tien-Tung Luong and Chi-Lang Nguyen, "Fabrication and Characterization of In0.4Ga0.6N/p-Si Solar Cells", TACT 2011-International Thin Films Conference, Nov 20-23, Kenting, Taiwan.

[6] Man-Chi Huang[1], Chia-Hua Chang[1], Fang-Ming Li[1], Ching-Hsiang Hsu[1], Binh-Tinh Tran[1], S.S. Tang[1], Kung-Liang Lin[1], Yueh-Chin Lin[1], Fu-Ching Tung[2], Muh-Wang Liang[2], and Edward Yi-Chang[1]
[1]Department of Materials Science and Engineering, National Chiao Tung University, Hsinchu, Taiwan
[2]Mechanical and Systems Research Laboratories K500, MSL/ITRI, Hsinchu, Taiwan
THE EFFECT OF H_2 TREATMENT ON HETEROJUNCTION WITH INTRINSIC THIN LAYER (HIT) SOLAR CELL PERFROMANCE USING 40.68MHz VHF-PECVD System 37th IEEE PVSC, Seattle

[7] *M. C. Huang[1], Y. Y. Wong1,C. H. Chang[1], F. M. Li1, C. H. Hsu[1], B. T. Tran[1], S. S. Tang[1], K. L. Lin[1],*

Y. C. Lin[1], F. C. Tung[2], M. W. Liang[2], and Edward Y. Chang[1],*
[1]Department of Materials Science and Engineering, National Chiao Tung University, Hsinchu, Taiwan
[2]Mechanical and Systems Research Laboratories K500, MSL/ITRI, Hsinchu, Taiwan
IMPROVEMENT OF HETEROJUNCTION WITH INTRINSIC THIN LAYER (HIT) SOLAR CELL PERFORMANCE BY USING VHF-PECVD SYSTEM
PHOTOVOLTAIC TECHNICAL CONFERENCE - THIN FILM & ADVANCED SOLUTIONS 2011 (accepted)

[8] TACT 台灣鍍膜研討會,oral presentation
M. C. Huang[1], Y. Y. Wong[1], F. M. Li[1], H. D. Trinh[1], B. *T.* Tran[1], K. L. Lin[1], Y. T. Ho[1], Y. C. Lin[1],
F. C. Tung[2], M. W. Liang[2], and Edward Y. Chang[1],[*]
(黃曼琦,黃延儀,李芳茗,金海光,陳平淨,林龔樑,林岳欽,何焱騰,董福慶,梁沐旺,張翼)
[1]Department of Materials Science and Engineering, National Chiao Tung University, Hsinchu, Taiwan (台灣,新竹市,國立交通大學,材料科學與工程系所)
[2]Mechanical and Systems Research Laboratories K500, MSL/ITRI, Hsinchu, Taiwan
(台灣,新竹市,工業技術研究院,機械與系統研究所)
IMPROVEMENT OF HETEROJUNCTION WITH INTRINSIC THIN LAYER (HIT) SOLAR CELL PERFORMANCE BY USING VHF-PECVD SYSTEM

[9] Binh-Tinh Tran, Edward Yi Chang, Hai-Dang Trinh, Ching-Ting Lee, Kartika Chandra Sahoo, Kung-Liang Lin, Man-Chi Huang, Hung-Wei Yu, Tien-Tung Luong, Chen-Chen Chung, Chi-Lang Nguyen
Solar energy material and solar cells
Fabrication and characterization of n-$In_{0.4}Ga_{0.6}N$/p-Si solar cell